



HAL
open science

Designing a high data rate wireless communication system in a doubly selective channel: TransPod system

Bentolhoda Kazemzadeh Osgoei

► **To cite this version:**

Bentolhoda Kazemzadeh Osgoei. Designing a high data rate wireless communication system in a doubly selective channel: TransPod system. Networking and Internet Architecture [cs.NI]. Université de Limoges, 2024. English. NNT: 2024LIMO0055 . tel-04860626

HAL Id: tel-04860626

<https://theses.hal.science/tel-04860626v1>

Submitted on 1 Jan 2025

HAL is a multi-disciplinary open access archive for the deposit and dissemination of scientific research documents, whether they are published or not. The documents may come from teaching and research institutions in France or abroad, or from public or private research centers.

L'archive ouverte pluridisciplinaire **HAL**, est destinée au dépôt et à la diffusion de documents scientifiques de niveau recherche, publiés ou non, émanant des établissements d'enseignement et de recherche français ou étrangers, des laboratoires publics ou privés.

Université de Limoges

ED 653 : Sciences et Ingénierie – XLIM

Faculté des Sciences et Techniques – Institut de Recherche XLIM

Thèse pour obtenir le grade de

Docteur de l'Université de Limoges

Réseaux ubiquitaires adaptatif hauts débits, Systèmes & Réseaux Intelligents

Présentée et soutenue par

Bentolhoda KAZEMZADEH OSGOEI

Le 27 Septembre 2024

**CONCEPTION D'UN SYSTÈME DE TRANSMISSION HAUT DÉBIT DANS UN CANAL DOUBLE-
MENT SÉLECTIF: SYSTÈME DE TRANSPOD**

Thèse dirigée par Vahid Meghdadi et Abbas Bradai

JURY :

Rapporteurs

M. Guillaume Ferre, Professeur – Universités ENSEIRB-MATMECA

M. Hmaied Shaiek, Professeur – Conservatoire National des Arts et Métiers

Examineurs

M. Abbas Bradai, Professeur – Université de Côte d'Azur

M. Jean-Pierre Cances, Professeur – Université de Limoges

M. Iyad Dayoub, Professeur – Université Polytechnique Hauts de France

M. Vahid Meghdadi, Professeur – Université de Limoges

M. Hamid Meghdadi, PhD – R&D TransPod France



To My Loving Family,

This thesis is dedicated to my family—my father, mother, and sister—with deep love. Your constant encouragement, love, and belief in me, even from afar, have been invaluable. To my husband, Omid, your unwavering support has made it possible for me to pursue my dreams, and I could not have done this without you. To my sons, Amirhossein and Danial, your energy and love have kept me inspired throughout this path.

“It always seems impossible until it’s done.”

Nelson Mandela

Acknowledgements

First and foremost, I would like to express my deepest gratitude to my supervisor, **Vahid Meghdadi**, for his invaluable guidance, encouragement, and unwavering support throughout this journey. His insights and expertise have been crucial in shaping this thesis, and I am profoundly thankful for his direction.

I am also incredibly grateful to **TransPod**, whose financial support made this research possible. Special thanks to **Sebastien Gendron**, **Ryan Janzen** and **Fabien Larocca** for their trust and encouragement, and to all my colleagues for creating such a collaborative and motivating work environment. A special mention goes to **Hamid Meghdadi** for his technical support and advice, especially during the more challenging moments of this project. Your help was truly appreciated.

I would also like to extend my gratitude to **Prof. Gerald Matz** for providing me with the wonderful opportunity to visit his group at TU WIEN (Vienna University of Technology), Vienna, Austria. This experience greatly enriched my research and broadened my academic perspective.

On a more personal note, I owe a deep debt of gratitude to my husband, **Omid**. His unwavering belief in me, constant encouragement, and unconditional support have been the foundation upon which I could complete this work. Without him, this achievement would not have been possible.

I also want to thank my sons, **Amirhossein** and **Danial**, whose boundless energy and joy provided me with the motivation and inspiration to persevere. You both are the light of my life, and your smiles kept me going, even in the most difficult times.

I am truly grateful to my friends in Toulouse and Limoges for making this journey unforgettable. Their support, advice, and company meant the world to me, and I'm so thankful for their friendship.

Finally, I want to express my heartfelt thanks to my family. Although we are separated by distance, your love and encouragement have always been felt. Your unwavering support has been a source of strength throughout this journey, and I am forever grateful for that.

Droits d'auteurs

Cette création est mise à disposition selon le Contrat :

« Attribution-Pas d'Utilisation Commerciale-Pas de modification 3.0 France »

disponible en ligne : <http://creativecommons.org/licenses/by-nc-nd/3.0/fr/>















List of Contents

| | | |
|----------|---|-----------|
| 1 | Introduction | 18 |
| 1.1 | Motivation | 19 |
| 1.2 | Challenges | 20 |
| 1.2.1 | Tube Structure | 21 |
| 1.2.2 | Ultra High Speed | 21 |
| 1.2.3 | Special Noise due to the Plasma | 21 |
| 1.2.4 | Handover | 21 |
| 1.3 | Related Works | 22 |
| 1.4 | Contributions | 23 |
| 1.5 | Thesis Outline | 24 |
| 1.6 | List of Publications | 26 |
| 2 | Wireless Channel Background | 27 |
| 2.1 | Introduction | 29 |
| 2.2 | Large-Scale Fading | 30 |
| 2.3 | Small-Scale Fading | 30 |
| 2.3.1 | Multipath (Time Dispersion / Frequency-Selective) | 31 |
| 2.3.2 | Time-Variance (Frequency Dispersion / Time-Selective) | 31 |
| 2.3.3 | Doubly Selective Channels | 32 |
| 2.4 | Representations of Wireless Channels | 32 |
| 2.4.1 | Time-Delay Representation of LTV Channels | 33 |
| 2.4.2 | Time-Frequency Representation of LTV Channels | 34 |
| 2.4.3 | Delay-Doppler Representation of LTV Channels | 37 |
| 2.4.4 | Virtual relation between time-frequency and delay-Doppler representations | 39 |
| 2.5 | OFDM Review | 42 |
| 2.5.1 | OFDM disadvantages | 44 |
| 2.6 | OTFS Modulation | 46 |
| 2.6.1 | System Model | 46 |

| | | |
|----------|--|-----------|
| 2.6.2 | OTFS Transmitter | 48 |
| 2.6.3 | Wireless Channel | 50 |
| 2.6.4 | OTFS Receiver | 51 |
| 2.6.5 | OTFS input-output relation | 52 |
| 2.6.6 | OTFS Variants | 53 |
| 2.7 | Summary | 57 |
| 3 | Channel Characteristics of Tube Transportation Ultra High Speed Systems | 58 |
| 3.1 | Introduction | 60 |
| 3.2 | Ray Tracing in a Tube Transportation System | 62 |
| 3.3 | TransPod System | 64 |
| 3.4 | System Model | 65 |
| 3.4.1 | Path Loss | 66 |
| 3.4.2 | Delay spread | 77 |
| 3.4.3 | Doppler spread | 78 |
| 3.4.4 | Power-delay-Doppler profile | 80 |
| 3.4.5 | Time-Frequency Transfer Function | 81 |
| 3.5 | Plasma-based Power Transmission System | 82 |
| 3.6 | Impulsive Noise | 83 |
| 3.6.1 | Two-state Markov-Gaussian Model | 84 |
| 3.6.2 | Noise Measurements | 86 |
| 3.6.3 | Data Analysis | 86 |
| 3.6.4 | Markov Chain Model | 90 |
| 3.6.5 | Numerical Results | 91 |
| 3.7 | Coding Techniques to Mitigate the Impulsive Noise | 93 |
| 3.8 | Proposed Architecture for Handover | 95 |
| 3.9 | Summary | 96 |
| 4 | OTFS Channel Estimation | 97 |
| 4.1 | Introduction | 98 |
| 4.2 | Motivation | 100 |
| 4.3 | Threshold-based Channel Estimation Algorithm | 101 |
| 4.4 | Problem Formulation | 108 |
| 4.5 | Sequence-based Pilot Channel Estimation | 115 |
| 4.5.1 | An Optimum Sequence | 119 |
| 4.5.2 | Pilot Sequence Placement | 120 |
| 4.5.3 | Channel Parameters Estimation | 122 |

| | | |
|----------|---|------------|
| 4.5.4 | PAPR of the Sequence Pilot | 125 |
| 4.6 | Detection | 127 |
| 4.7 | Simulation Results | 128 |
| 4.7.1 | NMSE | 129 |
| 4.7.2 | BER | 132 |
| 4.8 | Summary | 133 |
| 5 | Deep Learning Based Channel Estimation in ZP-OTFS Modulation Systems | 134 |
| 5.1 | Related works | 136 |
| 5.2 | Motivation | 137 |
| 5.2.1 | Background on neural network | 138 |
| 5.2.2 | Dataset Management: Train, Validation, and Test Sets | 141 |
| 5.2.3 | System Model and Data arrangement | 141 |
| 5.2.4 | Proposed DNN structure | 143 |
| 5.3 | Discussions and Simulation analysis | 145 |
| 5.3.1 | Impact of pilot power | 146 |
| 5.3.2 | DNN Architecture | 150 |
| 5.3.3 | Impact of Tx-Rx distances | 152 |
| 5.3.4 | Impact of SNR on the trained DNN model | 154 |
| 5.3.5 | Computational Complexity | 155 |
| 5.4 | Summary | 155 |
| 6 | Conclusion and Future Works | 157 |
| 6.1 | Conclusion | 158 |
| 6.2 | Future Works | 158 |
| 7 | Bibliography | 161 |
| | References | 162 |
| | List of Publications | 178 |

List of Figures

| | | |
|------|--|----|
| 2.1 | Different domain representations of LTV channel | 33 |
| 2.2 | Time-delay representation of a doubly selective channel. | 34 |
| 2.3 | Time-frequency channel representation of a doubly selective channel vs. a frequency selective channel (time-invariant) | 36 |
| 2.4 | Time-frequency channel representation of a Doubly selective channel vs. a static multipath channel (linear time-invariant) | 39 |
| 2.5 | Discrete time-frequency grid and delay-Doppler grid. | 40 |
| 2.6 | Channel representation in delay-Doppler domain with existing paths. . . | 41 |
| 2.7 | OTFS modulation implementation, direct approach | 47 |
| 2.8 | OTFS modulation implementation, two-step approach | 48 |
| 2.9 | RZP-OTFS structure of OTFS time domain signal;  ,  : data and  : L_{ZP} | 54 |
| 2.10 | RCP-OTFS structure of OTFS time domain signal;  ,  : data and  : L_{CP} | 54 |
| 2.11 | ZP-OTFS structure of OTFS time domain signal;  ,  : data and  : L_{ZP} | 55 |
| 2.12 | CP-OTFS structure of OTFS time domain signal;  ,  : data and  : L_{CP} | 56 |
| 3.1 | | 62 |
| 3.2 | FluxJet vehicle inside a tube in TransPod line. | 64 |
| 3.3 | FluxJet main technologies | 65 |
| 3.4 | Simplified model of the multipath channel inside the tube. | 66 |
| 3.5 | Simplified model of the multipath channel inside the tube. | 67 |
| 3.6 | Path loss in the TransPod tube. | 68 |
| 3.7 | Path loss in the TransPod tube at the carrier frequencies 870 MHz Megahertz (MHz), 2.45 Gigahertz (GHz), and 4 GHz. | 69 |
| 3.8 | Path loss for different construction materials at 2.45 GHz. | 72 |
| 3.9 | Half-wave dipole antenna and 3D pattern | 73 |
| 3.10 | Half-wave dipole antenna patterns | 73 |
| 3.11 | Path loss for isotropic and directive antenna. | 76 |
| 3.12 | Delay spread for different Tx-Rx distances. | 78 |
| 3.13 | Doppler spectrum for different Tx-Rx distances. | 79 |

| | |
|--|-----|
| 3.14 Doppler spectrum for different Tx-Rx distances. | 80 |
| 3.15 Power-Delay-Doppler profiles for different transmitter-receiver distances: (a) 10m, (b) 80m, (c) 700m | 81 |
| 3.16 Time-frequency transfer function $H(t, f)$ | 82 |
| 3.17 FluxJet power transmission schematic. | 83 |
| 3.18 Schematic of the TransPod system with the plasma-based power trans- mission system and transmitter/receiver inside the steel tube. | 84 |
| 3.19 Markov chain representation with two states G and B and transition probabilities. | 85 |
| 3.20 Plasma arc current during a system transient at various electrode separa- tions. | 86 |
| 3.21 Plasma arc current during a system transient, at an electrode separation of 1mm, overlaid with the model's generated square wave pulses. | 88 |
| 3.22 Plasma arc current during a system transient, at an electrode separation of 3mm, overlaid with the model's generated square wave pulses. | 89 |
| 3.23 Plasma arc current during a system transient, at an electrode separation of 6mm, overlaid with the model's generated square wave pulses. | 89 |
| 3.24 Noise samples modeled by Two-state Markov model. | 93 |
| 3.25 Dual-frequency system architecture. | 95 |
| | |
| 4.1 Symbols pattern at the transmitter and receiver for the classical impulse pilot scheme in [135]. | 102 |
| 4.2 Transmitted symbols in delay-Doppler domain. | 103 |
| 4.3 Received symbols in delay-Doppler domain. | 103 |
| 4.4 Pilot output grid in the presence of noise. | 105 |
| 4.5 Symbols pattern at the transmitter and receiver for the classical impulse pilot scheme for fractional Doppler indices in [136]. | 106 |
| 4.6 Estimation grid for $P_{\text{pilot}} = 5$ and $P_{\text{pilot}} = 25$ | 108 |
| 4.7 Amplitude of estimated channel coefficients for $P_{\text{pilot}} = 5$ and $P_{\text{pilot}} = 25$ | 109 |
| 4.8 High-power impulse pilot causing elevated PAPR in the time-domain signal. | 110 |
| 4.9 Comparison of Complementary Cumulative Distribution Function (CCDF) of the Peak to Average Power Ratio (PAPR) for full data transmission, and impulse pilot with low and high pilot power P_{pilot} | 113 |
| 4.10 Pilot output grid with fractional Doppler indices $\kappa_i = [0, 1.2, 2.5, 3.7]$ and delay indices $l_i = [0, 1, 2, 3]$ in the absence of noise. | 115 |
| 4.11 Sequence pilot balancing power distribution in the time domain signal. | 116 |

| | |
|--|-----|
| 4.12 Pilot sequence, guard, and data symbol placements in the Delay-Doppler domain at the transmitter, with $N = 12$, $M = 16$, $m_p = 14$, and $\ell_{\max} = 2$, ■ data, ■ pilot, and ■ guard. | 117 |
| 4.13 Channel effect on sequence pilot in delay-Doppler domain with $l = \{0, 1, 2\}$ and $k = \{3, 2, 1\}$. ■ data, ■ pilot at l_0 , ■ pilot at l_1 , ■ pilot at l_2 , and ■ channel effect of the data symbols spread on the guard area above the pilot. | 118 |
| 4.14 Auto-correlation function of the Constant Amplitude Zero Autoc-orrelation (CAZAC) and Pseudo-Random Noise (PN) sequences | 120 |
| 4.15 delay-Doppler grid structure with pilot sequence for CP-OTFS and ZP-OTFS; ■: data, ■: guard, and ■: pilot sequence. | 121 |
| 4.16 delay-Doppler grid structure with pilot sequence for RCP/RZP-OTFS; ■: data, ■: guard, and ■: pilot sequence. | 121 |
| 4.17 CAZAC sequence in the Delay-Doppler domain at the transmitter located at delay bin $m_p = 14$, and $\ell_{\max} = 2$, ■ data, ■ pilot, and ■ guard. | 123 |
| 4.18 PAPR vs PDR for impulse pilot and sequence pilot. | 126 |
| 4.19 High-power impulse pilot causing elevated PAPR in the time-domain signal. | 127 |
| 4.20 NMSE performance between proposed sequence pilot structure and conventional method with impulse pilot for different PDRs. | 130 |
| 4.21 NMSE performance comparison of proposed sequence pilot structure and conventional impulse pilot as a function of pilot power, for different SNR_d | 131 |
| 4.22 NMSE performance comparison of proposed sequence pilot structure and conventional impulse pilot as a function of pilot power, for different SNR_d | 132 |
| 4.23 BER performance of the proposed sequence pilot and conventional impulse pilot channel estimation under different PDR. | 133 |
| 5.1 Neuron architecture with n input values. | 139 |
| 5.2 delay-Doppler grid structure with pilot sequence for CP-OTFS and ZP-OTFS; ■: data, ■: guard, and ■: pilot sequence. | 142 |
| 5.3 A fully connected neural network (FNN); ■: Inputs, ■: Neurons, and ■: Outputs | 144 |
| 5.4 NMSE performance comparison between the proposed DNN approach and conventional scheme with an impulse pilot. | 148 |

| | | |
|------|--|-----|
| 5.5 | NMSE performance comparison between the proposed DNN approach and conventional scheme with a sequence pilot. | 148 |
| 5.6 | BER performance comparison between the proposed DNN approach and conventional scheme with an impulse pilot. | 149 |
| 5.7 | BER performance comparison between the proposed DNN approach and conventional scheme with a sequence pilot. | 149 |
| 5.8 | NMSE performance of the trained DNN model using different architectures. | 151 |
| 5.9 | BER performance comparison between the different DNN architectures. | 151 |
| 5.10 | NMSE performance of the trained DNN model using several distances in data SNR = 15dB. | 153 |
| 5.11 | NMSE performance of the trained DNN model using several distances in data SNR = 30dB. | 153 |
| 5.12 | NMSE performance of the trained DNN model using different architectures. | 154 |
| 5.13 | BER performance comparison between the different DNN architecture. . | 155 |

List of Tables

- 1 Mathematical Notation and Operators 17
- 2.1 Comparison of OTFS variants in terms of spectral efficiency and transmit power. 57
- 3.1 Comparison between the statistical parameters from the measured data and the model (E.D stands for the distance between electrodes). 92
- 4.1 Spectral efficiencies of OTFS variants with/without sequence pilot insertion for channel estimation. 122
- 4.2 System Parameters for Simulation 129
- 5.1 Parameters of DNN architecture. 145

List of **A**bbreviations

- 1G** – First Generation Mobile Radio.
- 3GPP** – 3rd Generation Partnership Project.
- 4G** – Fourth Generation Mobile Radio.
- 5G** – Fifth Generation Mobile Radio.
- 5G-NR** – fifth generation new radio.
- 6G** – Sixth Generation Mobile Radio.

- ANN** – Artificial Neural Network.
- AWGN** – Additive white Gaussian noise.

- BER** – Bit Error Rate.

- CAZAC** – Constant Amplitude Zero Autoc-orrelation.
- CCDF** – Complementary Cumulative Distribution Function.
- CNN** – Convolutional Neural Network.
- CP** – Cyclic Prefix.
- CSI** – Channel State Information.

- DFT** – Discrete Fourier Transform.
- DL** – Deep Learning.
- DNN** – Deep Neural Network.

- ECC** – Error Correction Code.

- FFT** – Fast Fourier Transform.
- FSPL** – Free-Space Path Loss.

- GHz** – Gigahertz.
- GSM-R** – Global System for Mobile communications-Railways.

- HSR** – High Speed Railway.
- ICI** – Inter Carrier Interference.
- IDFT** – Inverse Discrete Fourier Transform.
- IDZT** – Inverse Zak Transform.
- IFFT** – Inverse Fast Fourier Transform.
- ISFFT** – Inverse Symplectic Fast Fourier transform.
- ISI** – Inter Symbol Interference.
- LDPC** – Low Density Parity Check.
- LMMSE** – Linear Minimum Mean Square Error.
- LOS** – Line-of-Sight.
- LS** – Least Squares.
- LSTM** – Long Short-Term Memory.
- LT** – Luby Transform.
- LTE-R** – Long Term Evolution-Railways.
- LTV** – Linear Time Varying.
- MHz** – Megahertz.
- MIMO** – Multiple-Input and Multiple-Output.
- MMSE** – Minimum Mean Square Error.
- mmWave** – Millimeter-Wave.
- MRC** – Maximum-Ratio Combining.
- MSE** – Mean Square Error.
- NLOS** – Non-Line-of-Sight.
- NMSE** – Normalized Mean Squared Error.
- NR** – New Radio.
- NSE** – Normalized Spectral Efficiency.
- OFDM** – Orthogonal Frequency Division Multiplexing.
- OTFS** – Orthogonal Time Frequency Space.
- PAPR** – Peak to Average Power Ratio.
- PDF** – Probability Density Function.
- PLC** – Programmable Logic Controller.
- PN** – Pseudo-Random Noise.
- QAM** – Quadrature amplitude modulation.

- ReLU** – Rectified Linear Unit.
- RNN** – Recurrent Neural Network.
- RS** – Reed–Solomon.

- SFFT** – Symplectic Fast Fourier transform.
- SNR** – Signal-to-Noise Power Ratio.

- USRP** – Universal Software Radio Peripheral.

- WIFI** – Wireless Fidelity.
- WLAN** – Wireless Local Area Network.

- ZP** – Zero Padding.
- ZT** – Zak Transform.

Table 1: Mathematical Notation and Operators

| Operator | Definition |
|-----------------------------|--|
| j | $\sqrt{-1}$ |
| $(\cdot)^*$ | Complex conjugate |
| $(\cdot)^T$ | Transpose |
| $ x $ | The absolute value of the scalar x |
| $\ \mathbf{x}\ $ | The Euclidean norm of the vector/matrix \mathbf{x} |
| $\ \mathbf{x}\ _F^2$ | The Frobenius norm of the vector/matrix \mathbf{x} |
| $\text{var}\{x\}$ | The variance value of the random variable x |
| $\mathcal{CN}(0, \sigma^2)$ | Complex normal distribution with zero mean and variance σ^2 |
| $[N]$ | A set including $\{1, 2, \dots, N\}$ |
| $\text{mod}(a, b)$ | The modulus function |

1

Introduction

Sommaire

| | | |
|-------|---------------------------------|----|
| 1.1 | Motivation | 19 |
| 1.2 | Challenges | 20 |
| 1.2.1 | Tube Structure | 21 |
| 1.2.2 | Ultra High Speed | 21 |
| 1.2.3 | Special Noise due to the Plasma | 21 |
| 1.2.4 | Handover | 21 |
| 1.3 | Related Works | 22 |
| 1.4 | Contributions | 23 |
| 1.5 | Thesis Outline | 24 |
| 1.6 | List of Publications | 26 |

1.1 Motivation

The rise of high-speed transportation systems, autonomous vehicles, and vehicle-to-vehicle communication presents new challenges, including ensuring reliable communications, robust data transmission, and seamless connectivity in high-mobility wireless channels [1]–[3]. Alongside these advancements, advancements in high-speed transportation technology are revolutionizing the way we travel, driven by the increasing demand for faster and more efficient systems.

Ultra-high-speed transportation systems, such as tube-based vacuum transportation, promise to achieve speeds up to 1200 km/h, significantly reduce travel times and improve connectivity between regions [4]. These innovative systems address several issues associated with traditional transportation, including pollution, traffic congestion, accidents, and high carbon emissions. Looking forward, the implementation of ultra-high-speed transportation systems will require advanced communication networks that meet high standards for quality, capacity, and reliability. These transportation systems require advanced communication architectures to support both operational control services and passenger services. Simultaneously, wireless communication systems have also experienced extraordinary growth over recent years. For example, cellular networks have evolved from First Generation Mobile Radio (1G) to Sixth Generation Mobile Radio (6G), moving from basic mobile voice features in 1G to integrating satellite networks in 6G, driven by user demand for higher data rates and better connectivity [5].

In this work, we will study about the wireless communication system design for ultra-high-speed scenarios in doubly selective channels. The application of this thesis is for the @TransPod company has been developing a new type of tube-transportation system, in which a vehicle known as the FluxJet is capable of achieving speeds of up to 1000 km/h inside a cylindrical metal tube under low-pressure conditions [4], [6], [7]. The FluxJet resembles an aircraft without wings but operates like a train. It is magnetically levitated and runs through the tube using electrically driven linear induction motors.

Pod-transportation requires a robust and reliable network architecture to facilitate data transfer between the pod, infrastructure, control system, and the station. Communication systems for pod-transportation are categorized into two separate networks: one for critical communication used for operational control services of the pod and a second network for passenger services. The first network requires low data rates but high reliability, while the second network demands high data rates and can tolerate lower reliability.

Our aim in this thesis is to design a high data rate pod-to-tube wireless communication system specifically for passenger services. To properly design such a system and predict its performance, the following steps are essential:

- **Transmission Channel Characteristics:** The basis phase requires the knowledge of the characteristics of the transmission channel, based on the evaluation of its impulse response.
- **Physical Layer Design:** The second phase focuses on designing the physical layer, particularly the modulation and waveform design. Waveform design refers to the strategies for packing information symbols within a given bandwidth and time resource, forming the basic building block of communication systems. Waveform design should satisfy a comprehensive set of metrics that can include orthogonality of the basis functions in a multipath channel, ease of channel estimation with low pilot overhead, the complexity of equalization, low PAPR, robustness to synchronization errors.

1.2 Challenges

The unique and specific configuration of the TransPod system presents significant challenges for reliable communication. These specific conditions affect the communication system design and introduce constraints which may restrict the design flexibility. The challenges can be summarized into the following categories:

1.2.1 Tube Structure

The specific propagation environment of the TransPod system causes several challenges. The guideway is constructed from highly reflective metal, leading to numerous reflections from the walls. This results in significant multipath propagation effects, causing a time-dispersive or frequency-selective channel.

1.2.2 Ultra High Speed

The ultra high speed of the pod results in severe Doppler effects, which is particularly problematic for Orthogonal Frequency Division Multiplexing (OFDM) systems. These effects disrupt the orthogonality of the subcarriers, leading to Inter Carrier Interference (ICI) [8]. Multipath components experience different Doppler shifts due to varying angles of arrival and relative velocities. These Doppler shifts contribute to Doppler spread, causing the transmitted signal to spread in the frequency domain. Consequently, the channel becomes frequency-dispersive or time-selective. Additionally, in a fast time-varying channel, the channel coherence time is reduced. This leads to channel distortion within a single symbol time, making channel estimation more challenging as it must be performed within this short coherence time.

1.2.3 Special Noise due to the Plasma

The vehicle in the guideway is powered using a patented plasma-based high-speed power transmission system. Plasma is used to carry electric current to the vehicle without contact. Since the power transmission system and communication system will exist in the same environment inside a steel guideway, a signal at the receiver of the communication system can be contaminated by a kind of impulsive noise. In the presence of such noise, the information packages at the receiver might be completely lost.

1.2.4 Handover

The vehicle inside the tube is traveling at very high speeds, pass through multiple communication zones in a very short period, thus the handovers must be performed in

a very short time to avoid additional delays. This rapid movement requires frequent and very fast handovers. Additionally, high speeds cause the channel conditions to change rapidly, making it challenging to maintain a stable communication link long enough to perform a handover without interruption.

1.3 Related Works

Wireless communication design for pod-to-ground communication in tube-transportation systems remains largely unexplored in current literature. As it is similar to the tunnel scenario in the High Speed Railway (HSR), we review the wireless communication technologies that have been studied or applied in HSR including Global System for Mobile communications-Railways (GSM-R), Long Term Evolution-Railways (LTE-R), Wireless Fidelity (WIFI), 38 GHz Millimeter-Wave (mmWave) technology [9].

GSM-R is the established standard for railway communication, primarily supporting train control systems. It offers a maximum data rate of less than 200 kbps, insufficient for high data rate communication inside the trains [10]. LTE-R is envisioned to replace GSM-R and being a Fourth Generation Mobile Radio (4G) protocol, is suitable for HSR systems that require low latency and high data rates. It supports communications for vehicles traveling at maximum speed of 500 km/h [11].

Wireless Local Area Network (WLAN) including WiFi, based on IEEE 802.11 standards, is typically adopted in low-speed indoor scenarios with short coverage, and is not designed for high-mobility applications [12].

In terms of the cellular networks, 4G LTE supports wireless access at mobile speeds up to 350 km/h. Meanwhile, fifth generation new radio (5G-NR) introduces scalable subcarrier spacing to provide suitable numerology sets for high speed transportation. However, the standardized manuscript from 3rd Generation Partnership Project (3GPP) indicates that 5G-NR supports a maximum speed of 500 km/h [13].

mmWave Fifth Generation Mobile Radio (5G) was suggested to provide high data rates for the passengers in HSR services [14]. In the [15], the performance of the mmWave system at high mobility of up to 500 km/h is evaluated. The 38 GHz mmWave wireless

communication technology is applied in Shanghai maglev system, providing a capacity reach up to 100 Mbps but at the speed of lower than 500 km/h [16], [17]. Massive MIMO in OFDM system proposed to compensate Doppler effects in [18].

Some studies propose an antenna-based solution by installing the leaky-waveguide antennas for 5G communication along the top of vacuum tubes. This method aims to eliminate Doppler frequency shift, thereby maintaining wireless signal coverage for passengers inside the pod [19]–[21].

Despite all the advancements mentioned above, the current railway communication systems cannot support the requirements of the pod-to-ground communication for ultra high speed systems.

1.4 Contributions

The main contributions of this PhD thesis work can be summarized as follows:

- **Modeling of noise in the plasma-based contactless power transmission system for TransPod [22]:**

We analyzed the high-voltage signals associated with the plasma arc discharge in the TransPod contactless power transmission system. Using a two-state Markov-Gaussian model, we modeled the impulsive noise contaminating the received signal at the receiver. This model minimizes the differences between observed measurement values and predicted values. Detailed results of this analysis are provided in [chapter 3](#).

- **Sequence-pilot-based channel estimation method in Orthogonal Time Frequency Space (OTFS) systems: [23]**

Ultra-high-speed scenarios and doubly selective channels present significant challenges in wireless communication systems. OTFS systems are suited to address these conditions due to their robustness in such environments. Despite this robustness, accurately estimating the channel in OTFS systems is essential for optimal performance. To address this, we conducted an investigation of sequence-based channel estimation using CAZAC sequence pilot. Our findings demonstrate that

utilizing CAZAC sequence pilot improve estimation accuracy compared to traditional impulse-based methods, while also reducing PAPR, making it suitable for real-time implementation in OTFS systems. Detailed discussion is provided in [chapter 4](#).

- **DNN-based channel estimation method in OTFS systems utilizing CAZAC sequence pilot: [24]**

Building upon the advancements in sequence-based channel estimation, we have applied a Deep Neural Network (DNN)-based channel estimation method using CAZAC sequences for OTFS systems. This method takes advantage of the properties of CAZAC sequences to improve the performance of the DNN model. Combining CAZAC sequences with the DNN-based estimator significantly improved channel estimation accuracy compared to traditional methods, under varying pilot power ratios. By optimizing the DNN architecture with two layers and a 20 number of neurons, we achieved a balance between estimation accuracy and computational efficiency. This approach achieves the same estimation accuracy with less pilot power, thereby reducing PAPR. Detailed findings are presented in [chapter 5](#).

1.5 Thesis Outline

In this thesis, we focus on channel modeling and physical layer design to improve the performance of high data rate communication systems in high mobility wireless channels, particularly the TransPod system. The thesis is structured as follows:

Chapter 2 introduces a review of wireless channels particularly the doubly-selective channels along with the different representations. We review the signal distortions due to the channel impairments. We discuss the fundamentals of OFDM systems in brief along with some disadvantages associated with them in ultra high mobility scenarios. Then we study the basic fundamentals of OTFS modulation system, and introducing different OTFS variants as well as comparing in terms of spectral efficiency and transmit power.

Chapter 3 characterizes the transmission channel in the TransPod guideway, utilizing a 2D ray-tracing model to achieve the channel impulse response along with large-scale and small-scale characteristics such as delay profile, Doppler profile and path loss evaluation. We also introduce the plasma-based power transmission system of TransPod. The effect of impulsive noise from the plasma power transmission is analyzed and modeled. To mitigate the corrupted transmission due to the noise, the appropriate channel coding techniques are briefly studied. A dual-link communication solution is proposed to overcome the frequent disconnectivity due to the fast handovers.

Chapter 4 proposes a correlation-based channel estimation method for OTFS systems by inserting a CAZAC sequence pilot into the zero bins of the ZP-OTFS system. We begin by reviewing the conventional channel estimation technique that uses a single impulse pilot, highlighting its limitations, particularly under conditions of low pilot power. Conventional methods struggle with estimation accuracy when pilot power is low, often requiring an increase in pilot power to achieve satisfactory performance. This increase in pilot power, however, leads to a higher PAPR of the transmitted signal. Our correlation-based method makes benefit of correlation properties of CAZAC sequence, achieves high estimation accuracy while maintaining low pilot power, resulting in efficient power usage and lower PAPR in the time domain signal.

Chapter 5 explores the application of DNN for channel estimation in OTFS systems, beginning with an exploration of the motivation behind using neural network techniques to improve estimation accuracy particularly in the scenarios with fractional Doppler effect. It reviews related works, including background on neural networks and the management of datasets for training, validation, and testing. The chapter details the proposed DNN architecture, including its design and implementation specifics. Additionally, it presents an analysis of simulation results, examining factors such as pilot power, DNN architecture, transmitter-receiver distances, and the impact of Signal-to-Noise Power Ratio (SNR) on model performance.

Chapter 6 summarizes the entire thesis and also suggests potential methodologies and approaches for future advancements.

1.6 List of Publications

Conference papers

1. B. Kazemzadeh, R. Janzen, V. Meghdadi, H. Meghdadi, and A. Bradai, “Globe-com 2023-2023 iee global communications conference,” pp. 4958–4963, 2023.
2. B. Kazemzadeh, R. Janzen, H. Meghdadi, V. Meghdadi, and A. Bradai, “Modeling of noise due to a plasma-based contactless power transmission system for ultra-high-speed transportation,” p. 149, 2023

Journal paper

1. B. Kazemzadeh, A. k. Gizzini, V. Meghdadi, H. Meghdadi, R. Janzen, and A. Bradai, “Deep Learning Based Channel Estimation in ZP-OTFS Modulation Systems utilizing CAZAC Sequence Pilot (submitted),” IEEE Communications Letters, 2024.

2

Wireless Channel Background

Sommaire

| | | |
|-------|---|----|
| 2.1 | Introduction | 29 |
| 2.2 | Large-Scale Fading | 30 |
| 2.3 | Small-Scale Fading | 30 |
| 2.3.1 | Multipath (Time Dispersion / Frequency-Selective) | 31 |
| 2.3.2 | Time-Variance (Frequency Dispersion / Time-Selective) | 31 |
| 2.3.3 | Doubly Selective Channels | 32 |
| 2.4 | Representations of Wireless Channels | 32 |
| 2.4.1 | Time-Delay Representation of LTV Channels | 33 |
| 2.4.2 | Time-Frequency Representation of LTV Channels | 34 |
| 2.4.3 | Delay-Doppler Representation of LTV Channels | 37 |
| 2.4.4 | Virtual relation between time-frequency and delay-Doppler representations | 39 |
| 2.5 | OFDM Review | 42 |
| 2.5.1 | OFDM disadvantages | 44 |
| 2.6 | OTFS Modulation | 46 |
| 2.6.1 | System Model | 46 |

Chapitre 2 – CHAPTER 2. WIRELESS CHANNEL BACKGROUND

| | | |
|-------|--------------------------------------|-----------|
| 2.6.2 | OTFS Transmitter | 48 |
| 2.6.3 | Wireless Channel | 50 |
| 2.6.4 | OTFS Receiver | 51 |
| 2.6.5 | OTFS input-output relation | 52 |
| 2.6.6 | OTFS Variants | 53 |
| 2.7 | Summary | 57 |

THIS chapter begins by introducing the physical phenomena associated with Linear Time Varying (LTV) channels [25]. Next, we provide background information on different representations of LTV channels. An overview of OFDM communication systems is provided, pointing out some drawbacks in high mobility scenarios. Finally, we introduce the basic concepts of OTFS modulation, with more detailed discussions in subsequent chapters.

2.1 Introduction

In wireless communication, data transmission involves emitting a modulated electromagnetic wave at a specific carrier frequency through a transmitter antenna. The corresponding receiver antenna captures the wave's energy. These processes are influenced by radio wave propagation, which is affected by the propagation environment. Given the unpredictability of the propagation environment in wireless systems, a thorough understanding of the wireless channel is essential for designing effective communication systems. As the transmitted radio wave travels, it encounters multiple paths due to scattering objects in the environment. Furthermore, movement of the transmitter, receiver, and these scatterers induces the Doppler effect, characteristic of a LTV channel. The LTV channel causes the transmitted wave to experience significant fluctuations in received power at the receiver. These variations in the received signal amplitude over time and frequency are commonly referred to as fading. The received power of the transmitted wave can be modeled by considering a combination of physical

phenomena, including path loss, large-scale fading, and small-scale fading [25]–[27].

2.2 Large-Scale Fading

Large-scale fading includes variations in the average received signal strength due to signal transmission over long distances and the impact of complete or partial Line-of-Sight (LOS) path loss caused by obstacles in the signal path. The free space model is one way to estimate the average signal strength for long distances between transmitter and receiver.

Free Space Model: The free space propagation model can be used where there is a direct LOS and no obstacle between the transmitter and the receiver, such as satellite communication systems [27], [28]. This model is used for predicting the received signal strength in the LOS environment and provide a way to estimate the path loss as a function of the distance. The received power at distance d , is expressed by the well-known Friis equation [29]:

$$P_r(d) = \frac{P_t G_t G_r \lambda^2}{(4\pi)^2 d^2}, \quad (2.1)$$

where P_t represents the transmit power, G_t the transmitter antenna gain, G_r the receiver antenna gain, and λ is the wavelength. When we talk about the antenna gain, we refer to the fact that the directivity leads to the power being concentrated in particular directions [30].

2.3 Small-Scale Fading

Small-scale fading involves rapid variations in both amplitude and phase of a radio signal, occurring over a short period of time (on the order of seconds) or a short distance (a few wavelengths). Instantaneous received signal power can fluctuate significantly with even minor movements of the receiver over a fraction of a wavelength. These fluctuations result from constructive and destructive superposition of transmitted signal echoes via different propagation paths, known as multipath propagation. The small-scale fading

experienced by the signal through a wireless channel, depends on the signal parameters, such as bandwidth, symbol period, and the channel parameters like multipath delay spread and Doppler spread. These parameters introduce time and frequency dispersion, leading to either frequency-selective fading, time-selective fading, or both [28], [31].

2.3.1 Multipath (Time Dispersion / Frequency-Selective)

A channel becomes time dispersive when the transmitted signal encounters various paths from different scatters. This results in delayed and attenuated replicas of the original signal, causing the signal to spread out in time domain after traversing the channel. Such channels exhibit frequency selectivity, where different frequency components of the signal experience different channel gain. Coherence bandwidth B_c , as an important parameter for frequency-selective channels, is defined as the range of frequencies over which the channel is approximately constant, and is proportional to the inverse of the delay spread of the channel τ_{max} , that is $B_c \propto 1/\tau_{max}$. Normally, in a high rate wireless transmission, the channel impulse response presents a delay spread larger than the symbol period of the transmitted signal T_s , and the signal bandwidth B_s exceeds the channel coherence bandwidth, ($\tau_{max} > T_s$ and $B_s > B_c$). The short symbol duration, compare to the multipath delay spread, leads to significant overlap of multiple delayed copies with subsequent symbols, causing Inter Symbol Interference (ISI) [28], [31], [32].

2.3.2 Time-Variance (Frequency Dispersion / Time-Selective)

A channel becomes frequency dispersive due to the movement of the transmitter, receiver, or scatterers, causing the Doppler effect. In these scenarios, the emitted wave undergoes the Doppler effect, leading to frequency shifts. The Doppler shift, denoted by the ν , is proportional to the relative velocity between receiver and transmitter v and the carrier frequency f_c :

$$\nu = \frac{vf_c}{c} \cos \alpha, \quad (2.2)$$

where c represents the speed of light, and α is the angle between the direction of the received signal and the direction of the motion. In environments with multipath

propagation and moving elements, received echoes exhibit different Doppler shifts due to varying angles and velocities. This leads to the spreading of the transmitted signal in the frequency domain, known as frequency dispersion. Depending on the extent of the Doppler spread, the received signal may undergo fast or slow fading.

It should be noted that, with ν_{max} being the maximum Doppler shift, the Doppler spectrum bandwidth B_d is given as $B_d = 2\nu_{max}$. Coherence time T_c is a parameter for the time-variant channels which is the time duration over which the channel impulse response can be considered as constant, $T_c \propto 1/B_d$. In fast fading channels, the coherence time is shorter than the symbol period, leading to rapid variations in the channel impulse response within a single symbol period. In these scenarios, the Doppler spread is greater than the bandwidth of the transmitted signal ($T_c < T_s$ and $B_s < B_d$). Conversely, in slow fading scenarios where the Doppler spread is much smaller than the bandwidth of the baseband transmit signal, the channel impulse response varies slowly compared to the duration of the baseband transmit signal [28], [31].

2.3.3 Doubly Selective Channels

Wireless channels that are affected by both time and frequency selectivity are known as doubly selective. These channels, also referred to as doubly dispersive or LTV channels. In such channels, the received signal is a superposition of several time delayed and frequency shifted replicas of the transmitted signal. This results in a fast time-varying channel condition. In doubly dispersive channels, the delay spread is typically large, and both the transmitter and receiver often exhibit relatively high-speed movement. As a result, channel estimation and equalization in doubly selective channels present significant challenges from a communication perspective [25], [33].

2.4 Representations of Wireless Channels

We introduced the doubly selective channels, where both time and frequency variations affect signal transmission and lead to performance degradation. A doubly selective or time-variant multipath channel can be represented in different domains, including time-delay, time-frequency, and delay-Doppler, each provides some insights about channel

behavior [25], [34], [35]. Understanding each representation and the corresponding parameters is necessary for modeling the impulse response of the channel.

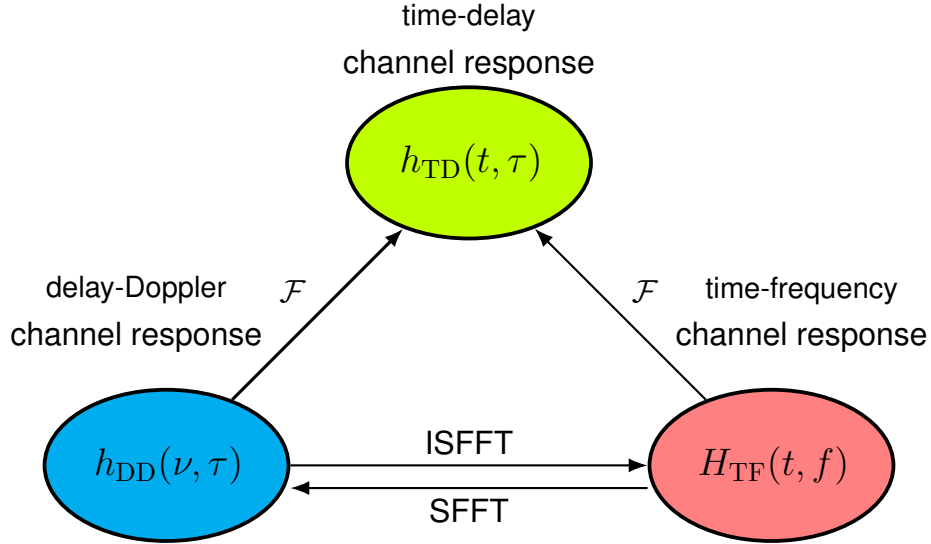


Figure 2.1: Different domain representations of LTV channel

Consider a time-varying multipath channel operating at carrier frequency f_c . The signal $s(t)$ is transmitted through the channel and $y(t)$ is the received signal. Additionally, we assume the LTV channel has P discrete propagation paths, with h_p , τ_p , and ν_p representing the complex fading coefficient, time delay, and Doppler frequency for the p -th path ($1 \leq p \leq P$), respectively. Our objective is to develop the mathematical representation of wireless channel in every domain.

2.4.1 Time-Delay Representation of LTV Channels

An LTV channel can be modeled as a linear filter with a time varying impulse response $h_{TD}(t, \tau)$, which acts on $s(t)$ and yielding $r(t)$. The time-varying impulse response of the channel can be represented as:

$$h_{TD}(t, \tau) = \sum_{i=1}^P h_i e^{2j\pi\nu_i(t-\tau)} \delta(\tau - \tau_i). \quad (2.3)$$

The input-output relationship between $s(t)$ and $r(t)$ with the noiseless assumption is given by

$$\begin{aligned} r(t) &= \int h_{\text{TD}}(t, \tau) s(t - \tau) d\tau \\ &= \sum_{i=1}^P h_i s(t - \tau_i) e^{2j\pi\nu_i(t - \tau_i)}. \end{aligned} \quad (2.4)$$

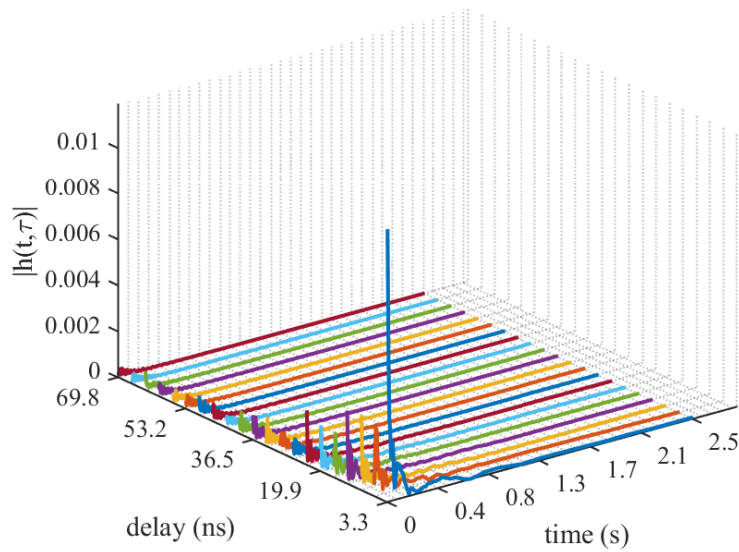


Figure 2.2: Time-delay representation of a doubly selective channel.

According to (2.4), the time-delay domain channel has P separable responses at the given delays for all the time domain components. It can be seen in the Figure 2.2 that the time-delay representation of the channel is sparse in the delay domain, but dense in the time domain. However, the effect of Doppler shift is not evident in time-delay channel representation.

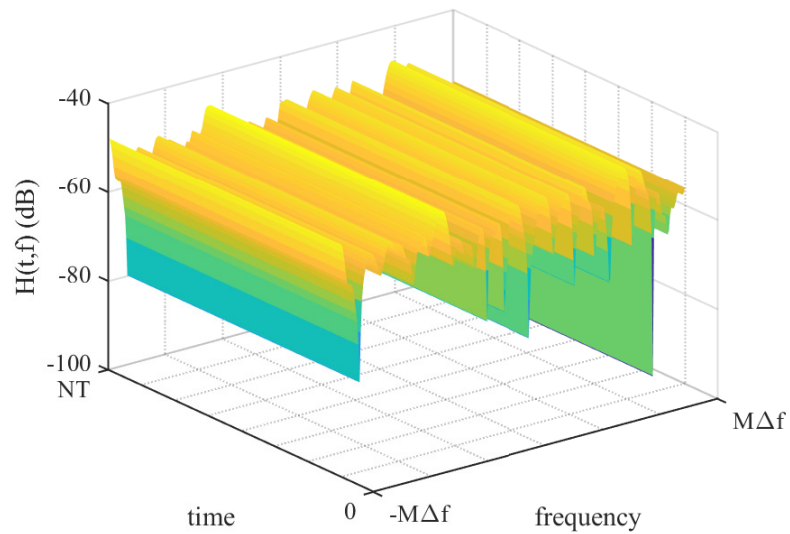
2.4.2 Time-Frequency Representation of LTV Channels

The joint time-frequency selectivity of an LTV channel is characterized by the time-frequency (or time-varying) transfer function. The time-frequency domain can be obtained by performing the Fourier transform along the delay domain to the time-delay

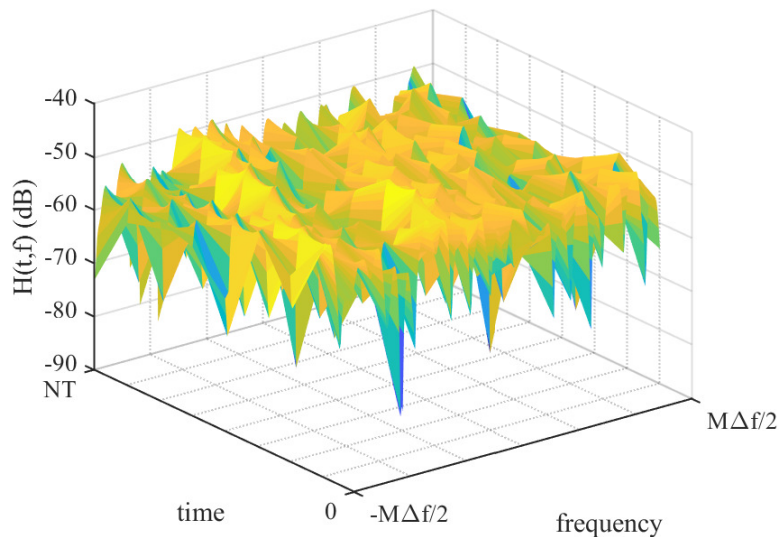
channel response $h_{\text{TD}}(t, \tau)$ in (2.3):

$$\begin{aligned} H_{\text{TF}}(t, f) &= \int_{-\infty}^{\infty} h_{\text{TD}}(t, \tau) e^{-j2\pi f\tau} d\tau \\ &= \sum_{i=1}^P h_i e^{2j\pi(\nu_i t - \tau_i f)}, \end{aligned} \quad (2.5)$$

It should be noted that, the term $e^{-2j\pi(\nu_i t - \tau_i f)}$ in the above equation representing a constant phase shift and can be absorbed into the channel coefficient h_i . The function $H_{\text{TF}}(t, f)$ represents the channel complex attenuation factor at a specific time t and frequency f . The LTV channel can be assumed stable within the coherence time and coherence frequency. Therefore, this representation is characterized by the maximum delay spread and Doppler spread and the channel coefficients vary significantly in the high mobility scenarios. Figure 2.3a shows a frequency selective channel in time-frequency domain which is time-invariant. Whereas Figure 2.3b illustrates the time-frequency representation of a channel that is selective in both time and frequency, displaying a dense distribution across the entire time-frequency plane. In doubly selective cases, the channel response varies with each time and frequency samples and accurately reconstructing the Channel State Information (CSI) requires estimating a large number of parameters due to significant variations in both dimensions.



(a) $H(t, f)$, time-invariant multipath channel



(b) $H(t, f)$, time-variant multipath channel

Figure 2.3: Time-frequency channel representation of a doubly selective channel vs. a frequency selective channel (time-invariant)

OFDM, which operates in the time-frequency domain, is particularly effective in static or low-mobility settings where channel conditions show minimal variation over time [32]. In these settings, OFDM utilizes a structured approach with orthogonal sub-carriers to manage multipath propagation. In these conditions, it is sufficient to estimate the channel at the beginning of each OFDM symbol and assume it remains constant

throughout the symbol duration. In high-mobility scenarios, as shown in [Figure 2.3b](#), the channel characteristics vary rapidly over time and frequency, leading to an increased number of unknown parameters, which complicates the estimation of the channel in real time. This involves advanced channel estimation and equalization techniques to effectively handle the rapid variations in order to maintain reliable communication.

2.4.3 Delay-Doppler Representation of LTV Channels

The wireless channel is not an arbitrary collection of complex numbers, and it is governed by simple physics, composed of a collection of reflectors, some of which are static and some of which are moving. The transmitted waveform propagates through the medium. The signal that arrives at the receiver is a superposition of the direct signal and the reflected echoes. Each of the reflected echoes at the receiver introduce a small distortion, which is a combination of time delay relates to the range of the reflector and Doppler shift relates to the velocity between the reflector and the transmitter/receiver. Therefore, we can parameterize each reflector as a pair of delay and Doppler and a certain complex number which represent the complex gain of the reflector. As a result, the geometry of reflectors can be mapped into a two-dimensional input response on the delay-Doppler grid. The LTV channel can be intuitively characterized using time delays and Doppler frequency shifts, and can be mathematically modeled through the delay-Doppler impulse response. The delay-Doppler (DD) domain can be obtained by performing the Fourier transform along the time of the time-delay channel response $h_{\text{TD}}(t, \tau)$ in (2.3):

$$h_{\text{DD}}(\tau, \nu) = \int_{-\infty}^{\infty} h_{\text{TD}}(t, \tau) e^{-j2\pi t\nu} dt. \quad (2.6)$$

Here, $h_{\text{DD}}(\tau, \nu)$ describes how delayed and Doppler-shifted version of the transmitted signal $s(t - \tau)e^{j2\pi\nu t}$, contributes to the receive signal $r(t)$:

$$r(t) = \int_{-\infty}^{\infty} \int_{-\infty}^{\infty} h_{\text{DD}}(\tau, \nu) e^{j2\pi\nu t} s(t - \tau) d\tau d\nu \quad (2.7)$$

As discussed previously, three channel representations are interchangeable by means of canonical transforms, as shown in [Figure 2.1](#). The transformation between the time and frequency representations is carried by the Fourier transform. The transition between the delay-Doppler and the time-frequency representations is achieved through a pair

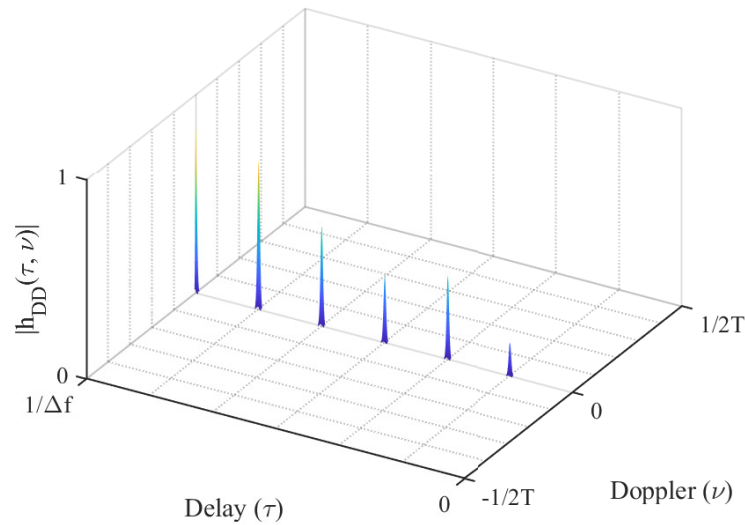
of two-dimensional transforms, Symplectic Fast Fourier transform (SFFT) and Inverse Symplectic Fast Fourier transform (ISFFT) as:

$$h_{\text{DD}}(\tau, \nu) = \int_{-\infty}^{\infty} \int_{-\infty}^{\infty} H(t, f) e^{-j2\pi t\nu} e^{j2\pi f\tau} dt df = \sum_{i=1}^P h_i \delta(\tau - \tau_i) \delta(\nu - \nu_i), \quad (2.8)$$

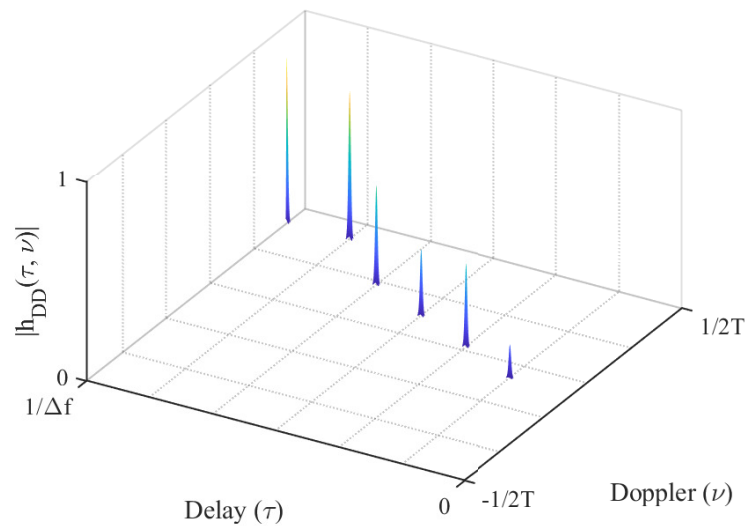
$$H(t, f) = \int_{-\infty}^{\infty} \int_{-\infty}^{\infty} h_{\text{DD}}(\tau, \nu) e^{j2\pi t\nu} e^{-j2\pi f\tau} d\tau d\nu = \sum_{i=1}^P h_i e^{2j\pi(\nu_i t - \tau_i f)}, \quad (2.9)$$

where (2.8) and (2.9) define the operations for SFFT and ISFFT operations, respectively. The SFFT involves a pair of Fourier transforms; converting time to delay through the Fast Fourier Transform (FFT), and frequency to Doppler through the Inverse Fast Fourier Transform (IFFT). Delay-Doppler channel response in (2.8) illustrates that channel responses are sparse in delay-Doppler domain, unlike the dense time-frequency domain. Furthermore, the peaks corresponding to different paths are separable.

These properties are illustrated in Figure 2.4 displaying the delay-Doppler representations for both doubly selective and time-invariant channels. The nonzero coefficients in the delay-Doppler channel representation at each location (τ, ν) represents the magnitude of the complex gain for a path with the specified delay τ and Doppler shift ν . Figure 2.4 is the equivalent representation of Figure 2.3 with the $P = 4$ number of paths. Figure 2.4a shows delay-Doppler representation of a time-invariant channel, where each path characterized by a delay time τ_i and a Doppler shift $\nu_i = 0$, $0 \leq i \leq 3$. However, in a doubly selective channel, as shown in Figure 2.4b, the responses from different paths are separated in both delay and Doppler directions.



(a) $h_{DD}(\tau, \nu)$, frequency selective channel



(b) $h_{DD}(\tau, \nu)$, double selective channel

Figure 2.4: Time-frequency channel representation of a Doubly selective channel vs. a static multipath channel (linear time-invariant)

2.4.4 Virtual relation between time-frequency and delay-Doppler representations

We consider the transmitted signal $s(t)$ spans a single frame on a time-frequency grid. The entire duration T_s is NT seconds, divided into N time slots, each lasting T seconds. Additionally, there are M subcarriers spaced Δf apart, resulting in a total bandwidth of

$M\Delta f$. By applying (2.9) and (2.8), we use the ISFFT to map the signal from the time-frequency grid to the delay-Doppler grid. The resulting delay-Doppler grid maintains the same number of points but on different scales.

To achieve a virtual channel representation in the delay-Doppler grid, the delay axis is sampled with a resolution of $\Delta\tau = \frac{1}{M\Delta f}$ seconds, capturing the smallest difference in delay representable by the delay-Doppler grid. Simultaneously, the Doppler axis is sampled with a distance of $\Delta\nu = \frac{1}{NT}$, representing the smallest variation in speed or Doppler shift than can be captured by the delay-Doppler grid. Consequently, the delay-Doppler grid is divided into multiple boxes of area $\Delta\tau \times \Delta\nu$. Figure 2.5 illustrates the discrete time-frequency grid and delay-Doppler grid.

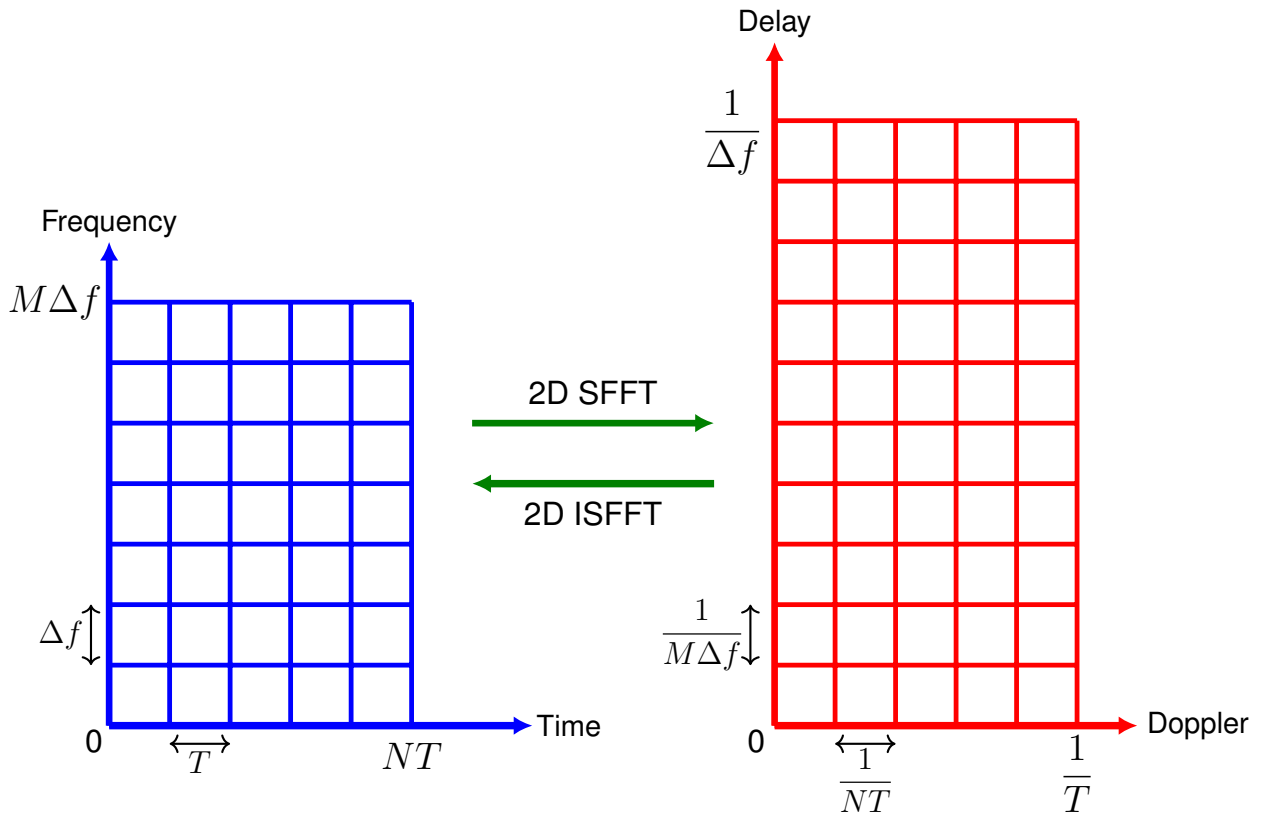


Figure 2.5: Discrete time-frequency grid and delay-Doppler grid.

For the i th path, $i = 1, \dots, P$, the corresponding delay τ_i and Doppler shift ν_i are given by:

$$\tau_i = \frac{l_i}{M\Delta f}, \quad \nu_i = \frac{k_i}{NT}, \quad (2.10)$$

where, l_i and k_i represent the normalized delay and normalized Doppler shift, respectively. $\tau_i \leq \tau_{max}$, where τ_{max} is the channel delay spread, and l_{max} corresponds to the associated normalized delay. Similarly, we have $\nu_i \leq \nu_{max}$, where ν_{max} signifies the channel maximum Doppler shift. Figure 2.6 shows a LTV channel with delay spread τ_{max} and Doppler spread $2\nu_{max}$. Each box, containing some points, corresponds to an existing path of the channel with the associated delay and Doppler values. Some boxes may contain multiple points, each contributing to a single, resolvable delay and Doppler values. The area of the points denotes the amplitude of the complex gain of each propagation path.

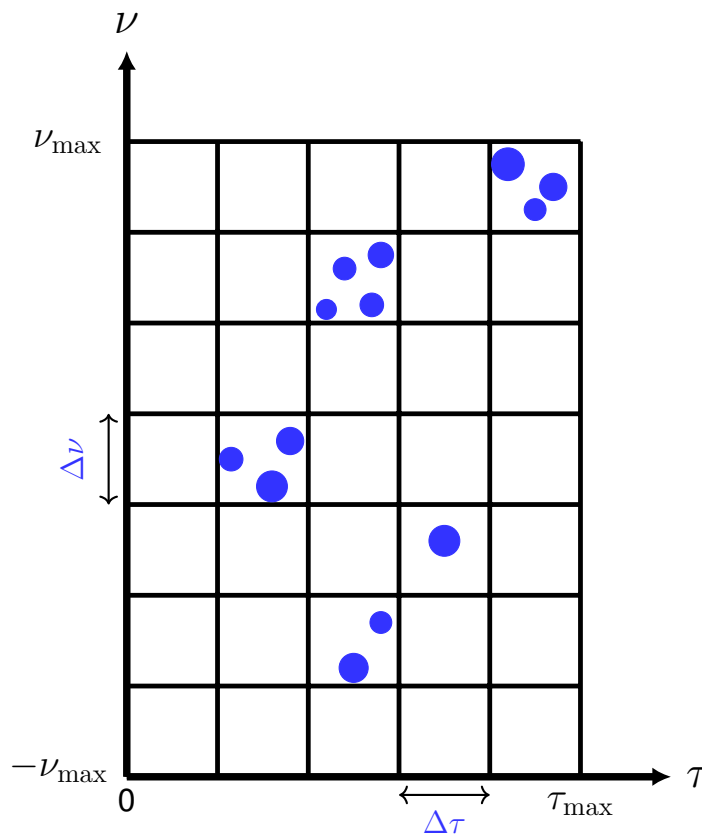


Figure 2.6: Channel representation in delay-Doppler domain with existing paths.

Physical Layer Modulation Techniques

The objective of the physical layer design is to develop a waveform that can mitigate the effects of fading and signal variations caused by the channel, thus meeting the needs

of modern applications. The traditional OFDM waveform has been the standard in 4G LTE due to its high performance in mitigating multipath effects and its low complexity of equalization [27], [36]. However, it does not perform well with fast time variations in high mobility environments. To overcome these limitations, a new modulation technique called OTFS has been proposed [37], showing performance improvements over classical OFDM in dynamic environments [38]. This thesis will explore the design of waveform that perform well in LTV wireless channels. In the subsequent section, We will review the classical OFDM-based system, which operates in the time-frequency domain, and the OTFS-based system which modulates information in the delay-Doppler domain.

2.5 OFDM Review

OFDM is a modulation technique that divides a high-rate data stream into several lower-rate streams. OFDM has been widely deployed in the 4G [36], [39] and the 5G cellular systems [40] as well as in WiFi networks [41] and DVB family [42], [43]. This technology is particularly effective for systems experiencing frequency-selective fading, where the channel remains constant within one OFDM symbol period. The fundamental concept of OFDM involves dividing the frequency-selective channel into smaller sub-channels. Each sub-channel occupies only a fraction of the overall bandwidth, enabling them to experience a flat-fading channel. These subcarriers maintain orthogonality, ensuring no Inter-Carrier Interference (ICI), facilitating the simultaneous transmission of multiple data streams. Orthogonality is achieved by spacing the sub-carriers in frequency so that they are integer multiples of $\frac{1}{T}$, where T is the duration of an OFDM symbol. Subcarrier spacing depends on factors such as channel frequency selectivity, rate of channel variations, phase noise, and the Doppler effect.

Consider an OFDM symbol with bandwidth $B = M\Delta f$ and duration T , where M is the number of subcarriers, and $\Delta f = 1/T$ is the subcarrier spacing. QAM information symbols are organized in the time-frequency plane, forming an information symbol matrix $\mathbf{X} \in \mathbb{C}^{M \times N}$ containing N OFDM symbols. For simplicity, we focus on a single OFDM symbol ($N = 1$). Let $\mathbf{x} \in \mathbb{C}^{M \times 1}$ be the column vector of \mathbf{X} containing the M information symbols. Applying an M -point Inverse FFT denoted by \mathbf{F}_M^H on \mathbf{x} produces

time-domain samples \mathbf{s} :

$$\mathbf{s} = \mathbf{F}_M^H \mathbf{x}. \quad (2.11)$$

To prevent ISI, a Cyclic Prefix (CP) of length l_{\max} is appended to \mathbf{s} , resulting in \mathbf{s}' . These time-domain samples are then transmitted into the channel. Passing the OFDM signal through a multipath channel causes the samples to spread in time. A multipath time-invariant channel with P propagation paths can be expressed as:

$$h(\tau) = \sum_{i=1}^P h_i \delta(\tau - \tau_i), \quad (2.12)$$

where h_i represents the complex channel coefficient of the i th path. The time-domain received signal \mathbf{r}' after passing through the channel is obtained as:

$$\mathbf{r}'[q] = \sum_{i=1}^P h_i \mathbf{s}'[q - l_i], \quad q = 0, \dots, M + l_{\max} - 1 \quad (2.13)$$

By defining $\mathbf{h} = [h_0, \dots, h_{\max}]^T$ as the discrete time channel vector, the time domain input-output relation is expressed as:

$$\mathbf{r}' = \mathbf{h}' * \mathbf{s}', \quad (2.14)$$

where \mathbf{r}' and \mathbf{s}' have length $M + l_{\max}$ due to CP.

After removing the CP and the first l_{\max} samples of the received signal \mathbf{r}' , we obtain the time-domain received signal \mathbf{r} . Note that the linear convolution of vectors \mathbf{h} and \mathbf{s} of length M is converted to circular convolution due to the CP:

$$\mathbf{r} = \mathbf{h} \circledast \mathbf{s}, \quad (2.15)$$

where \circledast denotes the circular convolution, and $\mathbf{h} = [\mathbf{h}[0], \dots, \mathbf{h}[M-1]] = [h_0, \dots, h_{l_{\max}}, 0, \dots, 0]$. \mathbf{r} and \mathbf{s} are of length M without CP.

After applying an M -point FFT on \mathbf{r} , the received frequency-domain samples \mathbf{y} are obtained:

$$\mathbf{y} = \mathbf{F}_M \mathbf{r} = \mathbf{H} \circ \mathbf{x}, \quad (2.16)$$

where \circ denotes element-wise multiplication, and $\mathbf{H} = [H_1, \dots, H_M] = \text{FFT}([h_1, \dots, h_{l_{\max}}, 0, \dots, 0])$

is the frequency-domain channel response. As a result, the m -th, $m = 0, \dots, M - 1$, received subcarrier can be obtained by element-wise multiplication of the channel frequency response and the transmitted symbols at the m -th subcarrier as:

$$\mathbf{y}[m] = \mathbf{H}[m]\mathbf{x}[m]. \quad (2.17)$$

When the frequency-selective channel does not change during an OFDM symbol, the frequency channel matrix \mathbf{H} is diagonal, which causes to low complexity one tap equalizer [44]. By transmitting pilot symbols, the channel frequency response can be estimated for every OFDM symbol, then one tap equalization is applied to estimate the transmitted symbols $\hat{\mathbf{x}}$:

$$\hat{\mathbf{x}}[m] = \frac{\mathbf{y}}{\hat{\mathbf{H}}[m]}, \quad (2.18)$$

where $\hat{\mathbf{H}}[m]$ are the estimated samples of the channel frequency response.

2.5.1 OFDM disadvantages

We have observed that OFDM has a simple transceiver architecture employing FFT and a simple one tap equalization. Despite its simplicity, OFDM is resilient to multipath effects, when the coefficients remain constant over time. However, OFDM struggles in time-varying channels, showing poor performance in high mobility scenarios due to Doppler spread. In the following, we highlight some major problems:

- **ICI:** In doubly selective channel, where Doppler shifts are also associated with each multipath component, channel coefficients change within an OFDM symbol duration. This time variation and Doppler shift destroy the orthogonality among subcarriers leading to ICI. We consider a doubly selective channel with P propagation paths where each is characterized by the gain h_i , delay time τ_i and Doppler shift ν_i . The equation (2.13) can be modified to include the Doppler effect, applying normalized delay l_i and normalized Doppler shifts k_i , as:

$$\mathbf{r}[q] = \sum_{i=1}^P h_i e^{j \frac{2\pi}{NM} k_i (q-l_i)} \mathbf{s}[q-l_i], \quad q = 0, \dots, M-1. \quad (2.19)$$

Due to the time-varying phase shift $e^{j \frac{2\pi}{NM} k_i (q-l_i)}$, the convolution in (2.15) is not

circular. In this case, the frequency domain channel matrix \mathbf{H} is a banded matrix, which means that the off-diagonal elements are not zero due to the energy leakage on adjacent subcarriers caused by the Doppler shift, resulting in ICI. The received signal on the m -th subcarrier include a second term represents ICI [45]:

$$\mathbf{y}[m] = \mathbf{H}[m]\mathbf{x}[m] + \text{ICI}, \quad (2.20)$$

If one-tap equalization in (2.17) is used, the system performance will be degraded. To mitigate ICI effect due to Doppler spread, increasing the subcarrier spacing in OFDM is a solution. However, increasing subcarrier spacing reduces the OFDM symbol time. If the length of CP is fixed, the ability of the system to handle ISI diminishes since the symbol time may become short compare to the delay spread of the channel. On the other hand, increasing CP length introduces higher overhead, as more time is spent transmitting redundant information rather than useful data. In 4G, LTE supports carrier bandwidths up to 20 MHz with a fixed CP duration and a fixed subcarrier spacing. However, in 5G, the modified version of OFDM has been used, named 5G New Radio (NR), introducing scalable numerology OFDM with the flexible sub-carrier spacing and CP length [46], [47].

- **Channel Estimation Error and High Pilot Overhead:** In frequency selective channels, the channel remains constant over OFDM symbols, allowing the estimated channel for one symbol to be used for other symbols. However, in doubly selective channels, the coherence time of the channel shrinks, causing the channel to change even within one OFDM symbol. Frequent pilot symbols insertion along time slots is required to capture rapid time variation of the channel, leading to increasing the system overhead. To keep the relative overhead fixed, the pilot density in frequency domain can be decreased that may not be sufficient to capture the frequency variations of the channel.

As a result, utilizing OFDM technique in doubly selective channels are often a trade off between pilot overhead, spectral efficiency and computational complexity. In the following, we will introduce the OTFS modulation system, which outperforms the conventional OFDM modulation for high-mobility double selective channels.

2.6 OTFS Modulation

In the preceding section, we discussed how OFDM has been widely used in 4G LTE due to its simple equalization process and its ability to mitigate the ISI by introducing a CP. However, in high-mobility environments with wide Doppler spreads, resulting in large frequency dispersion, conventional OFDM systems may struggle to maintain efficient and reliable communication. 5G NR employs a multi-numerology OFDM system to address various 5G requirements, including support for high-speed scenarios. Although increasing sub-carrier bandwidth in 5G NR can mitigate Doppler spread, the decrement of CP length can introduce ISI when delay spread is also significant. To tackle these challenges, a new modulation scheme called OTFS has been proposed in [48], showing significant performance improvements over OFDM. We observed that the delay-Doppler channel model accurately represents the wireless channel geometry compared to other models. OTFS operates based on this model, offering a solution to the limitations of multicarrier techniques over double dispersive channels by transforming the multipath channel into a sparser, slowly time-varying channel. Unlike OFDM, which modulates data in the time-frequency domain, OTFS modulates data in the delay-Doppler domain, to take the advantage of the channel model in this domain.

2.6.1 System Model

We consider an OTFS frame with M number of sub-carriers, each has Δf bandwidth, and N number of symbols each has T duration. OTFS system has a total bandwidth of $B = M\Delta f$ and total duration of $T_s = NT$. OTFS frame contains NM information symbols taken from a modulation alphabet (e.g., QAM), which are placed in the delay-Doppler domain matrix $X_{DD}[m, n]$.

There are two ways to implement OTFS modulation. One way is to implement OTFS directly in delay-Doppler domain via Zak Transform (ZT)/Inverse Zak Transform (IDZT), as seen in Figure 2.7 [49]–[51]. IDZT is the composition of ISFFT and IFFT. In this approach the information symbols $X_{DD}[m, n]$ are transformed directly to the time domain to get continuous signal $x(t)$ using the IDZT. The signal is transmitted into the double selective channel to get $y(t)$ signal at the receiver. Then we get $Y_{DD}[m, n]$ in the delay-Doppler domain.

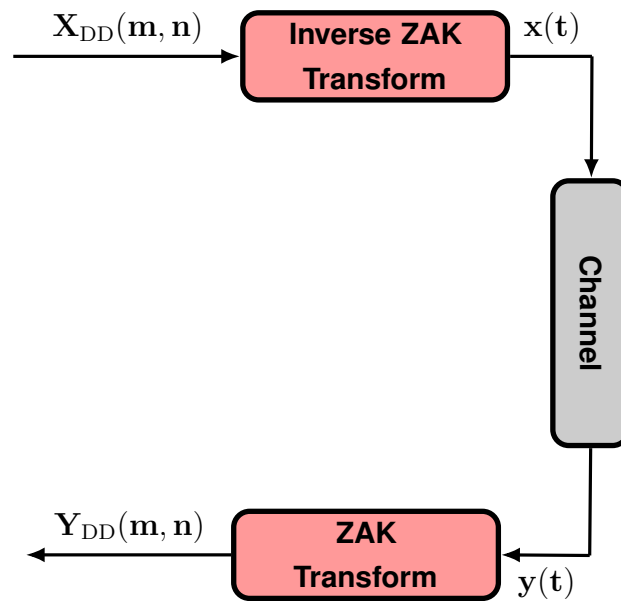


Figure 2.7: OTFS modulation implementation, direct approach

The second way is two-step approach via the time-frequency domain, as illustrated in [Figure 2.8](#) [37], [48]. The idea is to map the information symbols $X_{DD}[m, n]$ in the delay–Doppler domain to symbols $X_{TF}[k, l]$ in the time–frequency domain using the ISFFT. Then, the Heisenberg transform is applied to $X_{TF}[k, l]$ to create the time domain signal $x(t)$. After passing through the channel, at the receiver, the time-domain signal $y(t)$ is mapped to the time–frequency domain through the Wigner transform, and then to the delay–Doppler domain using SFFT for symbol demodulation.

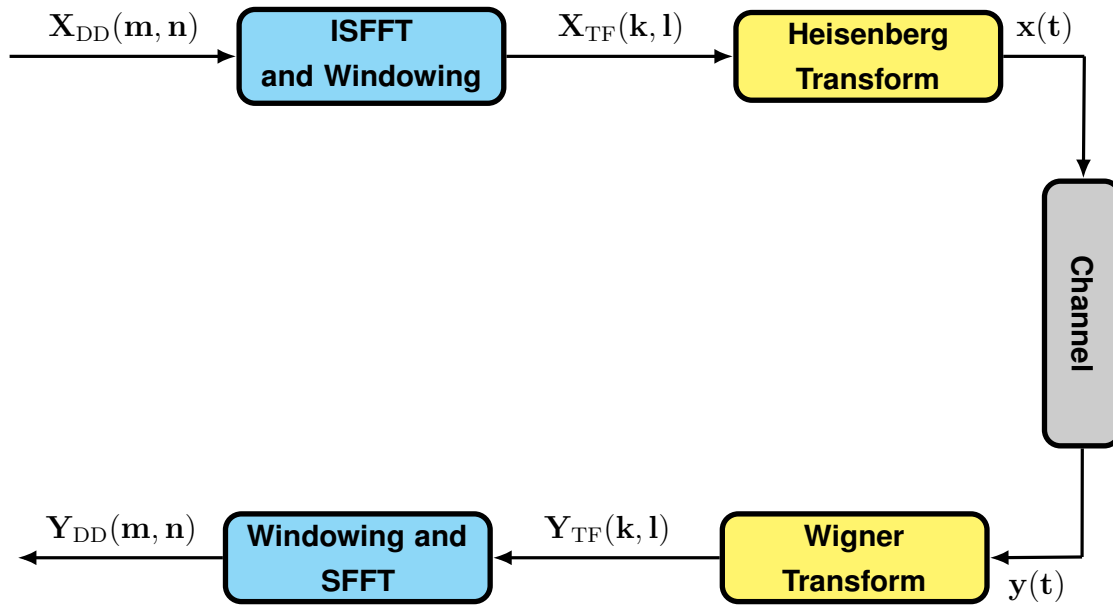


Figure 2.8: OTFS modulation implementation, two-step approach

The second approach has been widely considered in the literature, because it operates like pre-processing and post-processing in existing OFDM systems. More in details, the Heisenberg transform can be implemented by applying the conventional OFDM modulator which is IFFT module. And the Wigner transform can be implemented using the conventional OFDM demodulator through the FFT module [52], [53].

2.6.2 OTFS Transmitter

At the transmitter, the MN data symbols from a conventional modulation alphabet, like Quadrature amplitude modulation (QAM), are placed in the delay-Doppler domain matrix $\mathbf{X}_{DD} \in \mathbb{C}^{M \times N}$ with entries $X_{DD}[m, n]$, for $m = 0, \dots, M - 1$, $n = 0, \dots, N - 1$. They are transmitted in a packet with duration of NT in a bandwidth of $M\Delta f$. The delay-Doppler samples $X_{DD}[m, n]$ are mapped to time-frequency domain samples $X_{TF}[k, l]$, for $k = 0, \dots, M - 1$, $l = 0, \dots, N - 1$ by using ISFFT as:

$$\mathbf{X}_{TF}[k, l] = \frac{1}{\sqrt{NM}} \sum_{n=0}^{N-1} \sum_{m=0}^{M-1} \mathbf{X}_{DD}[m, n] e^{j2\pi \left(\frac{nl}{N} - \frac{mk}{M} \right)}. \quad (2.21)$$

As discussed in 2.4.4, ISFFT in (2.21) can be implemented using M -point Discrete Fourier Transform (DFT) on the columns of \mathbf{X}_{DD} and N -point Inverse Discrete Fourier

Transform (IDFT) on the rows of \mathbf{X}_{DD} . The equivalent matrix representation of (2.21) can be written as:

$$\mathbf{X}_{\text{TF}} = \mathbf{F}_M \mathbf{X}_{\text{DD}} \mathbf{F}_N^H. \quad (2.22)$$

Next, the Heisenberg transform is applied to $\mathbf{X}_{\text{TF}}[k, l]$ to create the time domain OTFS signal $x(t)$ transmitted over the wireless channel.

$$x(t) = \sum_{k=0}^{M-1} \sum_{l=0}^{N-1} \mathbf{X}_{\text{TF}}[l, k] g_{\text{tx}}(t - lT) e^{j2\pi k \Delta f (t - lT)}, \quad (2.23)$$

where $g_{\text{tx}}(t)$ is the pulse shaping waveform of duration T at the transmitter. In the matrix form we have:

$$\mathbf{X}_{\text{TD}} = \mathbf{G}_{\text{tx}} \mathbf{F}_M^H \mathbf{X}_{\text{TF}} \quad (2.24)$$

where $\mathbf{X}_{\text{TD}} \in \mathbb{C}^{M \times N}$ is the matrix containing the delay-time samples, and \mathbf{G}_{tx} is the matrix containing samples of $g_{\text{tx}}(t)$ as its elements:

$$\mathbf{G}_{\text{tx}} = \text{diag} [g_{\text{tx}}(0), g_{\text{tx}}(T/M), \dots, g_{\text{tx}}((M-1)T/M)] \in \mathbb{C}^{M \times M}.$$

The Heisenberg transform in (2.23) works similarly to the OFDM transformation, which is equivalent to M -point IFFT of the columns of \mathbf{X}_{TF} . The steps in (2.21) and (2.23) together constitute the OFDM-based OTFS modulation system, as seen in Figure 2.8.

Remark that in this work, we assume a rectangular pulse i.e:

$$g_{\text{tx}}(t) = \begin{cases} 1 & \text{if } 0 \leq t \leq T \\ 0 & \text{otherwise,} \end{cases} \quad (2.25)$$

therefore, \mathbf{G}_{tx} becomes an $M \times M$ identity matrix, i.e. $\mathbf{G}_{\text{tx}} = \mathbf{I}_M$.

By considering the rectangular pulse shape at the transmitter, (2.22) and (2.24), the time-domain transmit sample matrix can be obtained by:

$$\mathbf{X}_{\text{TD}} = \mathbf{I}_M \mathbf{F}_M^H \mathbf{F}_M \mathbf{X}_{\text{DD}} \mathbf{F}_N^H = \mathbf{X}_{\text{DD}} \mathbf{F}_N^H \quad (2.26)$$

The (2.26) is equivalent to an IDZT. As illustrated in Figure 2.7, in the direct approach of OTFS, the blocks ISFFT and Heisenberg transform together represent the Zak-transform, which converts the two-dimensional information symbols to time-domain transmit signal.

Then, the time-domain vector $\mathbf{s} \in \mathbb{C}^{MN \times 1}$ is obtained by vectorization of \mathbf{X} :

$$\mathbf{s} = \text{vec}(\mathbf{X}_{\text{TD}}) \quad (2.27)$$

2.6.3 Wireless Channel

The signal $x(t)$ is transmitted over a doubly selective channel. Ignoring the noise component, the received signal $y(t)$ in time domain is given by (recall from (2.7)):

$$\begin{aligned} y(t) &= \iint h_{\text{DD}}(\tau, \nu) e^{j2\pi\nu(t-\tau)} x(t-\tau) d\tau d\nu \\ &= \int h_{\text{TD}}(t, \tau) x(t-\tau) d\tau. \end{aligned} \quad (2.28)$$

Considering a limited number of reflectors within the channel, characterized by P paths, each associated with delays τ_i , Doppler shifts ν_i , and gains h_i , delay-Doppler channel response $h_{\text{DD}}(\tau, \nu)$ is represented as:

$$h_{\text{DD}}(\tau, \nu) = \sum_{i=1}^P h_i \delta(\tau - \tau_i) \delta(\nu - \nu_i), \quad (2.29)$$

while the delay-time channel response, obtained as the Fourier transform of $h_{\text{DD}}(\tau, \nu)$ with respect to ν , is given by:

$$h_{\text{TD}}(t, \tau) = \sum_{i=1}^P h_i e^{j2\pi\nu_i(t-\tau)} \delta(\tau - \tau_i). \quad (2.30)$$

By sampling $y(t)$ at $t = \frac{qT}{M}$ with $q = 0, \dots, NM - 1$, and $\tau = \frac{l}{M\Delta f}$, the signal $y(t)$ is transformed into:

$$y[q] = \sum_{i=1}^P h_i \underbrace{e^{j2\pi \frac{k_i}{NT} (\frac{qT}{M} - \frac{l_i T}{M})}}_{\text{Doppler}} \underbrace{x[q - l_i]}_{\text{Delay}}. \quad (2.31)$$

It is worth noting that the term $e^{-\frac{j2\pi k_i l_i}{NM}}$ in the above equation, representing a constant phase shift, can be absorbed into the channel coefficient h_i . This equation can be reformulated in vector form as:

$$\mathbf{y} = \mathbf{H}\mathbf{x} + \mathbf{w}, \quad (2.32)$$

where \mathbf{H} is the $MN \times MN$ matrix:

$$\mathbf{H} = \sum_{i=1}^P h_i \Pi^{l_i} \Delta^{k_i}, \quad (2.33)$$

with Π the permutation matrix (forward cyclic shift),

$$\Pi = \begin{bmatrix} 0 & \cdots & 0 & 1 \\ 1 & \ddots & 0 & 0 \\ \vdots & \ddots & \ddots & \vdots \\ 0 & \cdots & 1 & 0 \end{bmatrix}_{MN \times MN}, \quad (2.34)$$

and Δ is the $MN \times MN$ diagonal matrix:

$$\Delta^{(k_i)} = \begin{bmatrix} e^{\frac{j2\pi k_i(0)}{MN}} & 0 & \cdots & 0 \\ 0 & e^{\frac{j2\pi k_i(1)}{MN}} & \cdots & 0 \\ \vdots & \ddots & \cdots & \vdots \\ 0 & 0 & \cdots & e^{\frac{j2\pi k_i(MN-1)}{MN}} \end{bmatrix}_{MN \times MN}, \quad (2.35)$$

both Π and $\Delta^{(k_i)}$ are explained in details in [54].

Furthermore, it is advantageous to represent $h_{\text{TD}}(t, \tau)$ in (2.30) in discrete form here, as it will be utilized in subsequent chapters. According to the above sampling process, the discrete delay-time channel response can be derived as:

$$h_{\text{TD}}[q, l] = \sum_{i=1}^P h_i e^{\frac{2j\pi}{MN} k_i (q-l_i)} \delta[l - l_i]. \quad (2.36)$$

2.6.4 OTFS Receiver

Let $y(t)$ be the time domain received signal at the receiver. First, the Wigner transform is used at the receiver side to transform the time domain received signal $y(t)$ to time-frequency domain signal $\mathbf{Y}_{\text{TF}}[l, k]$, by matching it with the receiver pulse shaping waveform $g_{\text{yx}}(t)$, i.e:

$$Y(t, f) = \int r(t') g_{\text{yx}}^*(t' - t) e^{-j2\pi f(t' - t)} dt' \quad (2.37)$$

$$\mathbf{Y}_{\text{tf}}[l, k] = Y(t, f)|_{t=lT, f=k\Delta f}.$$

The Wigner transform works similarly to the OFDM demodulation, so the (2.37) can be considered as FFT operation. The (2.37) can be written as matrix form:

$$\mathbf{Y}_{\text{TF}} = \mathbf{F}_M \mathbf{G}_{\text{yx}} \mathbf{Y}_{\text{TD}}, \quad (2.38)$$

where \mathbf{G}_{yx} is the receiver pulse shaping matrix, \mathbf{Y}_{TD} is the matrix containing MN delay-time received samples.

Next step is to apply SFFT on the time-frequency signal $\mathbf{Y}_{\text{TF}}[l, k]$ to obtain the delay-Doppler signal $\mathbf{Y}_{\text{DD}}[m, n]$ as:

$$\mathbf{Y}_{\text{DD}}[m, n] = \frac{1}{\sqrt{NM}} \sum_{k=0}^{M-1} \sum_{l=0}^{N-1} \mathbf{Y}_{\text{TF}}[k, l] e^{-j2\pi(\frac{nl}{N} - \frac{mk}{M})}. \quad (2.39)$$

In the matrix form, the (2.39) can be written as:

$$\mathbf{Y}_{\text{DD}} = \mathbf{F}_M^H \mathbf{Y}_{\text{TF}} \mathbf{F}_N. \quad (2.40)$$

Similar to transmitter side, for rectangular pulse shaping waveform $\mathbf{G}_{\text{yx}} = \mathbf{I}_M$, substituting (2.38) in (2.40) gives:

$$\mathbf{Y}_{\text{DD}} = \mathbf{Y}_{\text{TD}} \mathbf{F}_N. \quad (2.41)$$

The (2.41) is equivalent to ZT as shown in Figure 2.7. In direct approach of OTFS, the blocks Wigner transform and SFFT together constitutes the IDZT, which converts the received time domain signal to two-dimensional received symbols in the delay–Doppler domain.

2.6.5 OTFS input-output relation

In the case of having ideal pulses g_{tx} and g_{rx} as defined in (2.25), input-output relationship in the time-frequency domain is: [35], [48]

$$\mathbf{Y}_{\text{TF}}[k, l] = \mathbf{H}_{\text{TF}}[k, l] \mathbf{X}_{\text{TF}}[k, l]. \quad (2.42)$$

The element-wise product in (2.42) is transformed to the circular convolution of the channel and transmitted symbols in the delay-Doppler domain through SFFT:

$$\begin{aligned} \mathbf{Y}_{DD}[m, n] &= \mathbf{H}_{DD}[m, n] \circledast \mathbf{X}_{DD}[m, n] \\ &= \sum_{i=1}^P h_i \mathbf{X}_{DD} [[m - l_i]_M, [n - k_i]_N]. \end{aligned} \quad (2.43)$$

It is worth mentioning that the (2.43) is valid only for the ideal pulse waveform. In the practical cases and non-ideal pulses, the 2D circular convolution is twisted due to the phase rotations $\exp\left(\frac{j2\pi k_i(m-l_i)}{MN}\right)$ as:

$$\mathbf{Y}_{DD}[m, n] = \sum_{i=1}^P e^{\frac{j2\pi k_i(m-l_i)}{MN}} h_i \mathbf{X}_{DD} [[m - l_i]_M, [n - k_i]_N]. \quad (2.44)$$

For the non-ideal pulses which does not hold bi-orthogonality, there is energy leakage outside the time-frequency resources which can lead to the fractional Doppler case. However, this effect can be reduced by choosing the narrow pulses at the cost of decreasing the time-frequency resource efficiency [55].

2.6.6 OTFS Variants

The OTFS frame comprises MN samples, which are divided into N time slots or blocks, each containing M samples. To mitigate interference between the frames, a guard interval equal to or greater than the maximum channel delay spread l_{max} should be included in the form of either CP or Zero Padding (ZP). Various OTFS frame structures exist with regard to the insertion of CP or ZP, as well as adding the guard to the frame or block of OTFS.

- **Reduced ZP-OTFS or RZP-OTFS** : In this structure, a single ZP of length $L_{ZP} \geq l_{max}$ appends to the OTFS frame, seen in [Figure 2.9](#).

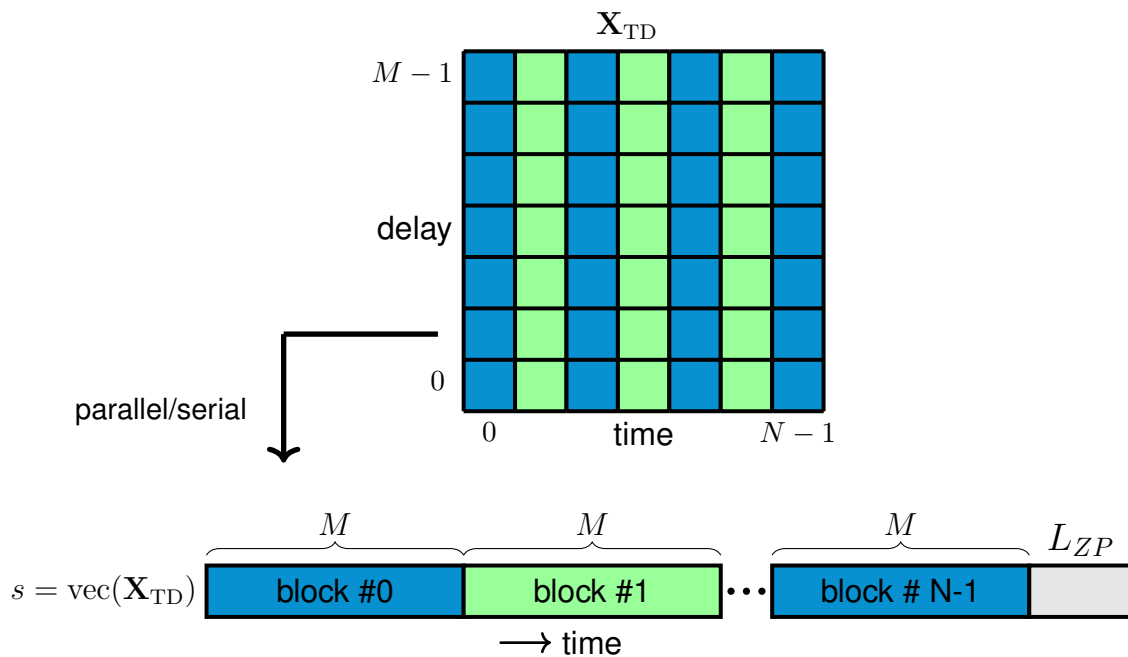


Figure 2.9: RZP-OTFS structure of OTFS time domain signal; ■, ■: data and ■: L_{ZP}

- **Reduced CP-OTFS or RCP-OTFS** : In this structure, a single CP of length $L_{CP} \geq l_{max}$ prepends to the OTFS frame, seen in [Figure 2.10](#).

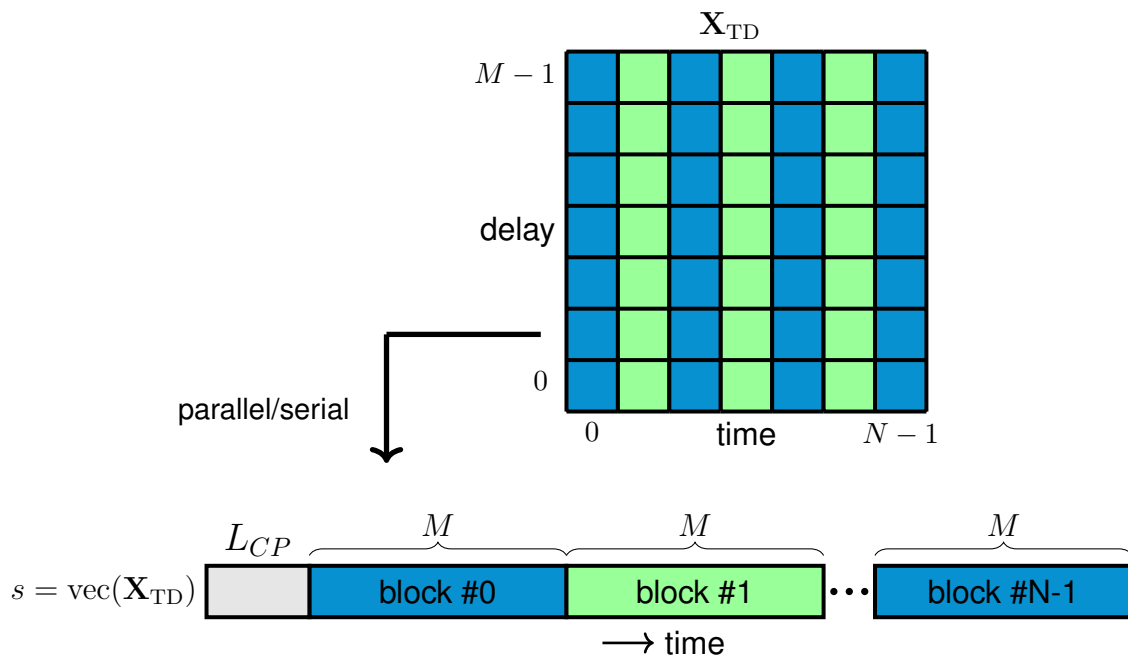


Figure 2.10: RCP-OTFS structure of OTFS time domain signal; ■, ■: data and ■: L_{CP}

- **ZP-OTFS** : In this structure, a ZP of length $L_{ZP} \geq l_{max}$ appends to each block of an OTFS frame, seen in [Figure 2.11](#).

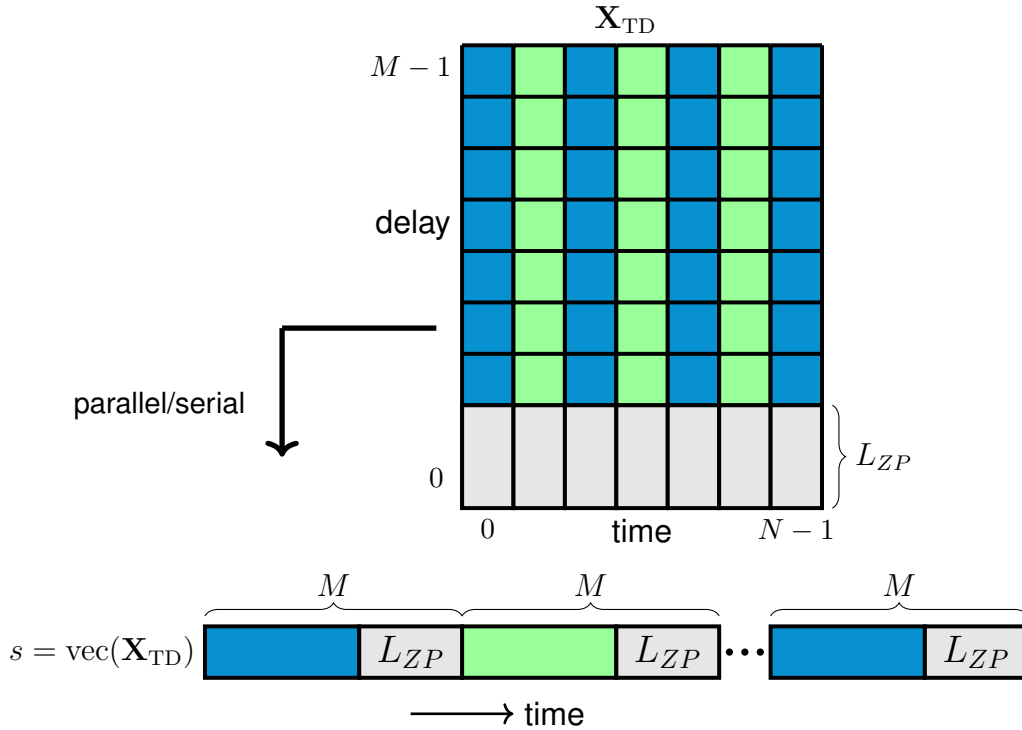


Figure 2.11: ZP-OTFS structure of OTFS time domain signal; ■, ■: data and ■: L_{ZP}

- **CP-OTFS** : In this structure, a CP of length $L_{CP} \geq l_{max}$ appends to each block of an OTFS frame, seen in [Figure 2.12](#).

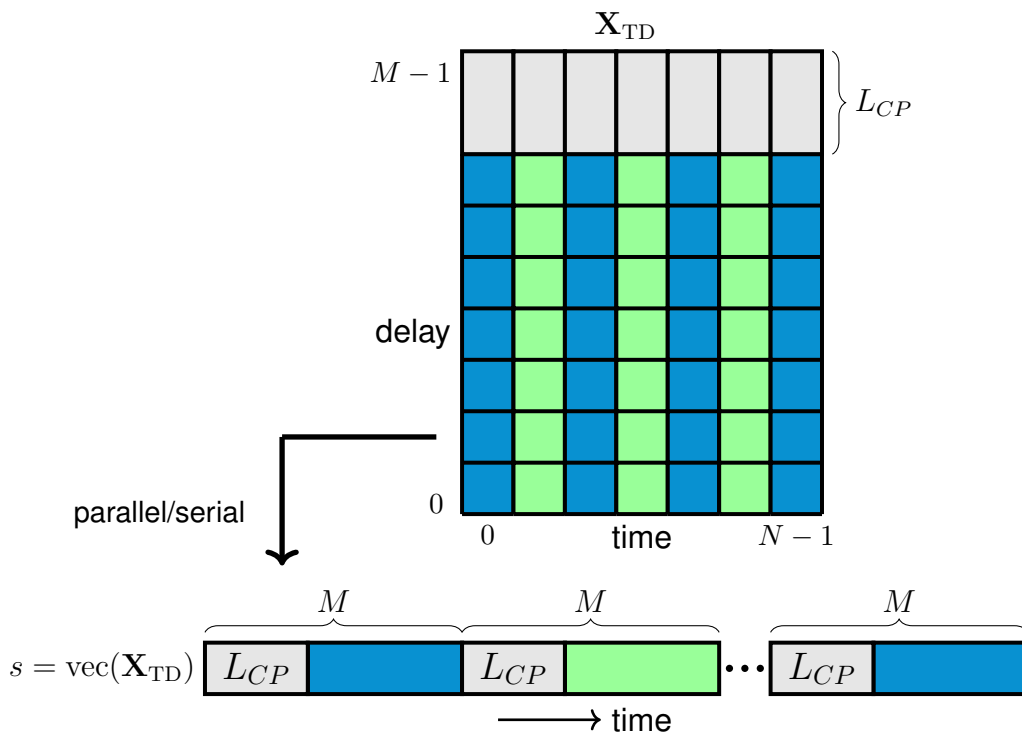


Figure 2.12: CP-OTFS structure of OTFS time domain signal; ■, ■: data and ■: L_{CP}

In [Table 2.1](#), we compare the different variants of OTFS, in terms of Normalized Spectral Efficiency (NSE) and the transmit power, P_{tr} . Noted that, E_s is defined as an average symbol energy of the modulation alphabets utilized in an OTFS frame. From the [Table 2.1](#) we conclude that, RZP/RCP-OTFS has higher NSE compared to the ZP/CP-OTFS variants due to the insertion of ZP/CP per frame. In terms of transmit power, it is obvious that ZP/RZP-OTFS has minimum required power compared to others, and CP-OTFS requires more power due to the L_{CP} additional guard samples are transmitted per block.

Table 2.1: Comparison of OTFS variants in terms of spectral efficiency and transmit power.

| | Normalized spectral efficiency (NSE) | transmit power (P_{tr}) |
|-----|--------------------------------------|-----------------------------|
| CP | $\frac{M}{M + L_{CP}}$ | $N(M + L_{CP})E_s$ |
| ZP | $\frac{MN}{MN + L_{ZP}}$ | NME_s |
| RCP | $\frac{MN}{MN + L_{CP}}$ | $(NM + L_{CP})E_s$ |
| RZP | $\frac{MN}{MN + L_{ZP}}$ | NME_s |

2.7 Summary

In this chapter, we provided a comprehensive background on LTV channels. We examined the signal distortions at the receiver caused by channel impairments such as large-scale fading, multipath effects, and the Doppler effect. Additionally, we introduced various representation domains of LTV channel, including time-delay, time-frequency, and delay-Doppler domains, and discussed the relationships between them. We reviewed the OFDM modulation technique operating in the time-frequency grid and highlighted some of the challenges of using OFDM in high-mobility LTV channels. Following this, we introduced OTFS, a newly proposed modulation technique that operates in the delay-Doppler domain and shows promise for high-mobility scenarios. Furthermore, we explored different variants of the OTFS system and compared them in terms of spectral efficiency and transmit power.

3

Channel Characteristics of Tube Transportation Ultra High Speed Systems

Sommaire

| | | |
|-------|---|----|
| 3.1 | Introduction | 60 |
| 3.2 | Ray Tracing in a Tube Transportation System | 62 |
| 3.3 | TransPod System | 64 |
| 3.4 | System Model | 65 |
| 3.4.1 | Path Loss | 66 |
| 3.4.2 | Delay spread | 77 |
| 3.4.3 | Doppler spread | 78 |
| 3.4.4 | Power-delay-Doppler profile | 80 |
| 3.4.5 | Time-Frequency Transfer Function | 81 |
| 3.5 | Plasma-based Power Transmission System | 82 |
| 3.6 | Impulsive Noise | 83 |
| 3.6.1 | Two-state Markov-Gaussian Model | 84 |
| 3.6.2 | Noise Measurements | 86 |

Chapitre 3 – CHAPTER 3. CHANNEL CHARACTERISTICS OF TUBE
TRANSPORTATION ULTRA HIGH SPEED SYSTEMS

| | | |
|-------|---|-----------|
| 3.6.3 | Data Analysis | 86 |
| 3.6.4 | Markov Chain Model | 90 |
| 3.6.5 | Numerical Results | 91 |
| 3.7 | Coding Techniques to Mitigate the Impulsive Noise | 93 |
| 3.8 | Proposed Architecture for Handover | 95 |
| 3.9 | Summary | 96 |

THE main aim of this chapter is to thoroughly explore the characteristics of the transmission channel in ultra-high-speed, tube-transportation systems such as TransPod [4], [6], [7]. We specifically examine both large-scale and small-scale characteristics. Additionally, we analyze how noise from the plasma power transmission system affects the communication system inside the guideway [56]. We also briefly discuss about the coding techniques to mitigate the impulsive noise effects.

3.1 Introduction

In the world of next-generation wireless systems, one of the key objectives is to support high-mobility scenarios, especially with the rapid evolution of transportation technologies. The tube-transportation system is a standout example, representing a significant advancement in ultra-high-speed rail technology. Unlike traditional high-speed trains with wheels, this system operates in a fundamentally different way [57]. The system offers significantly higher speeds while also posing unique challenges for wireless communication that require careful consideration. The special features, such as ultra-high-speed and a metal tube, highlight the need for reliable wireless communication in this environment [58]. To design wireless communication systems, it's crucial to understand the characteristics of the channel inside the tube and how signals behave when moving through it [59].

Channel models can be categorized primarily into empirical and theoretical models [60].

An empirical model relies on real-world data and observations instead of theoretical assumptions, developed through measurements and experiments. The accuracy of empirical models depends on how closely the estimated model parameters match the application environment [61]–[63]. The current theoretical approaches can be classified as the stochastic [64] and deterministic channel models [65], [66]. Deterministic models, on the other hand, use mathematical equations and parameters to describe the channel without considering uncertainties, offering a more predictable representation. In deterministic models, propagation mechanisms like reflection, absorption, diffraction, and refraction are applied to determine received signal strength. Deterministic channel models are further subdivided into numerical methods for solving Maxwell's equations, waveguide-based models [67], [68], the graph-based models [69], and ray tracing channel models [70]. Maxwell's equations mathematically describe electromagnetic field interactions, requiring detailed knowledge of physical object properties. Graph models can achieve a high modeling accuracy at a low computational cost, considering the infinite reverberation effect of electromagnetic waves [71], [72]. Ray tracing is commonly used in wireless communications, capturing crucial parameters such as Delay spread, Coherence bandwidth, Coherence time, and Doppler spread, along with obtaining the channel transfer function. This model is performed by tracing the path of the waves emitted from the transmitter and reach at the receiver. The waves include direct, reflected or scattered rays. The goal is to compute the number of valid rays at the receiver and to calculate the strengths of the waves to find out the path loss, total received power and channel transfer function [73]–[75].

In our study, the tube functions as a deterministic propagation environment with fixed dimensions. To advance towards our ultimate goal of employing the delay-Doppler representation of the channel in OTFS modulation, which closely corresponds to the physical geometric parameters of the environment, we utilize the ray tracing method. This enables us to establish a deterministic model of the wireless channel within the tube. This chapter outlines the construction of a 2D ray-tracing channel model, which incorporates both LOS and reflected paths, i.e. Non-Line-of-Sight (NLOS). Various properties such as reflection coefficients and incident phase which are influenced by the material dielectric constant in the environment, are also considered. With this model, we derive the channel impulse response and proceed to analyze both large-scale fading,

such as path loss, and small-scale fading characteristics, like delay spread and Doppler spread.

3.2 Ray Tracing in a Tube Transportation System

In our study, we utilize a model based on 2D ray-tracing technique to analyze and predict the propagation of communication signals within a tube-like environment. The tube is made of metal. This model, visually represented in [Figure 3.1](#), provides a framework for analyzing signal transmission in a tube characterized by its length D and radius r_1 . In the system, transmitters are placed along the inner wall of the tube, while a receiver is positioned on top or at the front of a train moving through the tube at a velocity v with radius r_2 . Our approach evaluates all potential signal paths from the transmitters to the receiver, including both LOS and NLOS paths, where the signals bounce off the walls of the tube before reaching the receiver.

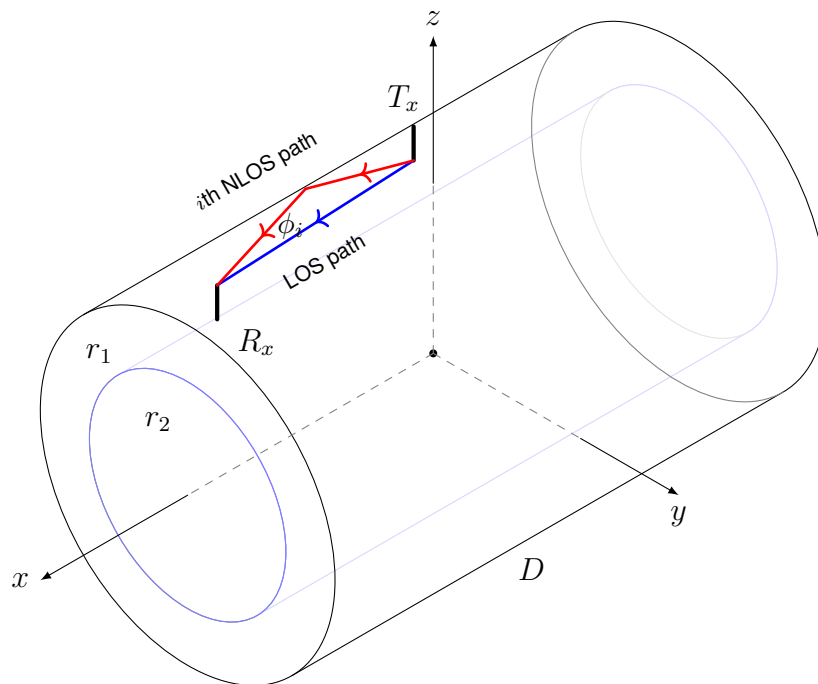


Figure 3.1

However, we only consider indirect paths whose signal strength doesn't drop below a certain level after bouncing around. The time-frequency channel impulse response is

described by the following equation [25], [26]:

$$H(t, f) = h_0 e^{2j\pi\nu_0 t} e^{-2j\pi\tau_0 f} + \sum_{i=1}^P h_i e^{2j\pi\nu_i t} e^{-2j\pi\tau_i f}, \quad (3.1)$$

in this equation, h_0 signifies the gain for the direct path, $\tau_0 = \frac{D_0}{c}$ denotes the propagation delay from the transmitter to the receiver with the direct path distance D_0 , and ν_0 represents the Doppler shift of the LOS path. The equation also includes h_i , representing the gain of each NLOS path, τ_i and ν_i , denoting their delay and Doppler shift, respectively. The delay for each NLOS path is computed relative to the LOS path delay, using the LOS path as a reference. Specifically, for a path with length D_i , the delay is $\tau_i = \frac{D_i - D_0}{c}$, and the Doppler shift is $\nu_i = \frac{v\phi_i}{\lambda} = \frac{f_c v\phi_i}{c}$, where c , v , λ , ϕ_i , and f_c are the speed of light, relative speed of transmitter and receiver, wavelength, arrival angle, and the carrier frequency, respectively. The gain of LOS path, P_0 is calculated using the Friis formula:

$$P_0 = G_{t0} G_{r0} \left(\frac{\lambda}{4\pi D_0} \right)^2, \quad (3.2)$$

where G_{t0} is the transmitter antenna gain corresponding to the LOS path, and G_{r0} is the receiver antenna gain associated with the LOS. Each NLOS path comprises reflections ranging from one to R . The power gain of these paths is determined as [29]:

$$P_i = G_{ti} G_{ri} \left(\frac{\lambda \prod_{r=1}^R \Gamma(\theta_r)}{4\pi D_i} \right)^2, \quad (3.3)$$

where G_{ti} and G_{ri} represent the transmitter and receiver antenna gain associated with i th path, respectively. Γ represents the reflection coefficient of the surface, and θ_r signifies the incident angle of the r th reflection component of i th NLOS path [29], [76], [77].

Once the power gain for each path is computed, the channel coefficients are generated. These coefficients are modeled as complex Gaussian random variables with a variance equal to the power gain of each path.

The reflection coefficient is defined as the ratio of the amplitude of the reflected wave (A_r) to the amplitude of the incident wave (A_i), $\Gamma = \frac{A_r}{A_i}$ [78]–[80]. In our study, the tube

is made of carbon steel. Metals are characterized by their high electrical conductivity, which significantly impacts how electromagnetic waves interact with them [81], [82]. When an electromagnetic wave encounters a metal surface, a significant portion of the wave is reflected and very little of the wave penetrates the metal. The absorbed part quickly attenuates due to the metal's high conductivity, which leads to the energy of the wave being absorbed and converted into heat. The reflection coefficient can range in magnitude from 0 to 1. For metals, the reflection coefficient is typically close to 1 due to the high reflection. From the S -parameters point of view, the reflection coefficient is directly related to S_{11} , which quantifies what portion of an incoming electromagnetic wave is reflected by the surface it encounters [83]. In the following, we will first examine the TransPod system as one of the tube-transportation systems and then evaluate our 2D ray-tracing channel model, particularly based on the TransPod system.

3.3 TransPod System

FluxJet, seen in Figure 3.2, a fully electric vehicle which is capable of speeds over 1000 km/h, has been unveiled by TransPod [6], [7].

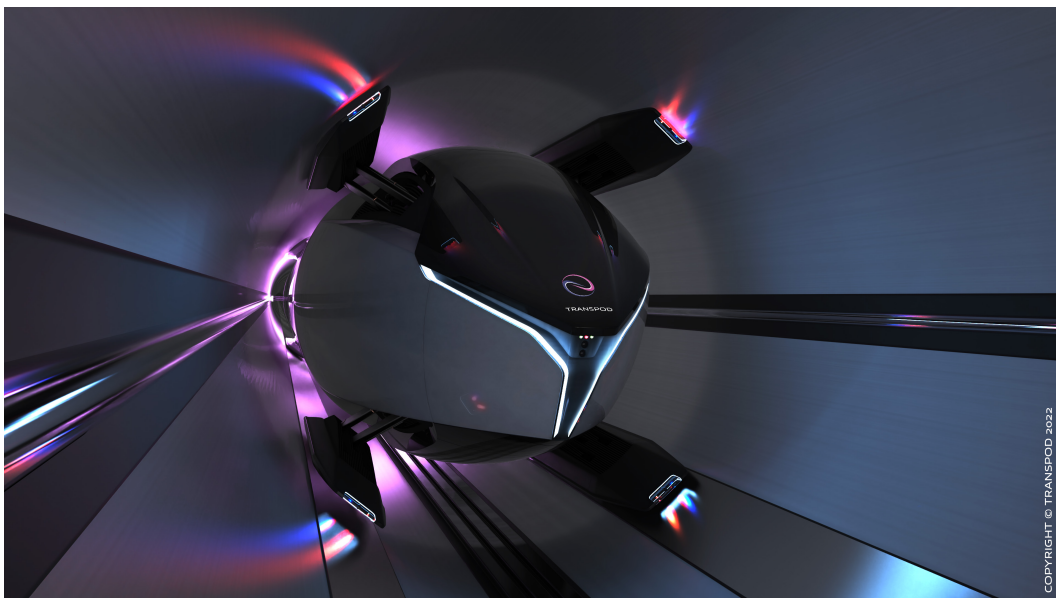


Figure 3.2: FluxJet vehicle inside a tube in TransPod line.

The infrastructure is a tube or guideway that allows multiple FluxJet vehicles to travel,

using electrically-powered propulsion. FluxJet is somewhat like an aircraft without wings [6]. The technology includes plasma-based power transmission [56], magnetic propulsion [84], [85], and veillance flux [86]–[88], as illustrated in Figure 3.3. The FluxJet operates on a patented plasma-based high-speed power transmission system [7], [56].

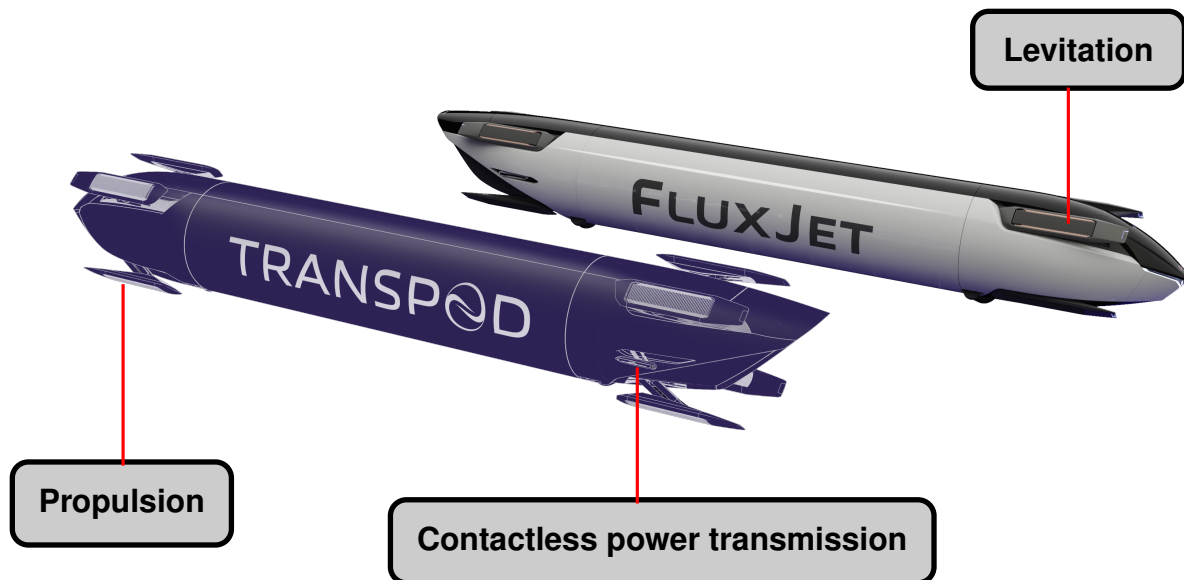


Figure 3.3: FluxJet main technologies

In more detail, the FluxJet is a contactless EMV (Electric, Magnetic, Veillance) vehicle that uses electric flux, magnetic flux, and veillance flux for power, propulsion, and control, without any contact between the vehicle and the guideway [7]. Plasma carries electric current to the vehicle without contact. The plasma is generated and controlled by power pickup systems on the vehicle, ensuring current flows across a contactless gap to deliver power from the grid to the vehicle [56]. The vehicle is then levitated and propelled using magnetic fields. Linear motors and power inverters on the vehicle create magnetic fields that move in a wave-like pattern, generating propulsive force through electromagnetic induction [7], [84], [85]. Finally, the vehicle's flight control system stabilizes motion in six axes by adjusting the magnetic fields [84].

3.4 System Model

In this section, we evaluate the simulation outcomes for the ray-tracing propagation channel model for the TransPod tube, as illustrated in Figure 3.4. The TransPod

infrastructure consists of a cylindrical carbon steel tube with a diameter of 4 meters, equipped with transmitters spaced every 700 meters along its length. Additionally, there is a receiver positioned at the front of the FluxJet. The FluxJet, constructed of concrete, has a diameter of 3.75 meters and can travel at speeds of up to 1000 km/h within the tube. The system operates at a carrier frequency of f_c with a bandwidth of 20 MHz. In the subsequent analysis, we examine simulation results of the channel time-varying impulse response, investigate path loss to understand the channel large-scale fading characteristics, and explore small-scale fading, including delay and Doppler profile.

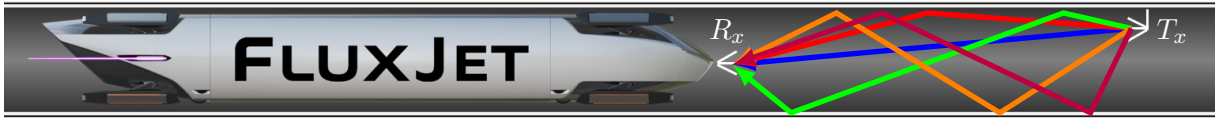


Figure 3.4: Simplified model of the multipath channel inside the tube.

3.4.1 Path Loss

According to the discussions in [section 3.2](#), we compute the power delay profile for each path based on the path loss as: [77]

$$P_L = -10 \log_{10} \left(\frac{P_r}{P_t} \right) = -10 \log_{10} \left[\left(\frac{\lambda}{4\pi} \right)^2 \left\| \frac{G_{t0}G_{r0}}{D_0} + \sum_{i=1}^P \frac{G_{ti}G_{ri}\Gamma_i \exp \left(\frac{j2\pi f_c(D_i - D_0)}{c} \right)}{D_i} \right\|^2 \right]. \quad (3.4)$$

Here, P_L denotes the path loss in dB, P_t represents the transmitted power, P_r stands for the received power at the receiver antenna. Γ_i denotes the total wall reflection attenuation, which varies based on the number of reflections from the wall corresponding to the i th path.

Given these configurations, detailed and complex computations are necessary due to the high number of reflections inside the tube. Another group in TransPod was expected to provide the precise channel model inclusive of all details; however, their input has not materialized. Consequently, we are constrained to utilize a simplified model. This simplified model considers a scenario where the transmitter T_x and receiver R_x are spaced D_s meters apart along a line in the middle of the tube, aligned with the direction

of movement, as illustrated in Figure 3.5. This simplified approach provides us with a general understanding of the channel characteristics within the tube, facilitating further exploration in wireless communication design.

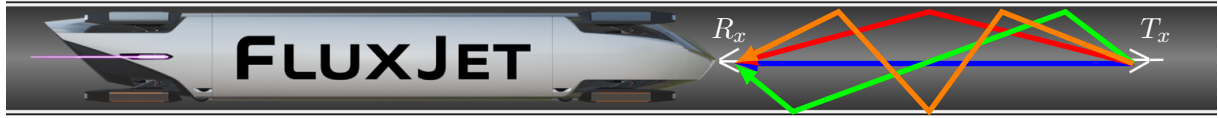


Figure 3.5: Simplified model of the multipath channel inside the tube.

According to (3.4), radio wave propagation and path loss depend on the signal frequency, electromagnetic properties of walls, and the radiation patterns of the transmitter and receiver antennas. In the following subsections, we explore the impact of these parameters. Initially, we present the theoretical Free-Space Path Loss (FSPL) model and compare it with the ray-tracing model of the tube. The calculation of FSPL, denoted as PL_{Free} , originates from the Friis transmission formula [29] and is computed as follows:

$$PL_{\text{Free}} = -10 \log_{10} G_t G_r \left(\frac{\lambda}{4\pi D_0} \right)^2. \quad (3.5)$$

For this discussion, we assume that both the transmitter and receiver use isotropic antennas with gains $G_t = G_r = 1$, operating at a carrier frequency of 2.45 GHz, with a reflection coefficient $\Gamma = 0.9987$. Figure 3.6 illustrates the path loss experienced as the FluxJet traverses the tube from 0 to 1400 m, with the transmitter positioned at 700 m. In the figure, the red curve represents the theoretical FSPL.

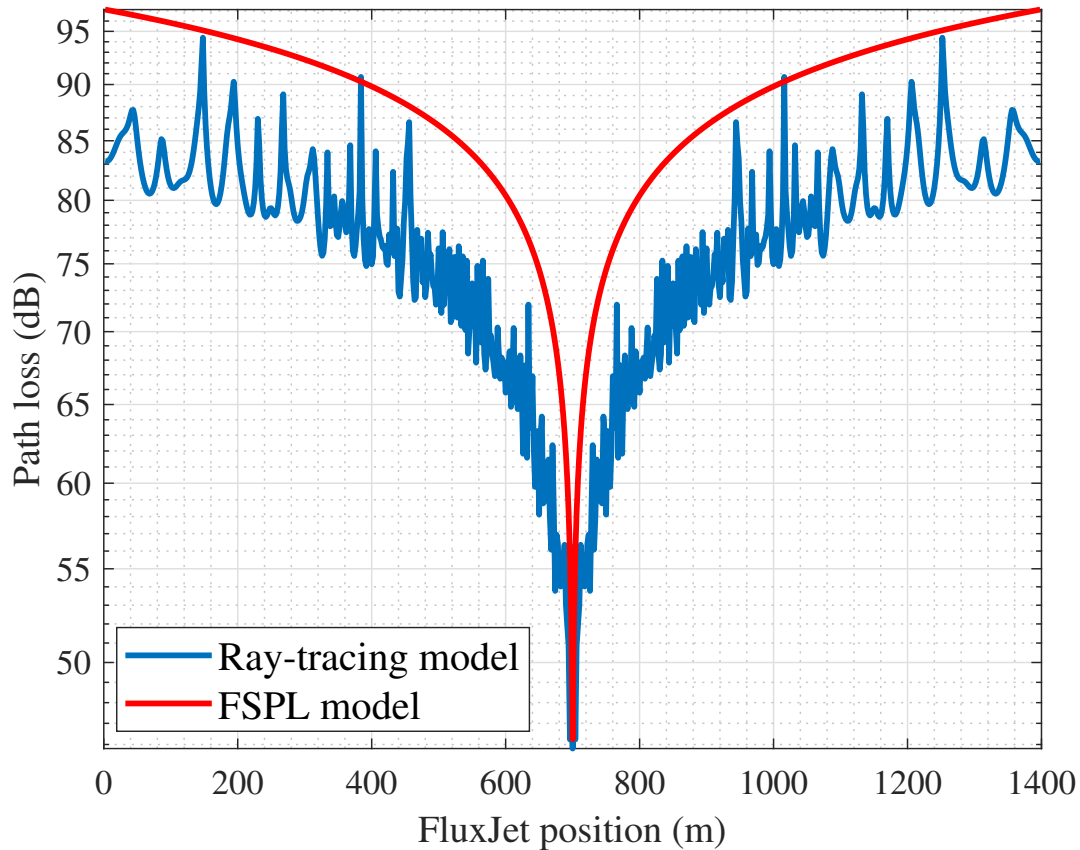


Figure 3.6: Path loss in the TransPod tube.

Observations indicate that the path loss within the tube is lower compared to free space. This difference is due to the reflections from the tube's metal surface, which conserve more energy during transmission than what is observed in free space. In free space, the absence of NLOS paths results in path loss increasing directly with distance at a fixed frequency. The blue curve, illustrating the path loss within the metal tube, shows significant reflected components as the receiver approaches the transmitter. These reflections due to the metal surface, help to minimize energy loss. However, as the distance between the transmitter and receiver increases, the LOS path becomes the dominant factor, leading to an increase in path loss proportional to the distance. An additional observation is the effect of fluctuations in the path loss curve within the metal tube which are attributed to multiple reflections from the metal walls.

In the following subsections, we analyze the effects of each parameter on path loss.

- **Carrier frequency:** Figure 3.7 illustrates the path loss at different carrier frequencies, as well as the FSPL models for those carrier frequencies. At each position, the path loss is increasing with the frequency, and the path loss of simulation results from the ray-tracing model, are lower than the result of FSPL.

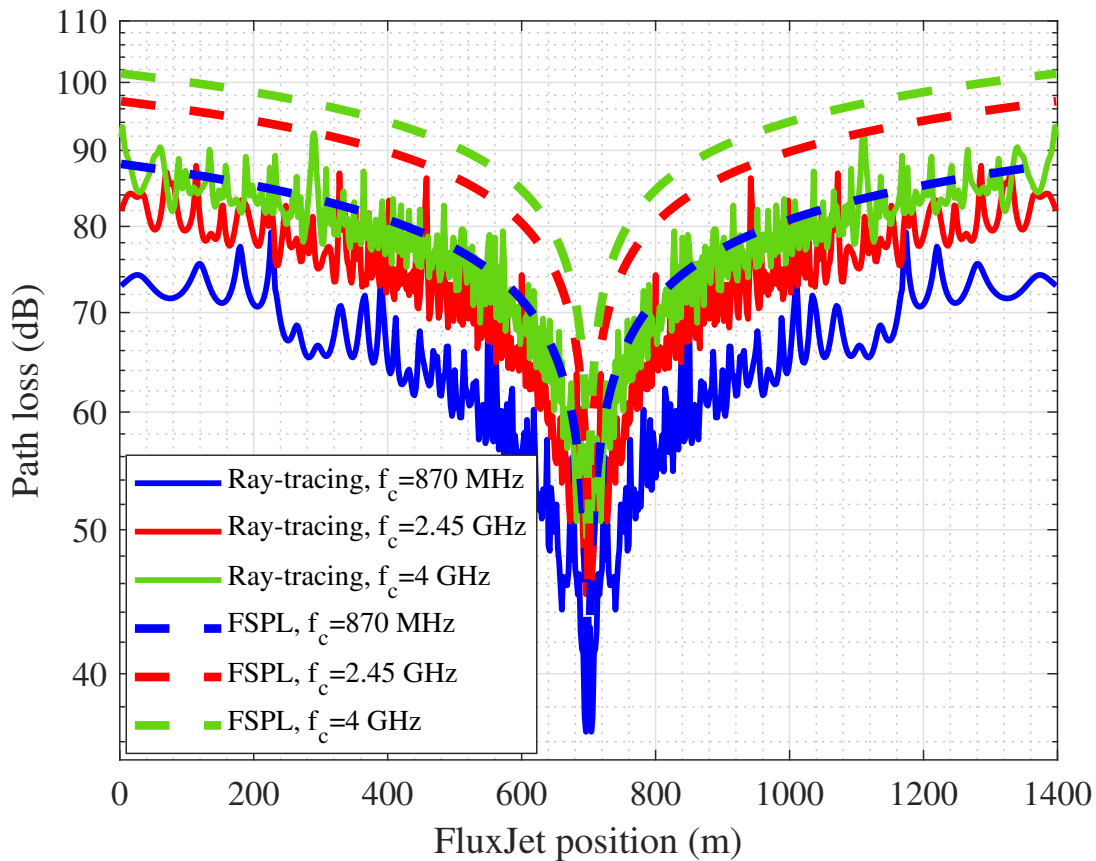


Figure 3.7: Path loss in the TransPod tube at the carrier frequencies 870 MHz, 2.45 GHz, and 4 GHz.

- **Reflection coefficient:** To examine the sensitivity of the model to variations in the reflectivity of the surfaces, it is important to evaluate the reflection coefficients for the different construction materials of the tube walls. Reflection coefficient can

be calculated by Fresnel reflection equations [79], [80]:

$$\Gamma(\theta) = \frac{1}{2} \left(\left| \frac{n_1 \cos \theta - n_2 \sqrt{1 - \left(\frac{n_1}{n_2} \sin \theta\right)^2}}{n_1 \cos \theta + n_2 \sqrt{1 - \left(\frac{n_1}{n_2} \sin \theta\right)^2}} \right|^2 + \left| \frac{n_1 \sqrt{1 - \left(\frac{n_1}{n_2} \sin \theta\right)^2} - n_2 \cos \theta}{n_1 \sqrt{1 - \left(\frac{n_1}{n_2} \sin \theta\right)^2} + n_2 \cos \theta} \right|^2 \right) \quad (3.6)$$

where θ is the incoming angle relative to the surface normal, and n_1 and n_2 are the indices of refraction of air/vacuum and material, respectively. For normal incidence ($\theta = 0$), the reflection coefficient Γ is simplified to:

$$\Gamma = \left| \frac{1 - n}{1 + n} \right|^2, \quad (3.7)$$

where $n_1 = 1$ (the refractive index of the air/vacuum) and $n_2 = n$ (the refractive index of the material).

In metals, the refractive index is a complex function of the frequency of the wave. The complex refractive index \bar{n} for an electromagnetic wave of angular frequency ω in a metal is

$$\bar{n} = n \sqrt{1 + i \frac{\sigma}{\varepsilon \omega}} \quad (3.8)$$

where ε is the permittivity (dielectric constant) and σ is the conductivity of the material. The real part of the refractive index n is given by [89]:

$$n = \sqrt{\varepsilon_r \mu_r}, \quad (3.9)$$

where ε_r is the relative permittivity and μ_r is the relative permeability [90].

For good conductors like metals, the complex refractive index has a very large imaginary part related to the conductivity and a comparatively insignificant real part. Then, we can approximate the complex refractive index in (3.8) as:

$$\bar{n} \approx n \sqrt{i \frac{\sigma}{\varepsilon \omega}} \quad (3.10)$$

The reflection coefficient of metal for normal incidence can then be written as:

$$\Gamma = \left| \frac{1 - \bar{n}}{1 + \bar{n}} \right|^2. \quad (3.11)$$

Substituting \bar{n} in Γ gives:

$$\Gamma = 1 - 2\frac{1}{\bar{n}}\sqrt{\frac{2\varepsilon\omega}{\sigma}} = 1 - 2\sqrt{\frac{2\varepsilon\varepsilon_0\omega}{\sigma\varepsilon\mu_r}} = 1 - 2\sqrt{\frac{2\varepsilon_0\omega}{\sigma\mu_r}} \quad (3.12)$$

which is the Hagen–Rubens relationship. This equation relates the reflection coefficient to the conductivity of the metal and the frequency f [91]–[93]:

$$\Gamma_{\text{metal}} = 1 - 2\sqrt{\frac{2\varepsilon_0 2\pi f}{\sigma\mu_r}}, \quad (3.13)$$

where $\varepsilon_0 = 8.85e^{-12}$ F/m denotes the vacuum electric permittivity, and μ_r is the relative permeability. To evaluate the path loss with respect to the reflection coefficient of the walls, we considered two different materials: carbon steel and concrete. We calculate the reflection coefficient for each material. For carbon steel walls, with $\sigma = 6.99 \times 10^6$ and Relative Permeability $\mu_r = 5.9 \times 10^6$, the reflection coefficient using (3.13) is obtained as $\Gamma_{\text{carbon steel}} = 0.9987$. For concrete, with $\varepsilon_r = 5.31$ and $\mu_r = 1$, using (3.7), the reflection coefficient is computed as $\Gamma_{\text{concrete}} = 0.155$.

The simulations are conducted at a carrier frequency of 4 GHz. Figure 3.8 illustrates the path loss for each material. The results show that concrete walls result in higher path loss compared to metal walls, likely due to concrete having a higher attenuation factor, which absorbs more signal energy as it propagates through the environment. In other words, the path loss for metal walls is lower than that for concrete, due to metal's highly reflective property, which reflects more signal energy rather than absorbing it, thus maintaining a stronger signal strength over distance. Another aspect of the simulations is that the path loss curve for metal walls exhibits significant fluctuations compared to the concrete one, due to the multiple reflections caused by the high reflectivity of metal.

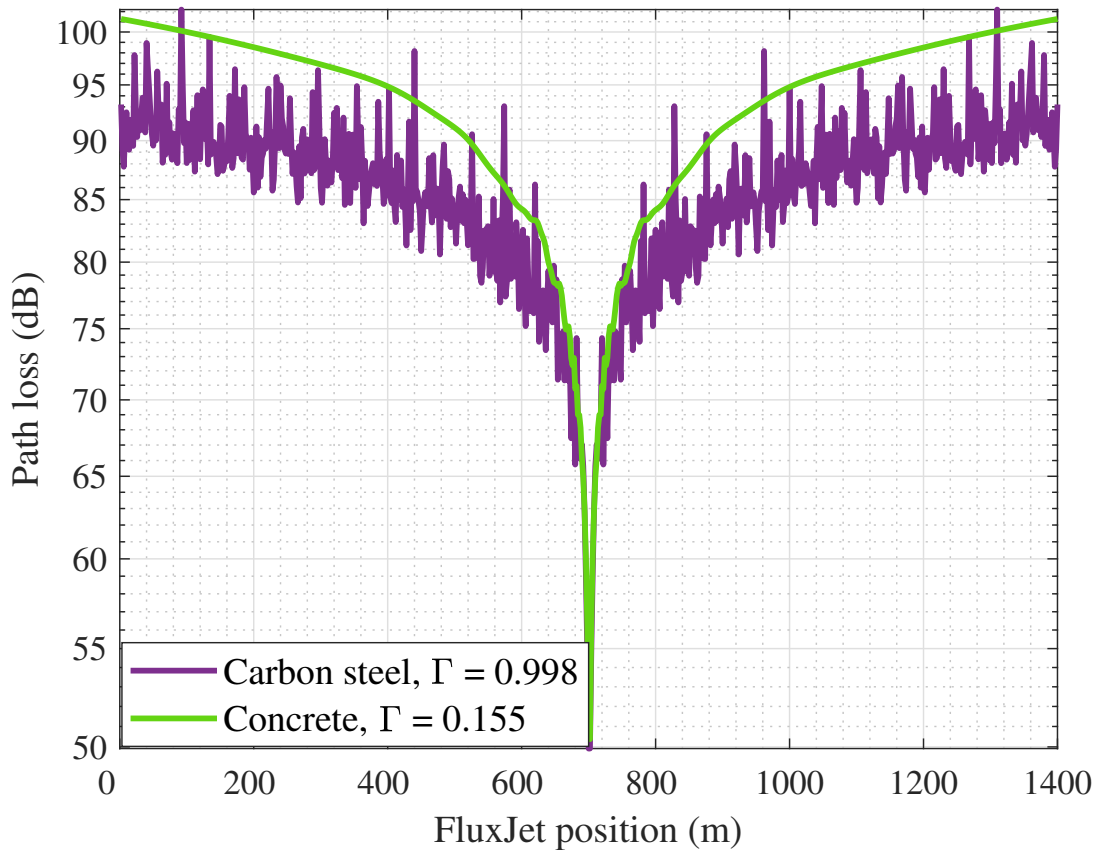


Figure 3.8: Path loss for different construction materials at 2.45 GHz.

- **Antenna gain:** Signal attenuation can be significantly influenced by the radiation pattern of both the transmitting and receiving antennas. In the previous sections, we considered isotropic antennas, which radiate uniformly in all directions. An isotropic antenna is a theoretical reference antenna with a gain of 1 (or 0 dB). However, real antennas are directional, meaning that they radiate more power in certain directions than others. This directional behavior is quantified by the antenna gain, which describes how much power is radiated in a particular direction compared to an isotropic antenna [30], [94].

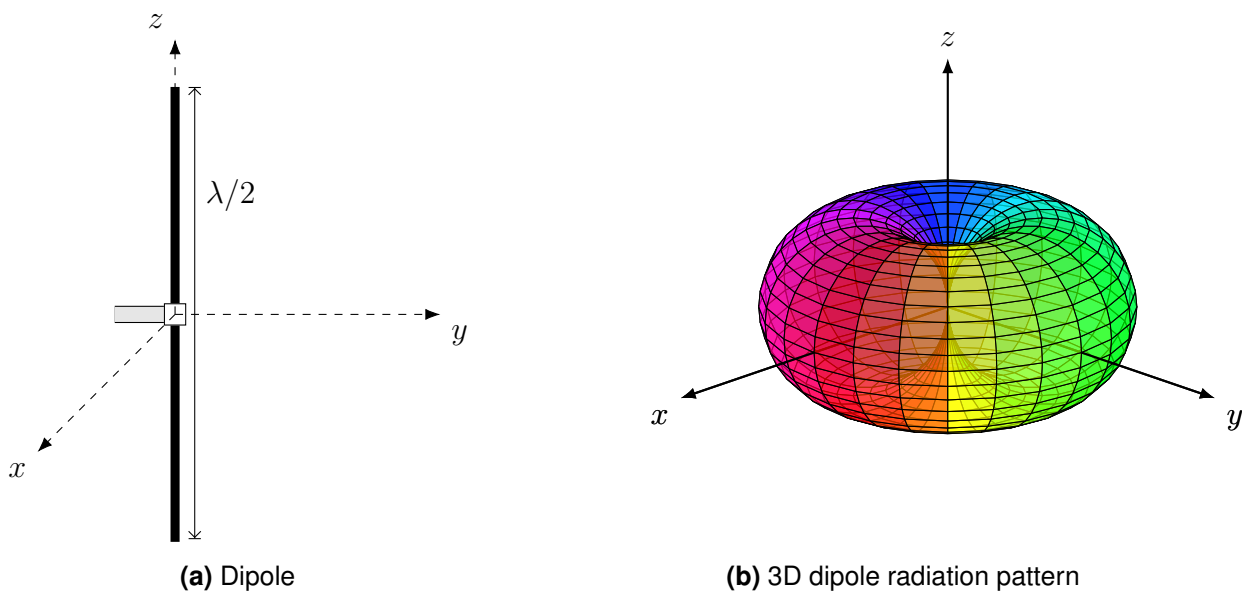


Figure 3.9: Half-wave dipole antenna and 3D pattern

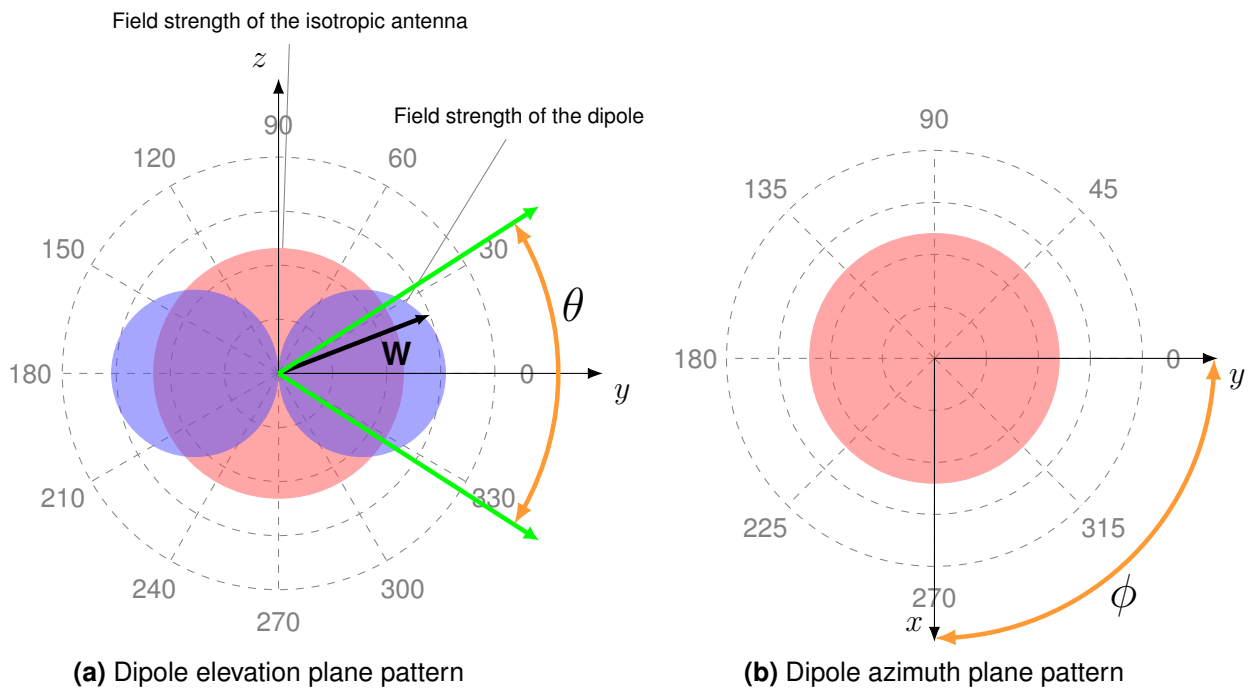


Figure 3.10: Half-wave dipole antenna patterns

A commonly used type of antenna is the dipole antenna. There are several types of dipole antennas such as horizontal dipole, half-wave dipole, and small dipole. In this discussion, we focus on the half-wave dipole, which has a length equal to half the wavelength of the frequency at which it operates. This dipole is

placed vertically, as shown in [Figure 3.9a](#). The antenna patterns are illustrated in [Figure 3.10](#). In [Figure 3.10a](#), we can observe the elevation plane pattern, which is the pattern seen in the yz plane or **E**-plane pattern and the electric field exists, showing the field strength as a function of θ , measured in yz -plane, between the z -axis and the radiation direction. In the azimuth plane or **H**-plane pattern, the magnetic field exists, and showing the field strength as a function of ϕ , measured in xy -plane from the x -axis, seen in [Figure 3.10b](#).

From the azimuth pattern, we find that the antenna works equally well in a full 360 degrees around the antenna. This indicates that the azimuth plane pattern is non-directional, meaning the antenna radiates its energy equally in all directions. So the azimuth plane pattern is a circle, passing through the peak gain at all angles. However, the radiation is directional in the **E**-plane, and this behavior can be described mathematically [30], [95].

The gain of an antenna in a specific direction is defined as the ratio of the intensity in that direction to the radiation intensity that would be obtained if the power accepted by the antenna were radiated isotropically. Mathematically, the gain $G(\theta)$ is given by [30], [95], [96]:

$$G(\theta) = \frac{4\pi r^2 U}{P_{rad}} \quad (3.14)$$

where U is the radiation intensity, which can be obtained by multiplying the radiation power density W by the square of the distance r :

$$U = r^2 W, \quad (3.15)$$

and P_{rad} is the total radiated power.

To calculate the power density, we need the electric and magnetic field values. The power density is given by the Poynting vector, which is the cross product of the electric field **E** and the magnetic field **H**:

$$W = \frac{1}{2} (E \times H^*) \quad (3.16)$$

For a half-wavelength dipole, the electric and magnetic field components are given

by:

$$\begin{aligned} E_{\theta} &\simeq j\eta \frac{I_0 e^{-jkr}}{2\pi r} \left[\frac{\cos\left(\frac{\pi}{2} \cos\theta\right)}{\sin\theta} \right] \\ H_{\phi} &\simeq j \frac{I_0 e^{-jkr}}{2\pi r} \left[\frac{\cos\left(\frac{\pi}{2} \cos\theta\right)}{\sin\theta} \right]. \end{aligned} \quad (3.17)$$

where:

- η is the intrinsic impedance of the medium,
- I_0 is the current at the feed point,
- k is the wave number,
- r is the distance from the antenna.

The power density is then:

$$W = \eta \frac{|I_0|^2}{8\pi^2 r^2} \left[\frac{\cos\left(\frac{\pi}{2} \cos\theta\right)}{\sin\theta} \right]^2 \simeq \eta \frac{|I_0|^2}{8\pi^2 r^2} \sin^3\theta \quad (3.18)$$

The total power radiated P_{rad} can be obtained by integrating the radiation intensity over a sphere of radius r :

$$P_{rad} = \int_0^{2\pi} \int_0^{\pi} U \sin\theta d\theta d\phi. \quad (3.19)$$

substituting (3.18) and (3.19) into the gain formula in (3.14), we get:

$$G(\theta) = 1.64 \left[\frac{\cos\left(\frac{\pi}{2} \cos\theta\right)}{\sin\theta} \right]^2 \simeq 1.64 \sin^3\theta. \quad (3.20)$$

The equation shows how the radiation pattern of the half-wavelength dipole is shaped based on the angle θ . Figure 3.11 presents simulation results comparing the performance of an isotropic antenna with unity gain $G_t = G_r = 1$ against that of a half-wave dipole antenna at both the transmitter and receiver, each with a maximum gain of 1.64. The carrier frequency utilized is 4 GHz, with a reflection coefficient of 0.998, corresponding to the material properties of the carbon steel tube. The findings indicate a reduction in path loss when employing the half-wave

dipole antenna compared to the isotropic antenna. The higher gain of the half-wave dipole means more energy is directed in a specific direction. This does not change the physical path loss but improves the effective received power by focusing the energy, thereby reducing the effective path loss.

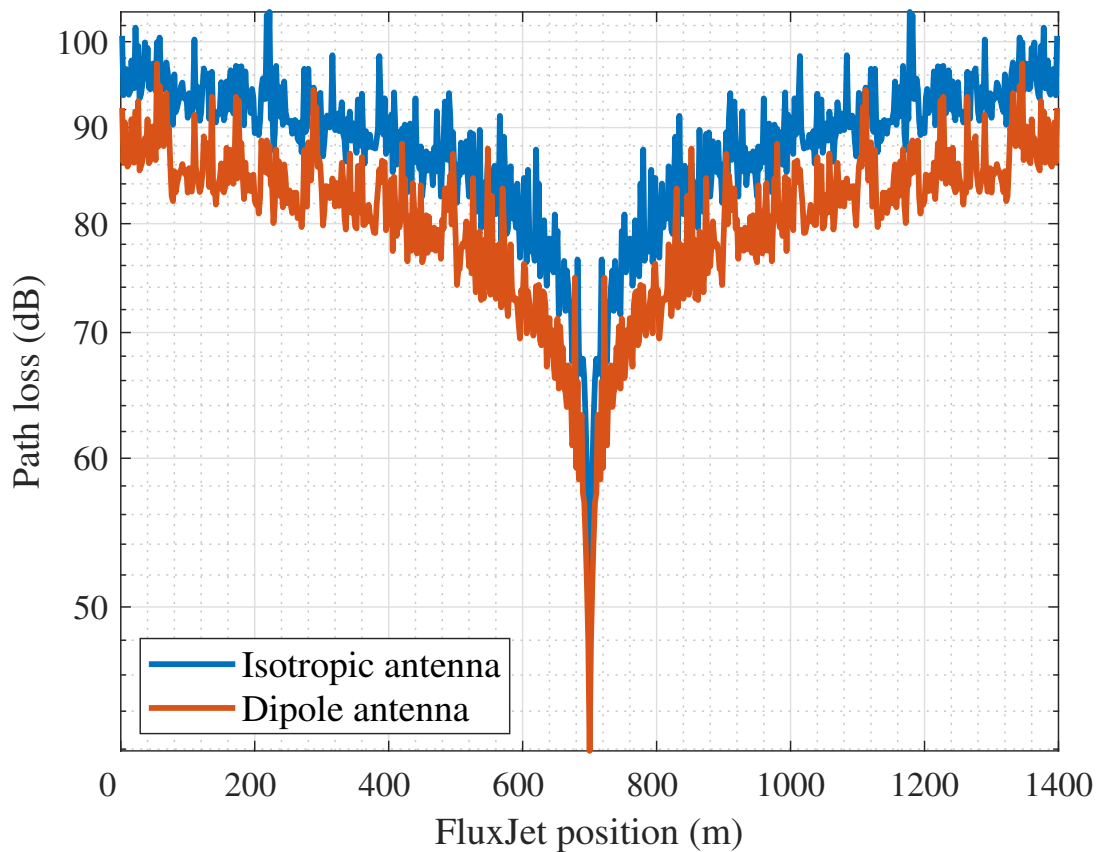


Figure 3.11: Path loss for isotropic and directive antenna.

In more details, at long distances between the transmitter and receiver within the tube, the angle of arrival of many reflected paths at the receiver tends to be very close, causing these paths to effectively contribute to a single resolvable path. When using a high-gain antenna, the focused energy is directed along the main lobe of the antenna radiation pattern, which aligns with the direct path in the tube, increasing the power density along the LOS path. This concentration of power results in a stronger signal, even if the number of multipath reflections remains similar.

At shorter distances, some reflected paths might fall outside the antenna effective range due to the steep angles of arrival, but the direct path remains highly efficient due to the increased gain. Therefore, the high-gain antenna performs better than an isotropic antenna, as it directs more power towards the receiver, results in higher signal strength and lower path loss.

3.4.2 Delay spread

The channel inside the tube presents dispersion in time due to the multipath effect. In this section, we analyze the delay spread characteristics of the channel. [Figure 3.12](#) shows the delay spread vs the transmitter-receiver distance. Initially, in very closed areas, LOS propagation is dominant. As the distance increases, the number of multipath changes frequently, leading to an increase in delay spread. When the number of paths remains constant, there is a decreasing trend in delay spread, until the addition of further multipath component. This pattern persists until approximately 100 meters.

However, beyond this point, for longer distances, there are no new paths added, and there is a decreasing trend in the curve. This is because many of the reflected paths arrive from directions that are close to each other, making the differences in their arrival times smaller. Consequently, the delay spread decreases. The addition of new paths does not significantly augment the delay spread, resulting in a continued decrease in the curve. Most signals experience very close delay times, and increasing the number of paths has minimal impact since they mostly fall within one resolvable path. This phenomenon can be explained due to the confined diameter of the tube and the minimal gap between the vehicle and the tube. In the [Figure 3.12](#), the points with the same color represent the paths within one resolvable path.

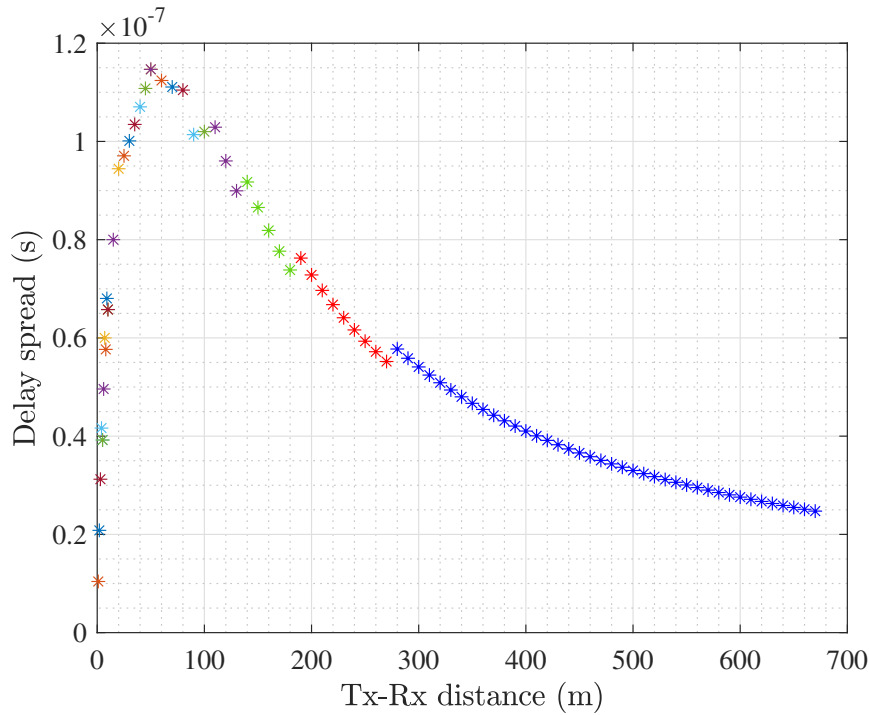


Figure 3.12: Delay spread for different Tx-Rx distances.

3.4.3 Doppler spread

In this section, we analyze the Doppler effect caused by the movement of the FluxJet inside the tube. The Doppler effect is characterized by the Doppler spread, which measures the dispersion of the channel in frequency. The instantaneous Doppler shift ν depends on the wavelength λ , the relative speed v of the FluxJet with respect to the tube, and the angle of arrival θ . It is expressed as:

$$\nu = \frac{v\phi}{\lambda}. \quad (3.21)$$

Figure 3.13 demonstrates the Doppler shift characteristics for both LOS and NLOS components as the distance between the transmitter and receiver increases. As shown in Figure 3.13, the movement of the FluxJet causes the receiver to move away from the transmitter. At shorter distances, the angle of arrival of multipath reflections results in varying Doppler shifts for different paths. This is indicated by the different colors on the curve, representing different Doppler shift values or intensities. Conversely, at longer distances, despite the presence of more multipath components, the tube's geometry

causes reflected waves to reach the receiver at nearly identical angles. This results in minimal variation in Doppler shift values, represented on the curve as a homogeneous area with uniform intensity and color.

Figure 3.14 illustrates the Doppler characteristics observed at various positions of the FluxJet as it quickly approaches the transmitter and passes by it. The Doppler spectrum exhibits a centrally symmetric shape, with the point of symmetry located at the midpoint. The primary variation in the spectrum resembles a Z shape, featuring a turning angle close to 90° . Additionally, the Doppler spectrum exhibits a sharp transition from its maximum to minimum value as the train passes the transmitter. This phenomenon is due to the short distance between the FluxJet and the tube.

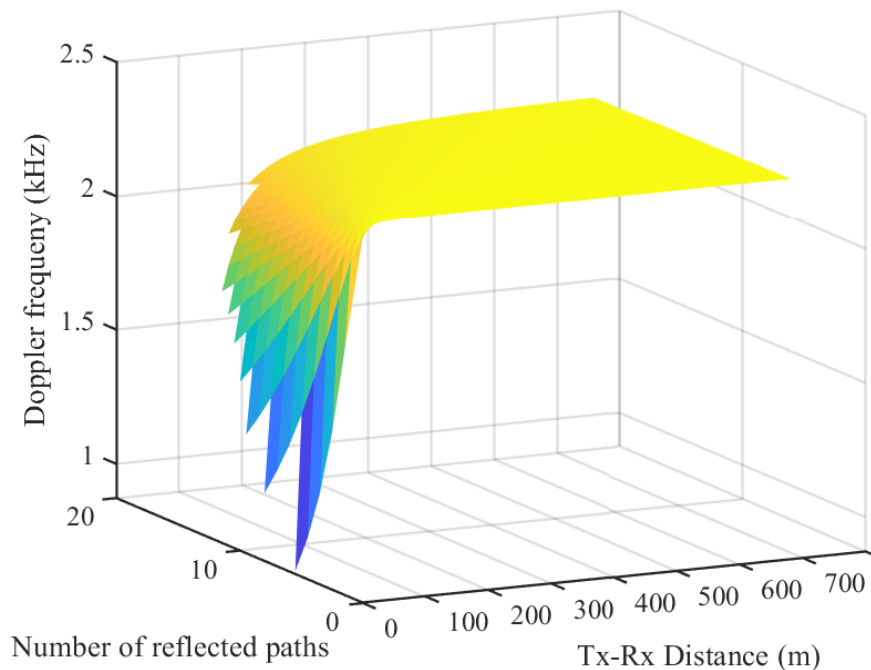


Figure 3.13: Doppler spectrum for different Tx-Rx distances.

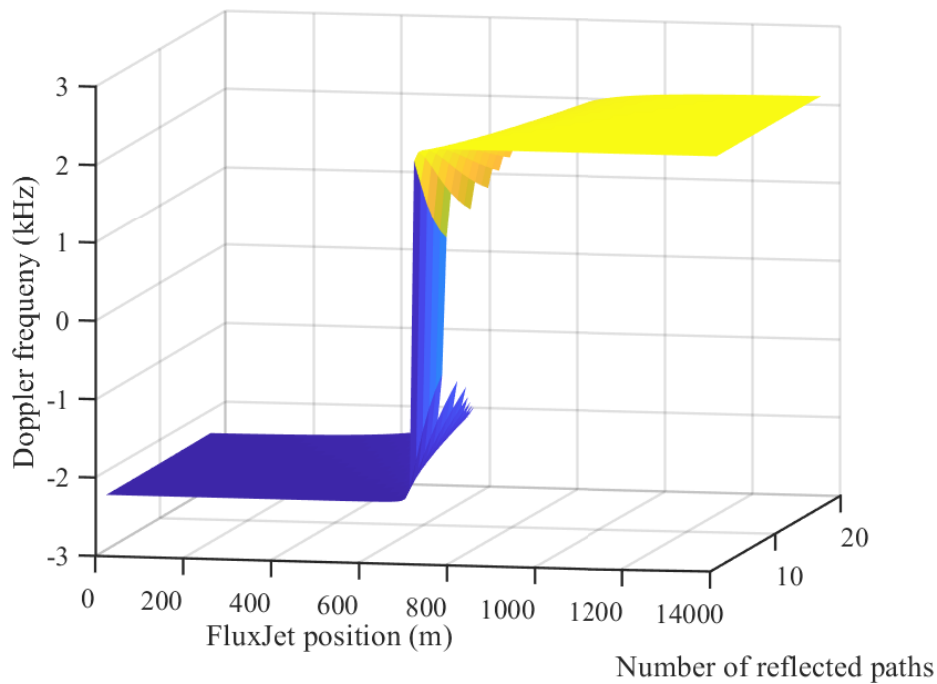


Figure 3.14: Doppler spectrum for different Tx-Rx distances.

3.4.4 Power-delay-Doppler profile

According to the previous position-based results, the propagation characteristics of the TransPod channel vary depending on the distance between the transmitter and the receiver, D_s . When the distance is large, the dominant propagation resolvable component is the LOS path, and the number of resolvable paths is minimal. Due to the small diameter of the tube compared to the distance, the multipath components experience similar Doppler shifts, as they reach the receiver at approximately the same angle. On the contrary, as the distance decreases, the propagation characteristics change. In addition to the LOS path, multiple reflections and multipath components become more significant. Each reflection introduces a unique angle of arrival at the receiver, leading to different Doppler shifts for each multipath component. To qualitatively visualize the channel at each transmitter-receiver distance, we create scatter plots, where the color intensity at each point represents the power of the path received at the receiver. These scatter plots effectively illustrate the distribution of delay and Doppler as the vehicle moves inside the tube, with varying transmitter-receiver distances. The scatter plots in [Figure 3.15](#) shows the power-delay-Doppler profiles for three distances

between the transmitter and receiver 10m, 80m, and 700m, respectively. For shorter distances, as depicted in Figure 3.15a, the diversity in angles of arrival results in a broader dispersion of Doppler and delay effects. This diversity introduces more complex channel conditions, where the power of the received signals is spread across multiple paths. Each of these paths is characterized by different delays and Doppler shifts, alongside varying time and frequency properties. Conversely, at longer distances, such as in the scenario depicted in Figure 3.15c, the plot demonstrates a channel with a short delay spread, where paths exhibit nearly identical Doppler shifts. This is due to the geometry and reflective characteristics of the tube, which result in a relatively constant angle of arrival for NLOS paths, thus minimizing the variability in Doppler shifts. At a moderate distance of 80 meters, as illustrated in Figure 3.15b, the LOS component continues to be a major factor, but the effects of multipath reflections are becoming more evident.

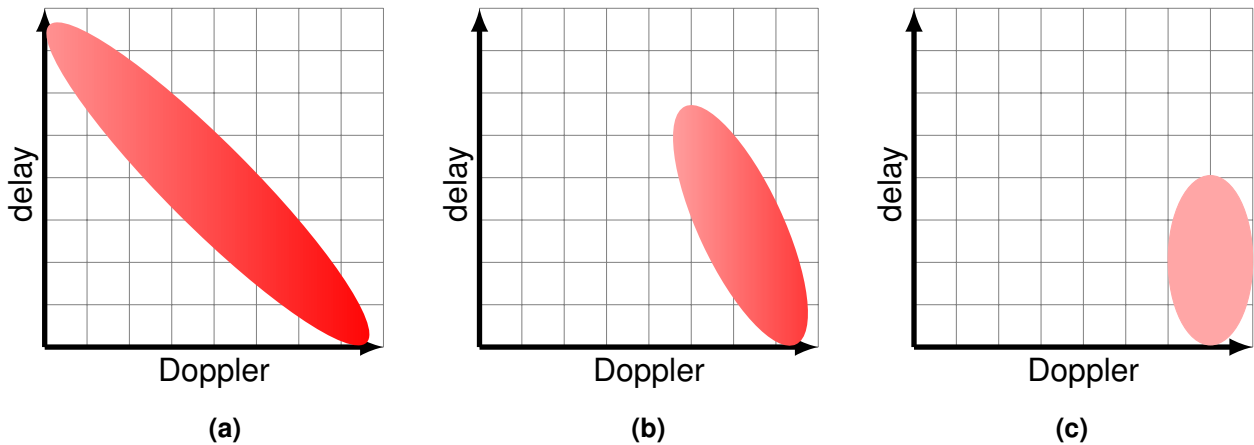


Figure 3.15: Power-Delay-Doppler profiles for different transmitter-receiver distances: (a) 10m, (b) 80m, (c) 700m

3.4.5 Time-Frequency Transfer Function

We rewrite the time-varying transfer function in (3.1) as:

$$H(t, f) = \sum_{i=0}^P h_i e^{\frac{2j\pi f c v \phi_i t}{c}} e^{-\frac{2j\pi D_i f}{c}}. \quad (3.22)$$

This expression represents the channel's complex attenuation factors h_i at time t and frequency f . Figure 3.16 illustrates the time-frequency transfer function of the system

as the FluxJet moves towards the transmitter at a constant speed of 1000 km/h. The function shows fluctuations in both time and frequency, reflecting the time dispersion that corresponds to frequency selectivity and the frequency dispersion that corresponds to time selectivity.

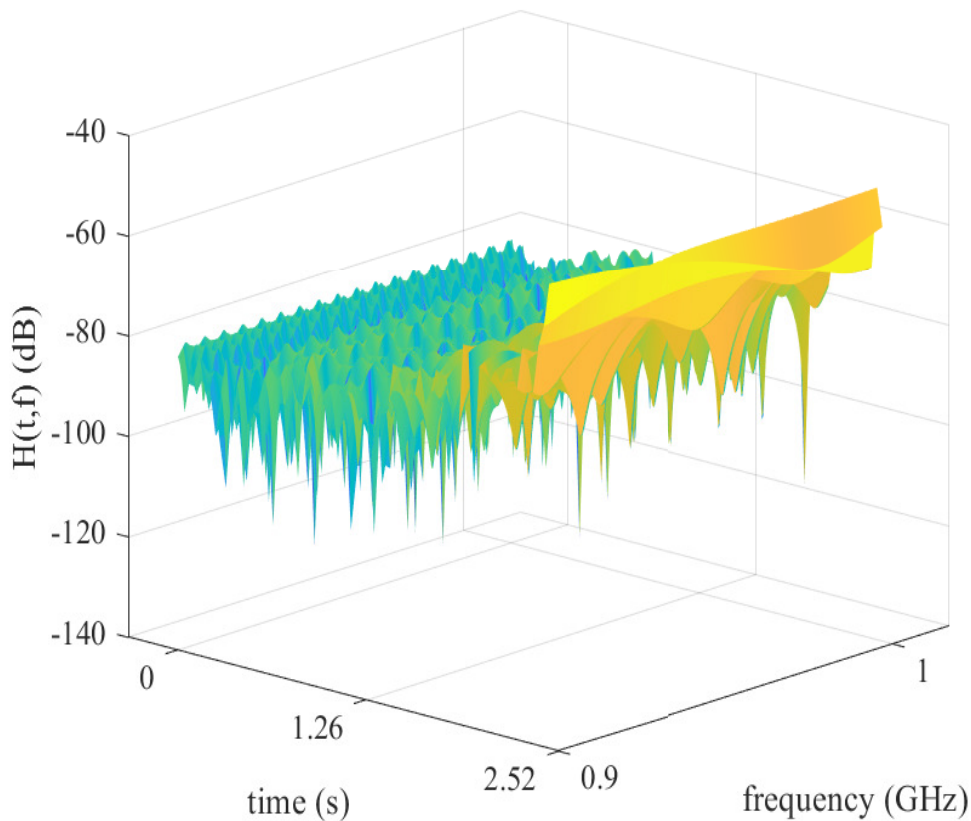


Figure 3.16: Time-frequency transfer function $H(t, f)$

3.5 Plasma-based Power Transmission System

In section 3.3, we introduced the FluxJet main technologies including levitation, propulsion, and plasma-based power transmission system. The power transmission system consists of two track electrodes, mounted to the inner surface of the low-pressure tube, and two vehicle electrodes attached to the vehicle structure through actuators. Actuators are designed to maintain the relative position between tube electrodes and the vehicle electrodes as the vehicle moves through the tube. To electrically connect the vehicle and

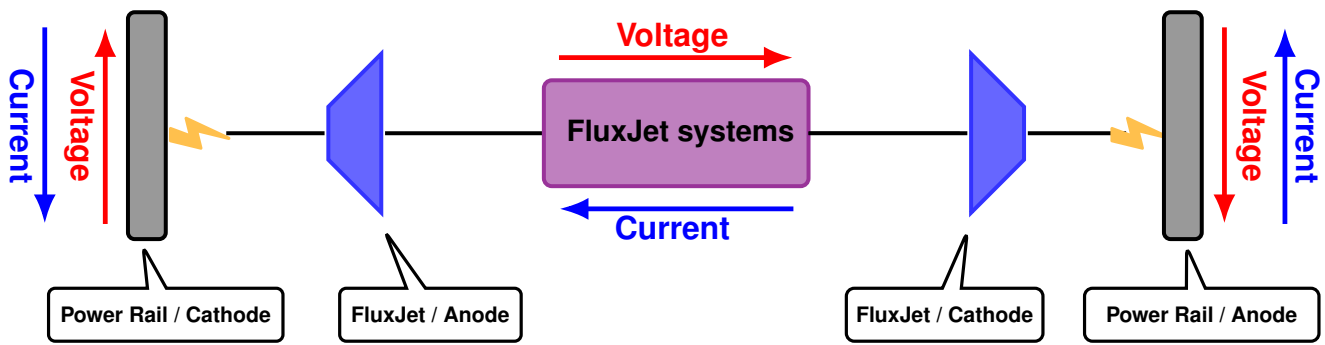


Figure 3.17: FluxJet power transmission schematic.

the infrastructure, a plasma state of matter is initiated and maintained between vehicle and tube electrodes [7]. The system could function in AC or DC modes. Regardless of the mode in question, a free-burning plasma arc is formed between electrodes and powering all the internal systems. The FluxJet power transmission schematic is illustrated in Figure 3.17. We set up some experiments to verify the high-speed operation of a plasma-based power transmission. These measurements replicated the conditions of (a) high altitude, low-pressure environment, (b) high-velocity motion, and (c) high electric field. The experiments were performed using a vacuum chamber and pressure control system, along with a custom-built high-voltage power system which was designed with a multiplexer circuit to control and maintain plasma. The high-voltage power and monitoring signals were delivered into the vacuum environment using an epoxy-sealed penetration [7]. A robotic arm was installed to remotely manipulate an electrode, which carried plasma through to a motorized rotating disc, controlled by a 3-phase inverter and electronic speed controller [7]. High-voltage signals were measured and recorded and we use a sample of these measured signals.

3.6 Impulsive Noise

The plasma arc discharge from the power transmission system of TransPod, could become a source of electromagnetic noise. By analyzing the measured data, we observe that the instantaneous noise variance is correlated with the current, which is drawn in the plasma arc discharge. It means that a signal at the receiver can be contaminated by a kind of impulsive noise. Impulsive noise is characterized by the probabilities of short duration and high amplitude pulses that is much greater than usual

peaks of data. Since the power transmission system and communication system will exist in the same environment inside a metal guideway isolated from the outside world, it is important to make the communication system resilient to this interference, seen in Figure 3.18. Impulsive noise has a significant impact in many communication settings, as recent literature points out: power-line communications [97], digital subscriber loop [98], wireless networks and OFDM [99], wireless sensor networks [100], acoustic communication [101], and different vehicular communications scenarios [102].



Figure 3.18: Schematic of the TransPod system with the plasma-based power transmission system and transmitter/receiver inside the steel tube.

Impulsive noise lowers the quality of received signals across a broad frequency range during short periods. This type of noise appears as a sequence of pulses, each occurring at random intervals and lasting for random duration. These noisy bursts can seriously corrupt the received signal. In this work, we aim to develop a mathematical model for this impulsive noise originating from plasma sources. Commonly used models for impulsive noise without memory include the Middleton Class A [103] and Bernoulli Gaussian [104]. Models that incorporate memory, such as the Markov Middleton [105] and Markov-Gaussian [106], are also considered. Since we're focusing on plasma as the primary source of impulsive noise, we employ a two-state Markov-Gaussian model in our analysis [107]. A detailed description of this model is presented in the next section.

3.6.1 Two-state Markov-Gaussian Model

The two-state Markov-Gaussian model was introduced by Fertoni [106]. In this model, we define a set of real-valued noise samples $\{X_k, k = 1, 2, 3, \dots, K\}$ [108], [109]. The statistical properties of the noise samples are completely described by states $s_k \in G, B$. In state G, there's no impulsive noise, and the transmitted signal is only affected by

background Gaussian noise. State B indicates impulsive noise presence, additionally affecting the transmitted signal. Given s_k , the Probability Density Function (PDF) of X_k are Gaussian distributions [110]:

$$\begin{aligned} p(X_k | s_k = G) &= \frac{1}{\sqrt{2\pi\sigma_G^2}} \exp\left(-\frac{X_k^2}{2\sigma_G^2}\right) \\ p(X_k | s_k = B) &= \frac{1}{\sqrt{2\pi\sigma_B^2}} \exp\left(-\frac{X_k^2}{2\sigma_B^2}\right), \end{aligned} \quad (3.23)$$

where σ_G^2 represents the average noise power of the "good channel", and σ_B^2 represents the average noise power of the "bad channel". The noise is characterized by the state process $s^K = \{s_0, s_1, \dots, s_{K-1}\}$, a stationary first-order Markov process:

$$p(s^{K+1}) = p(s_0) \prod_{k=0}^K p(s_{k+1} | s_k). \quad (3.24)$$

The state process is described by state transition probabilities $p_{s_k s_{k+1}} = p(s_{k+1} | s_k)$. Stationary probabilities of being in states G and B, i.e., p_G and p_B , are respectively obtained as [110]:

$$\begin{aligned} p_G &= p(s_k = G) = \frac{p_{BG}}{p_{GB} + p_{BG}} \\ p_B &= p(s_k = B) = \frac{p_{GB}}{p_{GB} + p_{BG}}, \end{aligned} \quad (3.25)$$

where p_{BG} denotes the transition probability from state B to state G, and p_{GB} is the transition probability from G to B. Hence, we can fully describe the noise using transition probabilities p_{GB} and p_{BG} . A two-state Markov process can be illustrated by a Markov chain with two states, as shown in Figure 3.19 [111], [112].

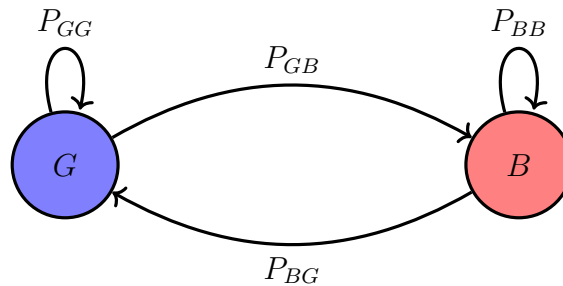


Figure 3.19: Markov chain representation with two states G and B and transition probabilities.

3.6.2 Noise Measurements

The electrical current recorded from the plasma arc discharge are categorized according to the spacing between the vehicle electrodes and tube electrodes, as illustrated in [Figure 3.20](#). Our objective is to first analyze this recorded data and secondly develop a model for the impulsive noise. Statistical parameters such as mean and variance metrics are employed for this purpose, as they effectively characterize the noisy the noise statistics [22].

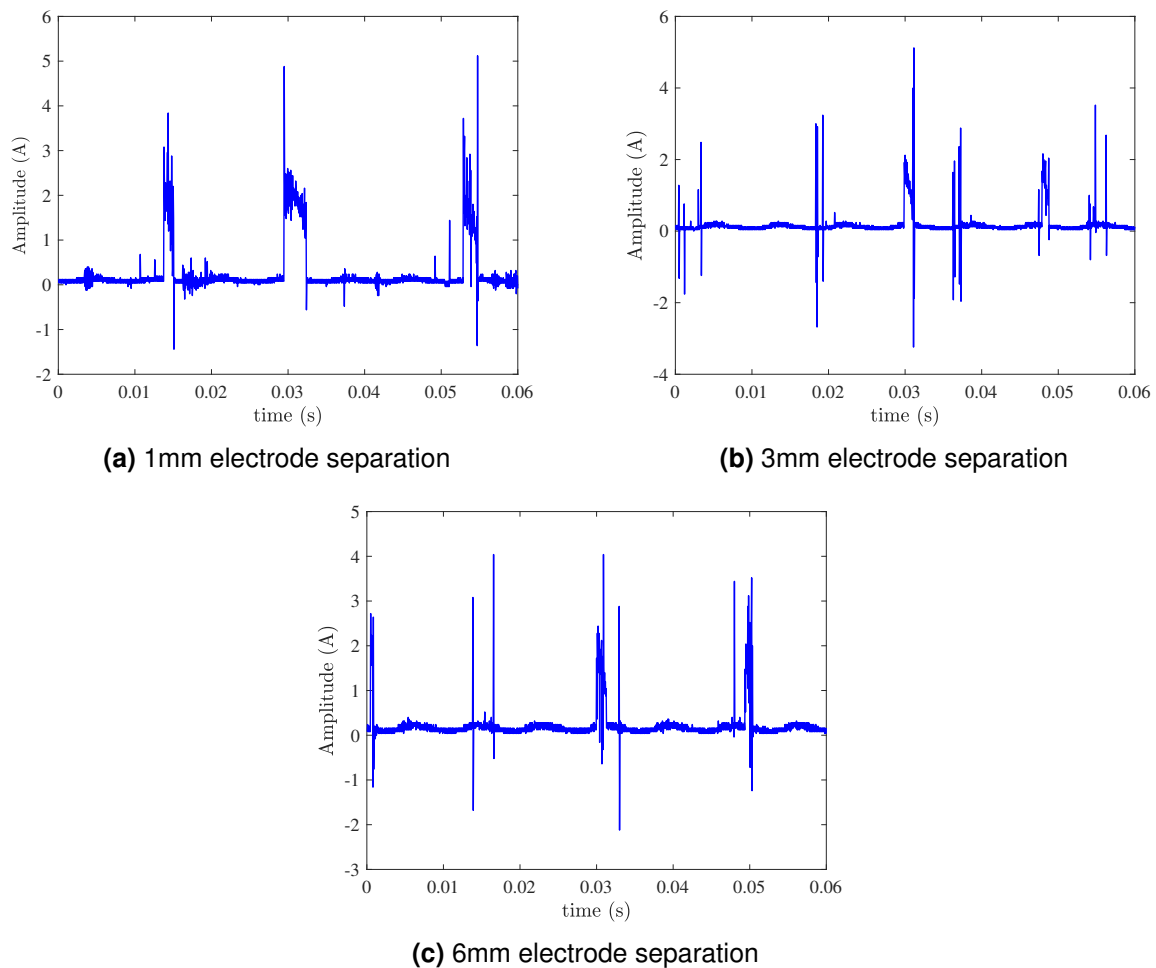


Figure 3.20: Plasma arc current during a system transient at various electrode separations.

3.6.3 Data Analysis

To evaluate the measured data, we model the impulsive noise as a series of pulses, where the intervals between successive pulses and the duration of each pulse are

treated as stochastic variables. We introduce two key variables, termed as *Pulse Distance*, P_D , which measures the gap between consecutive pulses, and *Pulse Width*, P_W , which measures the length of each pulse.

The initial step in interpreting the noisy signal involves the detection of impulsive events and determining their time boundaries within the signal. This is done by comparing a moving average of the signal amplitude with a predefined threshold [109]. A pulse is identified when the amplitude of the moving average surpasses this threshold, and it concludes when the amplitude drops back below it. After constructing the sequence of pulses from the recorded signal, we calculate the statistical measures μ_{P_D} and $\sigma_{P_D}^2$ for the intervals between pulses, and μ_{P_W} and $\sigma_{P_W}^2$ for the duration of the pulses, representing their mean and variance respectively. The recorded data are presented in this section. The y coordinate of the plots are normalized between 0 and 1. For three different distances of 1mm, 3mm, and 6mm between the electrodes, the measured current signals corresponding to the plasma arc discharge are plotted in [Figure 3.21](#), [Figure 3.22](#), and [Figure 3.23](#), respectively. The blue line in the figures represents the measured arc current during a system transient, and the red line shows the state of the detected impulsive.

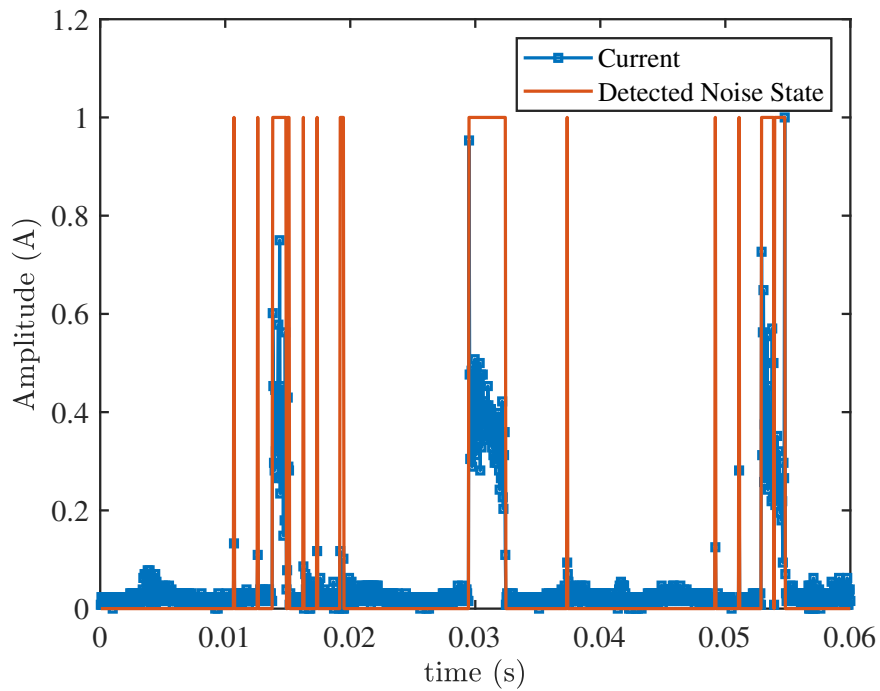


Figure 3.21: Plasma arc current during a system transient, at an electrode separation of 1 mm, overlaid with the model's generated square wave pulses.

[Figure 3.22](#) and [Figure 3.23](#) illustrate the same results for the electrodes distance equal to 3 mm and 6 mm, respectively. Once the statistical analysis of the pulse width and pulse distance is completed, the next step involves fitting these characteristics into a Markov chain model.

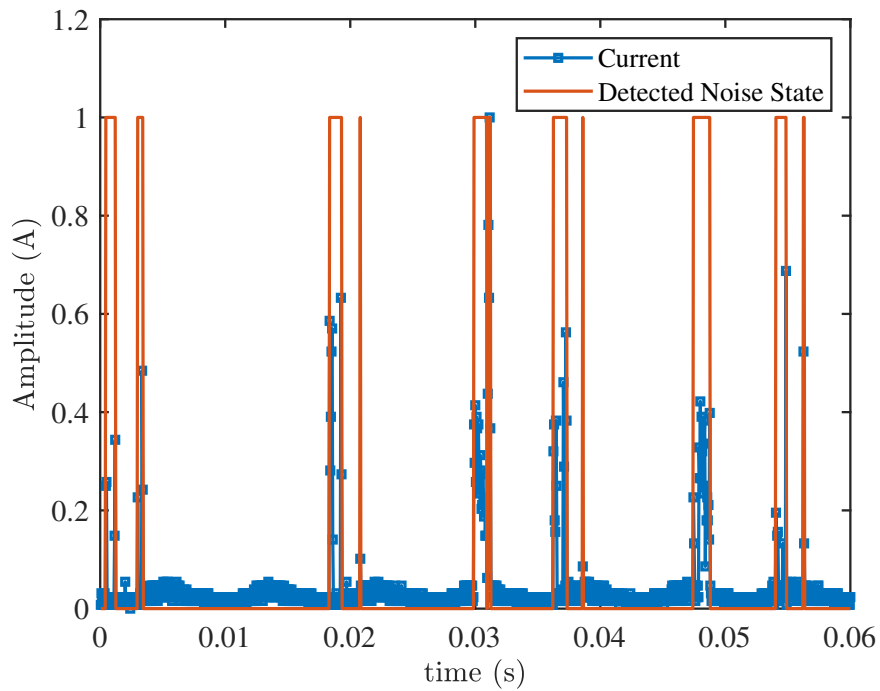


Figure 3.22: Plasma arc current during a system transient, at an electrode separation of 3mm, overlaid with the model's generated square wave pulses.

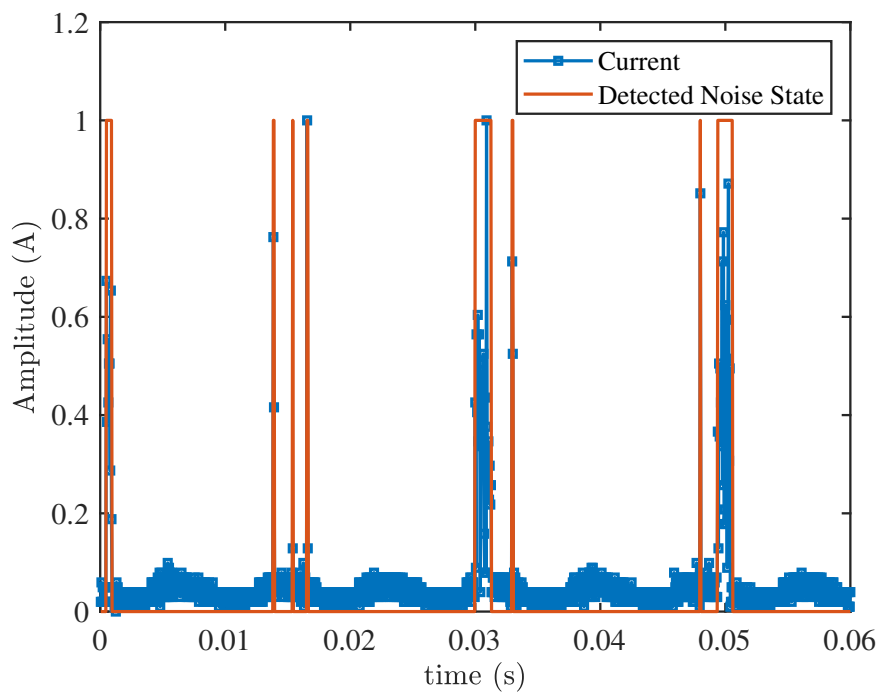


Figure 3.23: Plasma arc current during a system transient, at an electrode separation of 6mm, overlaid with the model's generated square wave pulses.

3.6.4 Markov Chain Model

As discussed in [subsection 3.6.1](#), the noise can be fully understood using the Markov model, once we acquire the transition probabilities p_{GB} and p_{BG} . To achieve this, we must determine both the initial probabilities of the states and the conditional transition probabilities, which are outlined in matrix P , as described in [113]:

$$P = \begin{bmatrix} p_{GG} & p_{GB} \\ p_{BG} & p_{BB} \end{bmatrix}. \quad (3.26)$$

The pulse distance (P_D) and pulse width (P_W) generated by the model are denoted as (\tilde{P}_D) and (\tilde{P}_W) respectively. Using the provided probabilities, we generate a sequence of N noise samples. Subsequently, we calculate the statistical mean $\tilde{\mu}_{P_D}$ and variance $\tilde{\sigma}_{P_D}^2$ (as well as $\tilde{\mu}_{P_W}$ and $\tilde{\sigma}_{P_W}^2$) of the random variables \tilde{P}_D (and \tilde{P}_W) of the noise series generated by the Markov chain model.

To adjust the created model with the measurements, we compare the mean and variance of the pulse distance and pulse width obtained from the measured data with those from the generated Markov model. We establish a suitable metric to align our model with the measured data, aiming to minimize four cost functions outlined in (3.27)-(3.30), where the difference between the measured mean values and those generated by the model is minimized. Additionally, we aim to minimize the variance error between the measured and modeled data.

$$J1_{P_D} = \min \|\tilde{\mu}_{P_D} - \mu_{P_D}\|^2, \quad (3.27)$$

$$J2_{P_D} = \min \|\tilde{\sigma}_{P_D}^2 - \sigma_{P_D}^2\|^2, \quad (3.28)$$

$$J1_{P_W} = \min \|\tilde{\mu}_{P_W} - \mu_{P_W}\|^2, \quad (3.29)$$

$$J2_{P_W} = \min \|\tilde{\sigma}_{P_W}^2 - \sigma_{P_W}^2\|^2. \quad (3.30)$$

This process is known as multi-objective minimization. To address this problem, we can minimize a single cost function, which is the sum of four metrics (3.27)-(3.30). The cost function is defined as follows:

$$J = J1_{P_D} + J1_{P_W} + J2_{P_D} + J2_{P_W}. \quad (3.31)$$

We apply a coarse-to-fine search method to minimize the cost function. Initially, we create a grid with coordinate axes p_{GB} and p_{BG} , each ranging from 0 to 1 with a step size of 0.1. We begin with a coarse grid resolution and iterate over all pairs of (p_{GB}, p_{BG}) on this grid, computing the cost function (3.31). We then identify the pair (p_{GB}, p_{BG}) that minimizes the cost function. Subsequently, we refine the search by adjusting the range of the axes around this obtained pair, transitioning to a finer grid resolution. This process continues until the accuracy of the grid points on the axes reaches within 0.0001. The iterative minimization process is summarized in Algorithm 1.

Algorithm 1 Minimizing Algorithm

Input: $\mu_{P_D}, \sigma_{P_D}^2, \mu_{P_W}, \sigma_{P_W}^2$.

Output: p_{GB}, p_{BG} .

- 1: We initialize the p_{GB} and p_{BG} in the range [0, 1].
 - 2: Compute step size $\Delta_{p_{GB}} = \frac{p_{GB}[\text{end}] - p_{GB}[\text{start}]}{10}$ and $\Delta_{p_{BG}} = \frac{p_{BG}[\text{end}] - p_{BG}[\text{start}]}{10}$.
 - 3: Create a grid with coordinate axes p_{GB} and p_{BG} with computed step size.
 - 4: Compute the cost function (3.31) for each grid point.
 - 5: Find the value $\hat{p}_{GB}, \hat{p}_{BG}$ which minimizes the cost function in (3.31).
 - 6: Set the coordinates in the new ranges
 $p_{GB} = \hat{p}_{GB} - \Delta_{p_{GB}}, \dots, \hat{p}_{GB} + \Delta_{p_{GB}}$ and
 $p_{BG} = \hat{p}_{BG} - \Delta_{p_{BG}}, \dots, \hat{p}_{BG} + \Delta_{p_{BG}}$.
 - 7: Stop if $(\hat{p}_{GB}$ and $\hat{p}_{BG})$ have the accuracy within 0.0001 or go to step 2 to refine grid over \hat{p}_{GB} and \hat{p}_{BG} .
-

3.6.5 Numerical Results

To create a comprehensive noise model that generalizes across different electrode spacing, the mean values of the pulse width and pulse distance are averaged across the three datasets (1mm, 3mm, and 6mm). Similarly, the variances of these two variables

are also averaged.

Table 3.1 represents the mean and variance values of P_D and P_W for three different electrode distances. It also includes the mean and variance values extracted from the Markov model of the noise. These values correspond to the minimum values of the cost function given in **Equation 3.31**. The table includes generalized averaged values as well as the statistical parameters derived from the Markov model.

Table 3.1: Comparison between the statistical parameters from the measured data and the model (E.D stands for the distance between electrodes).

| Parameters | $\mu(P_D)$ | $\sigma^2(P_D)$ | $\mu(P_W)$ | $\sigma^2(P_W)$ |
|-------------------------|------------|-----------------|------------|-----------------|
| Measured | 0.0036 | 1.5717e-5 | 5.1538e-4 | 6.9266e-7 |
| Model | 0.0036 | 2.2108e-5 | 4.1632e-4 | 5.9847e-7 |
| (E.D = 1mm) | | | | |
| Measured | 0.0056 | 2.0066e-5 | 6.409e-4 | 2.2591e-7 |
| Model | 0.0056 | 3.1069e-05 | 6.3089e-4 | 3.1102e-7 |
| (E.D = 3mm) | | | | |
| Measured | 0.007 | 4.3069e-5 | 4.1875e-4 | 2.8067e-7 |
| Model | 0.007 | 5.0821e-5 | 3.9102e-4 | 2.9932e-7 |
| (E.D = 6mm) | | | | |
| Generalized data | 0.0054 | 2.6284e-5 | 5.2501e-4 | 4.6641e-7 |
| Model | 0.0054 | 2.015e-5 | 5.2016e-4 | 2.2530e-7 |

Using the generalized Markov chain model, noise samples can be generated based on averaged means and variances. By generating these noise samples, we gain general insights into the nature of the impulsive noise affecting the system, including its frequency and duration. This simulation is crucial for the next step of the work, which involves designing coding techniques to mitigate the effects of this noise. **Figure 3.24** illustrates the noise samples produced by the generalized model.

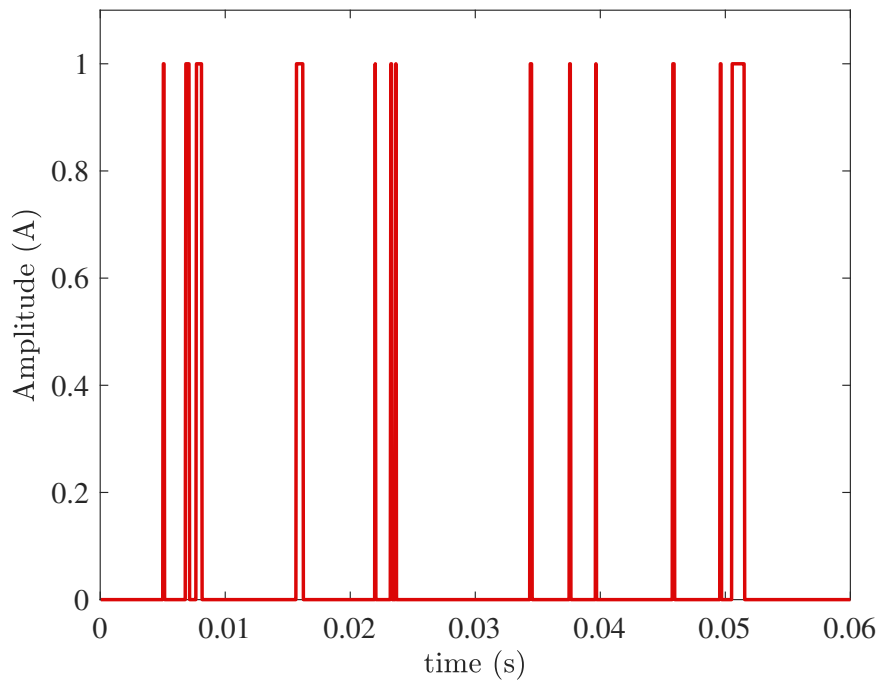


Figure 3.24: Noise samples modeled by Two-state Markov model.

3.7 Coding Techniques to Mitigate the Impulsive Noise

The findings in the previous section show that plasma-based power transmission system of TransPod constitute the noisy transmission medium with impulsive noise, which can seriously degrades the transmission performance. Given the nature of impulsive noise, the following coding approaches can be considered:

1. **Erasure Code:** Impulsive noise can cause parts of the transmitted signal to be corrupted so badly as to be considered erased. When a receiver encounters an impulsive noise, the signal during the noise period can be so degraded that the information is irretrievable. In such cases, the communication system can treat these corrupted portions as erasures. The erasures can be clustered together which refers to the burst erasure error. The erasure codes can then be used to recover the missing data. In some cases, the system uses detection mechanisms to identify the corrupted portions and marked them as erased, then uses erasure codes to recover the lost information.

Fountain codes are a class of erasure codes and an efficient way to protect data against erasures. The idea behind is that to transmit a fixed set of source packets over an erasure channel, the source packets are encoded by combining packet data into a possibly infinite sequence of encoded packets, and the receiver decodes the encoded packets again into source packets. Luby Transform (LT) codes [114] are a practical example of digital fountain codes. An extension of LT codes, Raptor codes were introduced in [115]. In Raptor codes, each encoded packet is a linear combination (XOR) of the transmitted packets. In [116], the utilization of concatenated LT and Low Density Parity Check (LDPC) codes has been proposed. LDPC codes were employed as the inner code to identify which packets are marked as erased, while LT codes were used as the outer code for correcting errors. [117], proposed a joint erasure marking and Viterbi algorithm within the same decoding block to decode the convolutionally coded data transmitted over an unknown impulsive noise channel.

2. **Error Correction Code (ECC):** The transmitted data may be corrupted due to the impulsive noise, but not completely erased. These errors can occur in a contiguous sequence of symbols, refer to the burst error. In such case, interleaving can be applied to rearrange the data bits or symbols in a way that disperses the burst errors over different blocks or frames. The data spreads across multiple blocks and converting the consecutive errors into some scattered errors. Interleavers can be bit interleavers [118], [119] or symbol interleavers [120]–[122]. Interleaving is usually utilized in combination with ECC designed to correct random errors like Reed–Solomon (RS) codes [123], Polar codes, LDPC codes. Therefore, the detected random errors can be corrected by applying ECCs. In [124], a combination of interleaving and RS coding was proposed to shield systems from noise bursts. The authors in [125] investigate the performance of polar codes over impulsive noise in Programmable Logic Controller (PLC) in OFDM systems and demonstrate that Polar codes outperformed LDPC codes in the presence of Middleton’s Class A noise.

According to the noise samples created from the Markov model and the statistical parameters, we can evaluate the frequency and duration of impulsive noise occurrences.

This evaluation helps in determining the appropriate coding techniques to apply. For example, with a radio frame size of 10 ms in LTE and according to the noise samples from the model shown in Figure 3.24, it appears that a significant portion of the packet can be corrupted. In such cases, applying erasure coding techniques is practical. If the whole or a large portion of a data packet is corrupted, applying erasure coding techniques is practical. For scenarios where data corruption is less severe and errors are spread across symbols, interleaving combined with ECC would be more effective.

3.8 Proposed Architecture for Handover

One of the significant challenges in the TransPod system is the frequent handover of communication between transmitters as the vehicle moves through different communication zones at high speeds. To address this issue, we propose a dual-frequency approach, utilizing two parallel channels operating at different frequencies, F_1 and F_2 . In this approach, the transmitters alternate their operating frequencies, such that adjacent transmitters work on different frequencies. For instance, T_{x1} operates at F_1 , the next transmitter T_{x2} at F_2 , the following one at F_1 again, and so on.

This dual-frequency system not only smooths the handover process but also provides diversity to mitigate the effects of impulsive noise at the receiver. The system can implement advanced error recovery techniques such as fountain coding, by maintaining redundancy with two active frequencies. Instead of transmitting the entire set of source packets through one link, the transmitted packets can be linearly combined and transmitted through the dual-link system.

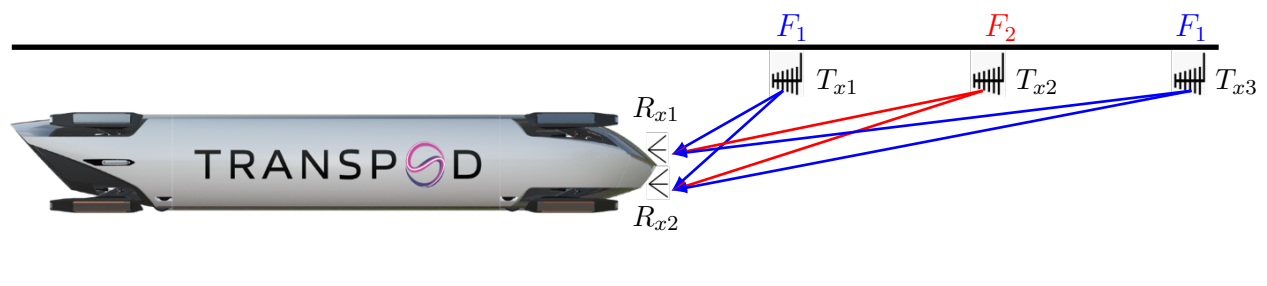


Figure 3.25: Dual-frequency system architecture.

3.9 Summary

In this chapter, we analyzed the path loss channel model based on ray-tracing within the vacuum tube of the tube-transportation system, such as TransPod. Both the LOS and NLOS components were considered, and the time-varying transfer function was derived. We examined large-scale and small-scale fading channel characteristics, including path loss, delay spread, and Doppler spread. Additionally, we investigated the measured noise in the context of the contactless power transmission system employed in the FluxJet vehicle, designed to operate on the fully-electric TransPod line. Our analysis included a detailed examination of recorded current samples associated with plasma arc discharges. We found that the noise measurements correlate closely with the instantaneous noise variance at the receiver of the communication system. A two-state Markov-Gaussian model was used to represent the measured noise. The results demonstrate that this model accurately fits the measurements, with minimal differences between the observed values and those predicted by the model. We suggest the use of erasure codes, such as fountain codes, and ECC codes combined with interleaving, to enhance data recovery and reliability in the presence of impulsive noise. Additionally, the dual-frequency approach, which alternates operating frequencies among adjacent transmitters, was presented to facilitate seamless handover and improve communication robustness. Design and simulation of these methods will be considered in future work.

4

OTFS Channel Estimation

Sommaire

| | | |
|-------|--|-----|
| 4.1 | Introduction | 98 |
| 4.2 | Motivation | 100 |
| 4.3 | Threshold-based Channel Estimation Algorithm | 101 |
| 4.4 | Problem Formulation | 108 |
| 4.5 | Sequence-based Pilot Channel Estimation | 115 |
| 4.5.1 | An Optimum Sequence | 119 |
| 4.5.2 | Pilot Sequence Placement | 120 |
| 4.5.3 | Channel Parameters Estimation | 122 |
| 4.5.4 | PAPR of the Sequence Pilot | 125 |
| 4.6 | Detection | 127 |
| 4.7 | Simulation Results | 128 |
| 4.7.1 | NMSE | 129 |
| 4.7.2 | BER | 132 |
| 4.8 | Summary | 133 |

THE objective of this chapter is to propose a correlation-based channel estimation method by inserting a sequence pilot in the OTFS grid. We begin by reviewing the conventional channel estimation technique using a single impulse pilot. Then, we discuss the proposed method and demonstrate how it reduces the PAPR of the signal in the time domain while decreasing channel estimation error.

4.1 Introduction

We have seen that OFDM was introduced to deal with the time-dispersive nature of the wireless channels [126], [127]. In OFDM, the channel frequency response is estimated for every OFDM symbol and used to equalize the channel [128], [129]. However, OFDM fails in performance in high mobility scenarios due to the wide Doppler spread [130], [131]. Furthermore, the channel frequency response changes very rapidly and the coherence time of the channel is short. In this scenario, in OFDM system, there is not sufficient time to estimate the channel. Channel estimation in the OFDM-based systems require multiple pilots interleaved along the time slots and sub-carriers to capture the time-frequency channel variations [132], [133]. In [chapter 2](#), we explored various channel representations. From the [Figure 3.12](#), we can see that in time-frequency representation, time-varying channel impulse response $H_{TF}(t, f)$ is varying rapidly in time and frequency, makes the channel estimation difficult. An equivalent representation was introduced in the delay-Doppler domain with impulse response $H_{DD}(\tau, \nu)$. In this model, the coefficients of the channel, or channel taps, correspond to reflectors with specific delay

and Doppler values [35]. The delay component is influenced by the distance traveled by the wave after being reflected, while the Doppler component depends on the relative velocity of the reflector. These velocities and distances tend to remain roughly constant over a long period, leading to the delay-Doppler channel representation appearing time-invariant over long duration compared to the time-frequency representation. The delay-Doppler channel representation captures the geometric characteristics of the channel. In many practical scenarios, the number of reflectors is low, leading to a sparse appearance of the channel in the delay-Doppler domain, with fewer peaks on the grid [134]. This sparsity reduces the number of parameters that need to be estimated. Furthermore, since the delay-Doppler coefficients remain constant for symbols over a long period, there is a decrease in both the pilot overhead ratio and the complexity of estimation.

After receiving the delay-Doppler symbols at the receiver, the initial step involves estimating the channel in order to mitigate its effects using equalizers. In time-frequency domain techniques like OFDM, pilots are transmitted through the channel, and the channel response over these pilot symbols is estimated. Then, the channel for all data symbols is extracted using interpolation [129]. For OTFS channel estimation, there are several approaches available. One of the approaches involves pilot-based channel estimation techniques that have been extensively studied in recent years [135]–[138]. The main concept is to place a single pilot symbol within the data frame, ensuring adequate guard space surrounds it in the delay-Doppler grid, and transmitting it alongside the data symbols. These guard symbols prevent interference between the data symbols and the pilot symbols after passing through the doubly dispersive channel. At the receiver, the pilot experiences delay and Doppler offsets, resulting in the multiple copies with varying power in the receiver delay-Doppler grid. The pilot symbol undergoes similar Doppler and delay shifts as the data symbols. Therefore, by observing the spread output in the estimation grid (pilot and guard symbols at the receiver), we can obtain the delay and Doppler indices corresponding to the relative distance and velocity of the reflectors, as well as the magnitude of gain provided by these reflectors. In this section, we review some of the existing works. The proposed method in [135] stands out as one of the most notable works. In this method, estimation is carried out by employing an optimal threshold that operates on the replicas of the

received pilot within the estimation grid. By examining the symbols within this grid, the positions of delay and Doppler indices can be identified. In the absence of noise, the channel coefficients can be determined by identifying the peaks in the grid, while considering the transmitted pilot power. However, in high noise conditions, extracting channel information becomes challenging due to the potential for detecting false peaks or missing some peaks in the grid. By adjusting the threshold, the probabilities of false or missed detection can be reduced. Consequently, the threshold significantly influences the performance of data detection at the receiver. Accurately identifying the correct peaks corresponding to the existing paths of the channel, requires higher pilot power. In [139], another estimation scheme is proposed, which is based on employing multiple pilot symbols to improve the performance of the threshold based method in the high noisy condition. However, this scheme makes use of prior information of the channel such as maximum delay, which may not be available. Several studies have focused on exploiting the sparsity of the channel by employing a compressive sensing approach for channel estimation, as indicated in [140]. These compressive sensing algorithms are complex and require more pilot data, resulting in high pilot overhead. Another category of channel estimation approaches is the use of superimposed pilots over the entire data symbols in the delay-Doppler grid [137], [138]. They claim that the guard space around the pilot symbol degrades the spectral efficiency especially for the small frame sizes. However, it also introduces additional complexity in the receiver design such as interference elimination process between the pilot and data symbols that requires complex signal processing techniques at the receiver. In this study, we focus on the first category where the pilot symbols are inserted with the data and guards symbols simultaneously.

4.2 Motivation

Considering the poor performance of the traditional threshold-based method using only one impulse pilot in high noise conditions, we suggest to use an approach utilizing multiple impulses. This aims to exploit diversity gain to improve the accuracy of channel estimation. In the next section, we begin by examining the conventional threshold-based channel estimation method employing a single impulse pilot [135], [136].

4.3 Threshold-based Channel Estimation Algorithm

In the classical channel estimation scheme, a single impulse pilot x_p with power $P_{\text{pilot}} = |x_p|^2$ is positioned at coordinates (m_p, n_p) within the delay-Doppler grid. It is accompanied by N_g guard symbols set to zero and $MN - N_g - 1$ data symbols $x_d[m, n]$. It is assumed that the maximum delay τ_{max} and maximum Doppler shift ν_{max} among all channel paths are known. The number of guard symbols are chosen to accommodate the maximum delay and Doppler spreads of the channel. The guard intervals are added on both sides of the pilot to prevent interference between pilot and data symbols at the receiver. Consequently, the guard symbols are arranged such that they remain zero within the range $m_p - l_{\text{max}} \leq m \leq m_p + l_{\text{max}}$ and $n_p - 2k_{\text{max}} \leq n \leq n_p + 2k_{\text{max}}$. The difference in arrangement along the delay and Doppler axes arises from the fact that delay taps can not be negative, but Doppler taps can be either negative or positive.

In [chapter 2](#), (2.10) defines the delay shifts τ_i as $\frac{l_i}{M\Delta f}$. Typically, the delay resolution $\frac{1}{M\Delta f}$ is sufficient to approximate the delay shifts as integer multiples of the sampling period $\frac{1}{M\Delta f}$. Consequently, the delay indices l_i can be considered as integer values, denoted by $l_i \in \mathbb{Z}$ [141], [35]. Similarly, the Doppler shifts ν_i are defined as $\frac{k_i}{NT}$. When N is large, the Doppler resolution $\frac{1}{NT}$ increases, enabling the Doppler indices k_i to be treated as integers as well, i.e., $k_i \in \mathbb{Z}$. However, for large N , the OTFS frame becomes longer, and the channel may change within the duration of one frame. Therefore, in practice, N is often chosen to be smaller than M to improve channel estimation performance. Consequently, with small values of N , the Doppler resolution decreases, and the Doppler indices become fractional, leading to $k_i \in \mathbb{R}$. In the following, we review transmitter and receiver delay-Doppler grid for both the integer and fractional Doppler indices.

- **Integer Doppler indices:** The arrangement of symbols in the delay-Doppler grid for integer Doppler indices is detailed in the following, as depicted in [Figure 4.1a](#):

$$X_{\text{DD}}[m, n] = \begin{cases} x_p & m = m_p, n = n_p \\ 0 & \begin{cases} m_p - l_{\text{max}} \leq m \leq m_p + l_{\text{max}} \\ n_p - 2k_{\text{max}} \leq n \leq n_p + 2k_{\text{max}} \end{cases} \\ x_d[m, n] & \text{otherwise} \end{cases} \quad (4.1)$$

Figure 4.1b represents the schematic representation of the received signal in the delay-Doppler domain. The green region within Figure 4.1b illustrates the estimation grid defined by $m_p \leq m \leq m_p + l_{\max}$ and $n_p - k_{\max} \leq n \leq n_p + k_{\max}$. Within this grid, a single impulse pilot is distributed among guard symbols due to the delay and Doppler characteristics of the channel. We utilize the received symbols within this green region specially for channel estimation purpose. Symbols outside this green region, highlighted in yellow, can be utilized for data detection alongside other symbols within the delay-Doppler grid denoted in blue.

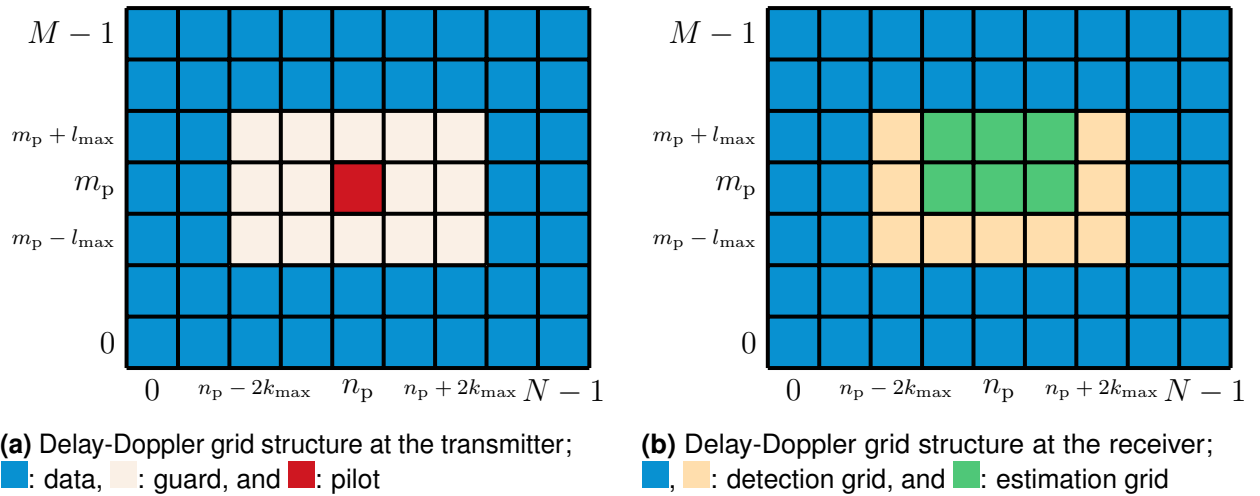


Figure 4.1: Symbols pattern at the transmitter and receiver for the classical impulse pilot scheme in [135].

To illustrate clearly, we consider an example with a delay-Doppler grid of size 16×16 . A single impulse pilot x_p with the power of $P_{\text{pilot}} = |x_p|^2$, is positioned at $[8, 8]$, surrounded by a guard band of size 7×9 . We assume the maximum delay index $l_{\max} = 3$ and the maximum Doppler index $k_{\max} = 4$. Figure 4.2 demonstrates the organization of data within the delay-Doppler domain at the transmitter. In this scenario, the channel exhibits delay indices $l_i = \{0, 1, 2, 3\}$ and Doppler indices $k_i = \{0, 1, 2, 3\}$ without the presence of noise. The received signal in the delay-Doppler domain is represented in Figure 4.3a. To provide a closer examination in the absence of noise, Figure 4.3b provides a zoomed-in view of the estimation grid area. This zoomed-in view clearly shows that the received delay and Doppler indices of the spread pilot symbol can be accurately extracted in the absence of noise.

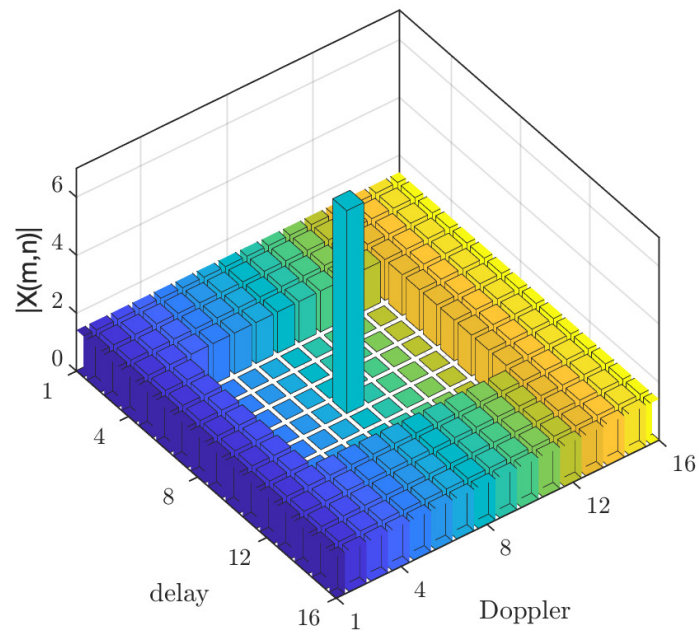


Figure 4.2: Transmitted symbols in delay-Doppler domain.

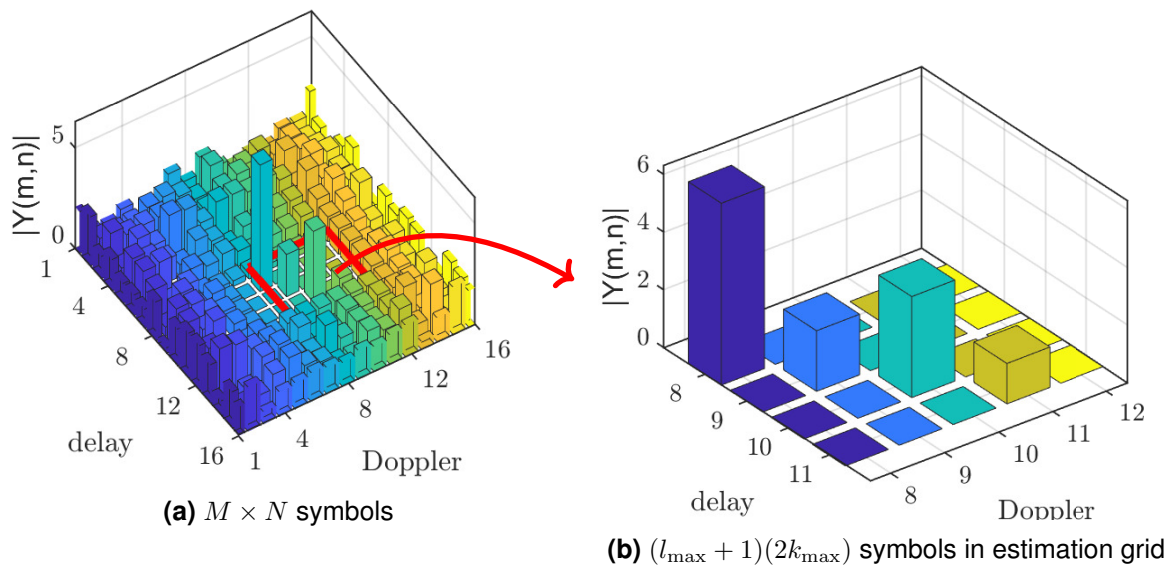


Figure 4.3: Received symbols in delay-Doppler domain.

We recall the input-output relation in the delay-Doppler given in (2.44):

$$\mathbf{Y}_{\text{DD}}[m, n] = \sum_{i=1}^P z^{k_i(m-l_i)} h_i \mathbf{X}_{\text{DD}} [[m - l_i]_M, [n - k_i]_N], \quad (4.2)$$

where $z = e^{\frac{j2\pi}{MN}}$. Each symbol in the estimation grid represents an existing channel path. Along the delay axis, the transmitted pilot symbol has been spread to be located at the position $m + l_i$, and along the Doppler axis at $n + k_i$, due to the channel characteristics. The relationship between the pilot symbol and its corresponding symbols in the received estimation region can be established as:

$$\mathbf{Y}_{\text{DD}}[m_p + l_i, n_p + k_i] = z^{k_i m_p} h_i \mathbf{X}_{\text{DD}}[m_p, n_p] = z^{k_i m_p} h_i x_p. \quad (4.3)$$

From the above equation, the delay taps l_i , Doppler taps k_i , and channel coefficients h_i can be estimated knowing the pilot symbol x_p and received symbols $\mathbf{Y}_{\text{DD}}[m_p + l, n_p + k]$ in $0 \leq l \leq l_{\text{max}}$ and $-k_{\text{max}} \leq k \leq k_{\text{max}}$. Moreover, it's important to mention that $h[l, k]$, the discrete delay-Doppler channel, represents the corresponding channel coefficient h_i :

$$h[l, k] = \begin{cases} h_i, & \text{if } l = l_i \text{ and } k = k_i \\ 0, & \text{otherwise.} \end{cases} \quad (4.4)$$

The estimated channel coefficients are denoted by $\hat{h}[l, k]$, calculated as:

$$\hat{h}[l, k] = \frac{\mathbf{Y}_{\text{DD}}[m_p + l, n_p + k]}{z^{k m_p} x_p}. \quad (4.5)$$

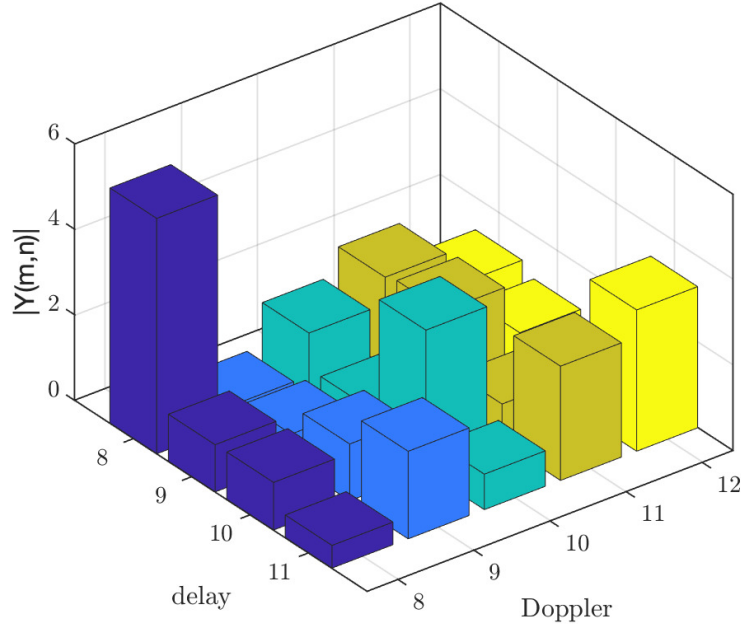


Figure 4.4: Pilot output grid in the presence of noise.

When noise is present, the pilot symbols at the receiver are contaminated, resulting in false detection. Multiple noisy peaks may be mistaken for the correct channel path, as depicted in [Figure 4.4](#). The input-output relationship of the pilot symbol is given by:

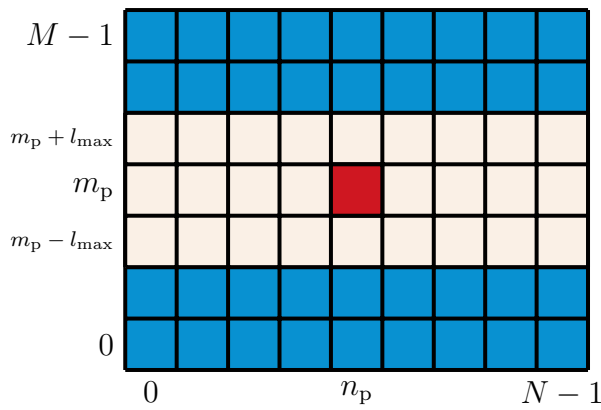
$$\mathbf{Y}_{\text{DD}}[m, n] = \sum_{i=1}^P z^{k_i(m-l_i)} h_i \mathbf{X}_{\text{DD}} [[m - l_i]_M, [n - k_i]_N] + \mathbf{n}[m, n], \quad (4.6)$$

where $\mathbf{n}[m, n]$ indicates Additive white Gaussian noise (AWGN) with zero mean and variance σ^2 . In [135], [136], a threshold-based method is used to remove false peaks in the estimation grid. According to this algorithm, if the magnitude of the received symbols in the estimation grid exceeds the noise-dependent threshold, the peak indicates the existence of a channel path, implying that the symbol is the weighted pilot symbol with noise; otherwise, it is considered only noise and is set to zero. The performance of this method is highly influenced by the chosen threshold; if it exceeds a certain value, false detection occurs, and for small values, it is more likely to detecting non-existent paths. Furthermore, following the recommendation

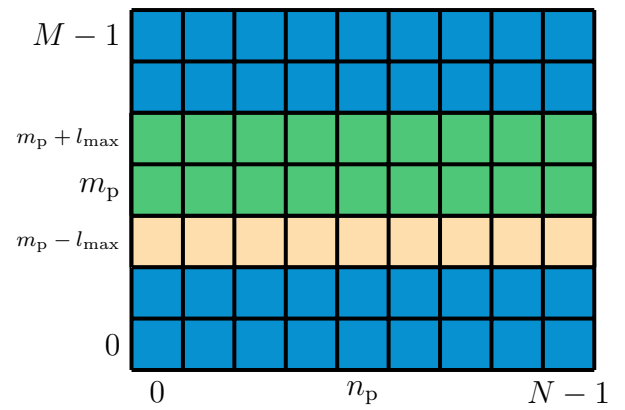
in [35], [135], the threshold is set to be 3σ to balance between false detection and miss detection probabilities.

- Fractional Doppler indices:** In this scenario, when the diffusion of fractional Doppler shift, ν , is not an integer multiple of the Doppler resolution $\frac{1}{NT}$, the resulting normalized Doppler shift k becomes fractional, leading to energy leakage on both sides of the resolvable Doppler shift [136], [142]. Fractional Doppler introduces a challenge to the sparsity of the channel in the delay-Doppler domain due to the energy leakage into all symbols along the Doppler axis. Essentially, for each delay tap, the pilot symbol spreads across all Doppler shift indices, $k = 0, \dots, N - 1$. For that reason, the whole area on the Doppler axis on both sides of the pilot should be considered as the guard interval. The arrangement of symbols in the delay-Doppler domain for the fractional Doppler case is illustrated below and shown in Figure 4.5a:

$$X_{DD}[m, n] = \begin{cases} x_p & m = m_p, n = n_p \\ 0 & \begin{cases} m_p - l_{\max} \leq m \leq m_p + l_{\max} \\ 0 \leq n \leq N - 1 \end{cases} \\ x_d[m, n] & \text{otherwise} \end{cases} \quad (4.7)$$



(a) Delay-Doppler grid structure at the transmitter; ■: data, ■: guard, and ■: pilot



(b) Delay-Doppler grid structure at the receiver; ■: data, ■: detection grid, and ■: estimation grid

Figure 4.5: Symbols pattern at the transmitter and receiver for the classical impulse pilot scheme for fractional Doppler indices in [136].

The received signal in the delay-Doppler domain is shown in Figure 4.5b, where the symbols within the green area correspond to pilot symbols utilized for channel estimation. The input-output relationship for the fractional Doppler indices is described in [35] as follows:

$$\mathbf{Y}_{\text{DD}}[m, n] = \sum_{i=1}^P z^{\kappa_i m_p} h_i \left(\sum_{k=0}^{N-1} \zeta_N(\kappa_i - k) \mathbf{X}_{\text{DD}}[[m - l_i]_M, [n - k]_N] \right), \quad (4.8)$$

where

$$\zeta_N(x) = \frac{1}{N} \sum_{k=0}^{N-1} e^{j2\pi x k / N} = \frac{1}{N} \frac{\sin(\pi x)}{\sin(\pi x / N)} e^{j\pi x(N-1)/N}. \quad (4.9)$$

The received signal in (4.9) can be expressed in terms of the pilot symbol x_p by setting $m = m_p + l_i$ and $n = n_p + k$ for $0 \leq l \leq l_{\max}$, $0 \leq k \leq N - 1$:

$$\begin{aligned} \mathbf{Y}_{\text{DD}}[m_p + l_i, n_p + k] &= h_i z^{\kappa_i m_p} \zeta_N(\kappa_i - k) \mathbf{X}_{\text{DD}}[m_p, n_p] \\ &= h_i \zeta_N(\kappa_i - k) x_p \end{aligned} \quad (4.10)$$

The delay-Doppler grid comprised of $M \times N$ points, is subdivided with a resolution of $\frac{1}{M\Delta f}$ in the delay axis and $\frac{1}{NT}$ in the Doppler axis. Consequently, the channel only detects integer multiples of the Doppler resolution, i.e, $k_i \in \mathbb{Z}$. Therefore, in the presence of a channel path with a fractional Doppler shift, it appears as multiple paths at integer Doppler shifts close to the fractional value. It is important to note that, in the case of fractional Doppler indices, the channel coefficients for every delay index l_i , are computed as follows:

$$h_i = \sum_{k=0}^{N-1} h[l_i, k] \quad (4.11)$$

To identify channel paths within the estimation area $0 \leq l \leq l_{\max}$ and $0 \leq k \leq N - 1$, a threshold is set for the magnitude of the received symbols to identify those exceeding it. The peaks detected with delay index l_i within the interval $m_p \leq l_i \leq l_{\max}$ indicate the presence of at least one existing channel path. The discrete delay-Doppler channel is estimated based on the detected symbols as follows:

$$\hat{h}[l_i, k] = \frac{\mathbf{Y}_{\text{DD}}[m_p + l, n_p + k]}{z^{k m_p} x_p}. \quad (4.12)$$

4.4 Problem Formulation

In the previous section, we explored the embedded pilot channel estimation method, which employs a single pilot symbol. This method takes advantage of the properties of the pilot symbol, which spread along both the delay and Doppler axes within the received OTFS frame for channel estimation. It offers a low-complexity estimation algorithm. However, its accuracy relies on ensuring that all pilot symbols, corresponding to the transmitted pilot symbol, exhibit greater strength than the noise. To accurately determine the output symbols at the receiver, which define the delay and Doppler taps of the channel, it is essential to use a pilot symbol with sufficiently high power, potentially much higher than that of the data symbols. Additionally, increasing the pilot power reduces the difference between the actual channel coefficients and their estimated values. Visual representations of the estimation grids for $P_{\text{pilot}} = 5$ and $P_{\text{pilot}} = 25$ can be seen in [Figure 4.6a](#) and [Figure 4.6b](#) respectively. The data SNR in this example is set to 10dB. In [Figure 4.7](#), the channel coefficients and their corresponding estimated values are depicted for pilot SNR of 5dB and 15dB. Increasing pilot power helps to decrease the channel estimation error.

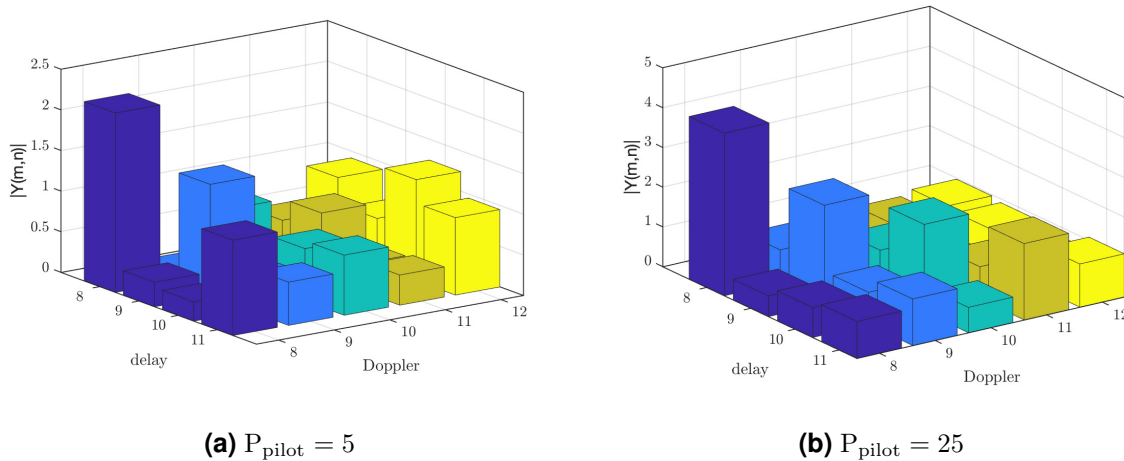


Figure 4.6: Estimation grid for $P_{\text{pilot}} = 5$ and $P_{\text{pilot}} = 25$.

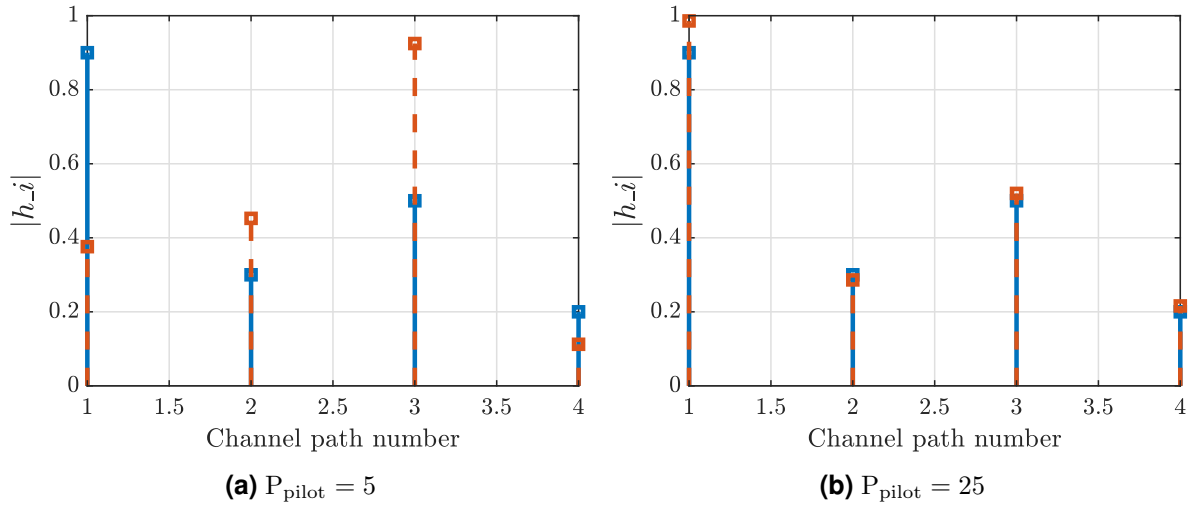


Figure 4.7: Amplitude of estimated channel coefficients for $P_{\text{pilot}} = 5$ and $P_{\text{pilot}} = 25$.

Moreover, when dealing with fractional normalized Doppler indices k_i , instead of integer ones, for each delay bin l_i , full Doppler bins in the Doppler axis are utilized to estimate channel coefficients. Given these considerations, the conventional channel estimation scheme faces several challenges:

1. The time-domain signal should be amplified prior to transmission through the wireless channel, making PAPR a critical metric for power amplifier efficiency evaluation [143]. The distribution of pilot and data symbols significantly influences the characteristics of the signal. Placing a high power single pilot in the delay-Doppler domain generates multiple spikes in the time domain with power levels exceeding that of other time domain samples, resulting in a high PAPR. Figure 4.8 illustrates the delay-Doppler domain signal with a high power impulse pilot located at position $[m_p, n_p]$ of the grid. After performing N -point IDFT to each row of the matrix \mathbf{X}_{DD} , the time-delay matrix is obtained as:

$$\mathbf{X}_{\text{td}}[m, l] = \frac{1}{\sqrt{N}} \sum_{n=0}^{N-1} \mathbf{X}_{\text{DD}}(m, n) e^{j \frac{2\pi l n}{N}}. \quad (4.13)$$

The single pilot is distributed along the time axis at row m_p . According to (4.13), the pilot symbols in the time-delay domain maintain a constant amplitude of $\sqrt{\frac{P_{\text{pilot}}}{N}}$ and linear phases $\frac{2\pi n_p l}{N}$, where $0 \leq l \leq N - 1$. Consequently, the average

power of the samples in \mathbf{X}_{td} at the delay index m_p exceeds that of other delay indices. Subsequently, the delay-time signal converts into a time domain vector $s = \text{vec}(\mathbf{X}_{td})$ for transmission. As illustrated in Figure 4.8, periodic peaks with high power are evident in the time domain signal.

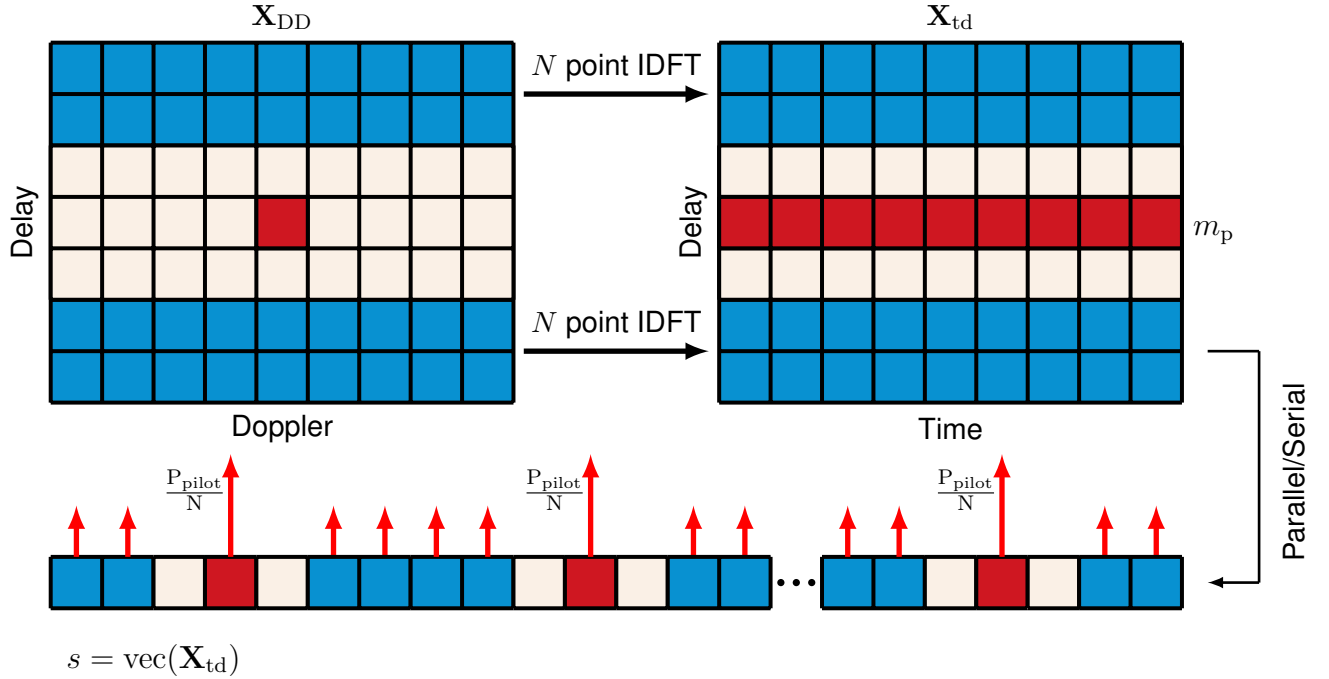


Figure 4.8: High-power impulse pilot causing elevated PAPR in the time-domain signal.

In the following, we derive an analytical PAPR expression for the OTFS transmitted signal. According to (2.26), the time domain samples of the OTFS transmitted signal are obtained through the IDZT which transforms \mathbf{X}_{DD} from the delay-Doppler domain to \mathbf{X}_{td} in the delay-time domain.

$$\mathbf{X}_{DD}[n, m] = \begin{bmatrix} x_0[0] & \cdots & x_0[N-1] \\ \vdots & \ddots & \vdots \\ x_{M-1}[0] & \cdots & x_{M-1}[N-1] \end{bmatrix} = \begin{bmatrix} \mathbf{x}_0 \\ \vdots \\ \mathbf{x}_{m-1} \end{bmatrix}, \quad (4.14)$$

where $\mathbf{x}_m \in \mathbb{C}^{N \times 1}$ represents the vectors containing the delay-Doppler symbols in the m -th row of \mathbf{X}_{DD} . After performing N -point IDFT of \mathbf{x}_m for each row of the

matrix \mathbf{X}_{DD} , delay-time domain matrix \mathbf{X}_{td} is given as:

$$\mathbf{X}_{td} = \mathbf{X}_{DD} \mathbf{F}_N^H = \begin{bmatrix} \tilde{\mathbf{x}}_0 \\ \vdots \\ \tilde{\mathbf{x}}_{m-1} \end{bmatrix}, \quad (4.15)$$

where $\tilde{\mathbf{x}}_m \in \mathbb{C}^{N \times 1}$ represents the column vectors containing the delay-time symbols in the m th row of \mathbf{X}_{td} . The time domain samples vector $\mathbf{s} \in \mathbb{C}^{MN \times 1}$ is obtained by vectorization of \mathbf{X}_{td} :

$$\mathbf{s}[m + nM] = \text{vec}(\mathbf{X}_{td}) = \frac{1}{\sqrt{N}} \sum_{n'=0}^{N-1} \mathbf{X}_{DD}(m, n') e^{j\frac{2\pi n n'}{N}}. \quad (4.16)$$

The PAPR of an OTFS transmitted signal \mathbf{s} is defined as:

$$\text{PAPR} = \frac{\max_{m,n} \{|s[m + nM]|^2\}}{P_{\text{avg}}}, \quad (4.17)$$

where

$$P_{\text{avg}} = \frac{1}{MN} \sum_{m=0}^{M-1} \sum_{n=0}^{N-1} \mathbb{E} \{|s[m + nM]|^2\}. \quad (4.18)$$

Substituting Equation (4.16) and (4.18) into Equation (4.17), we obtain:

$$\text{PAPR} = \frac{\max_{m,n} \left\{ \left| \frac{1}{\sqrt{N}} \sum_{n'=0}^{N-1} \mathbf{X}_{DD}[m, n'] e^{j\frac{2\pi n n'}{N}} \right|^2 \right\}}{\frac{1}{MN} \sum_{m=0}^{M-1} \sum_{n=0}^{N-1} \mathbb{E} \left\{ \left| \frac{1}{\sqrt{N}} \sum_{n'=0}^{N-1} \mathbf{X}_{DD}[m, n'] e^{j\frac{2\pi n n'}{N}} \right|^2 \right\}}. \quad (4.19)$$

Utilizing the Cauchy-Schwarz inequality [144], we derive:

$$\left| \sum_{n'=0}^{N-1} \mathbf{X}_{DD}[m, n'] e^{j\frac{2\pi n n'}{N}} \right|^2 \leq \sum_{n'=0}^{N-1} |\mathbf{X}_{DD}[m, n']|^2. \quad (4.20)$$

The PAPR is computed for two scenarios: when the delay-Doppler grid is filled with data symbols, and when an impulse pilot along with guard symbols are inserted in

the grid:

- **Full data:** Data symbols $\mathbf{X}_{DD}[m, n']$ are considered as independent and identically distributed (i.i.d.) random variables with zero mean and variance $\sigma^2 = \mathbb{E} \{ |\mathbf{X}_{DD}[m, n']|^2 \}$. $\alpha = \max_{m,n} \{ |\mathbf{X}_{DD}[m, n']|^2 \}$ represents the maximum power of the modulated symbols \mathbf{X}_{DD} . The upper bound for PAPR in (4.17) is given by:

$$\text{PAPR}_{\text{Full data}} \leq \frac{\max_{m,n} \left\{ \sum_{n'=0}^{N-1} |X_{DD}[m, n']|^2 \right\}}{\mathbb{E} \{ |X_{DD}[m, n']|^2 \}} = \frac{N\alpha}{\sigma^2}. \quad (4.21)$$

It's worth noting that the upper bound is achieved when data symbols in the grid have zero phases.

- **Impulse pilot with guard symbols:** Let us consider the insertion of an impulse pilot with power P_{pilot} into the grid along with guard symbols. Assuming the energy of the pilot symbol is spread along the delay axis at Doppler bin m_p , with surrounding zero guard symbols, the P_{avg} in (4.17) is expressed as:

$$P_{\text{avg}} = \frac{1}{MN} [(M - (2l_{\text{max}} - 1))N\sigma^2 + P_{\text{Imp}}]. \quad (4.22)$$

Maximum power of the row in \mathbf{X}_{td} containing pilot symbols is $\frac{P_{\text{pilot}}}{N}$. Finally, the PAPR is computed as:

$$\text{PAPR}_{\text{Impulse}} \leq \frac{\max \left\{ N\alpha, \frac{P_{\text{pilot}}}{N} \right\}}{\frac{1}{MN} [(M - (2l_{\text{max}} - 1))N\sigma^2 + P_{\text{pilot}}]}. \quad (4.23)$$

To analyze the statistical distribution of PAPR within the system, we generate a plot of the CCDF vs PAPR. This graphical representation aids in understanding how frequently the power of the signal exceeds a given threshold, which is linked to the PAPR of the signal. It provides insights into the probability distribution of peak power levels relative to the average power of the signal, allowing us to observe the

probability of encountering specific PAPR values within the signal. In Figure 4.9, we illustrate the CCDF of PAPR for the transmitted OTFS signal s , for the scenario where the grid contains only data symbols, and also where an impulse pilot of different powers is employed. In Figure 4.9, parameters $M = 128$, $N = 32$, and 4-QAM modulation are employed.

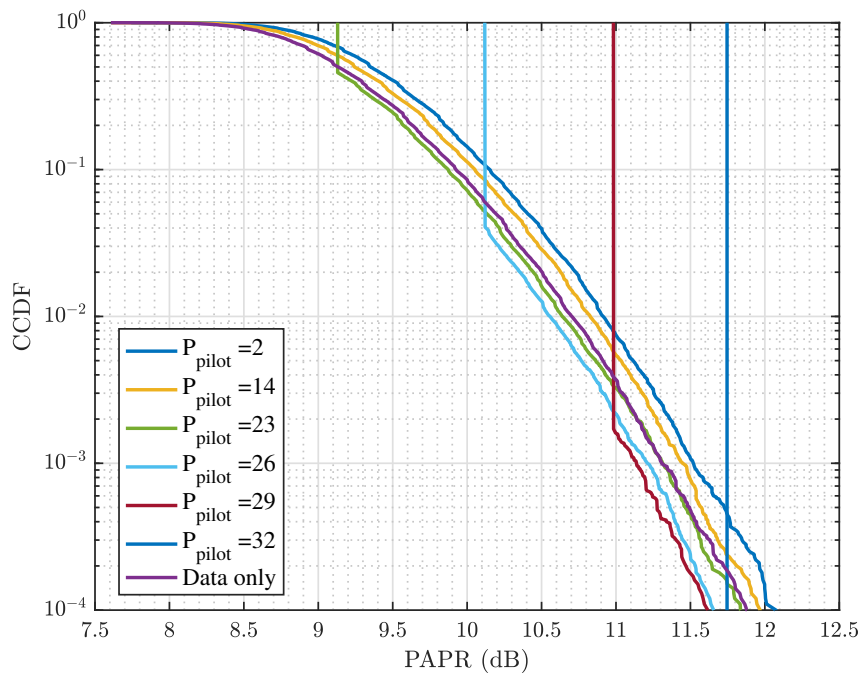


Figure 4.9: Comparison of CCDF of the PAPR for full data transmission, and impulse pilot with low and high pilot power P_{pilot} .

To improve the accuracy of channel estimation within the conventional threshold-based method [135], using an impulse pilot with higher power becomes necessary. As indicated by (4.23) and evidenced in Figure 4.9, increasing the power of the pilot leads to a significant increase in the ratio $\frac{P_{\text{pilot}}}{N}$ compared to the data symbols. When the pilot power is large, the pilot's contribution to the signal power becomes dominant. Consequently, the maximum value in the time domain signal and the PAPR of the signal is heavily influenced by the pilot symbol. This is where we can see the vertical lines in the Figure 4.9. For the small pilot powers, the data symbols contribution to the signal power becomes significant. In each iteration, the maximum power of the signal can vary due to different data symbol configurations,

leading to fluctuations in the peak power value for different iterations. In the transition region, around $P_{\text{pilot}} = 23$, the PAPR values can be influenced by the pilot or the data symbols, leading to a mix of fixed and variable PAPR values.

2. The conventional embedded channel estimation methods fail to estimate fractional Doppler indices $\kappa_i \in \mathbb{R}$, making it impossible to estimate the fractional Doppler shifts $\nu_i = \frac{\kappa_i}{NT}$. As discussed in [section 4.3](#) of the current chapter, instead of estimating individual Doppler indices, the discrete delay-Doppler response $h[l_i, k]$ is estimated, representing the full normalized Doppler shifts for each path with normalized delay l_i . In [\[35\]](#), this discrete delay-Doppler response is referred to as the channel Doppler response. [Figure 4.10](#) illustrates an example of the estimation grid in the delay-Doppler domain for a channel with delay indices $l_i = [0, 1, 2, 3]$ and Doppler indices $\kappa_i = [0, 1.2, 2.5, 3.7]$, with $P = 4$ existing paths, in the absence of noise. It is observed that at each delay bin within the interval $0 \leq l \leq 3$, the discretization of Doppler indices leads to leakage into all Doppler bins. Consequently, it appears that there are more channel paths than the actual number P . In this case, instead of fractional Doppler shift κ_i , the nearest integer k_i is estimated. To estimate the channel coefficients in [\(4.12\)](#), $z^{\kappa_i(m-l_i)}$ is applied as the phase rotation, resulting in the error $z^{(\kappa_i-k_i)(m-l_i)}$, which degrades the estimation performance. One of the possible solutions to maintain the sparsity of the delay-Doppler channel and decrease the leakage effect, can be changing pulse shaping waveform at the transmitter or receiver which has been studied in [\[145\]](#). Another potential solution is utilizing Deep Learning (DL) methods which will be studied in more details in [chapter 5](#).

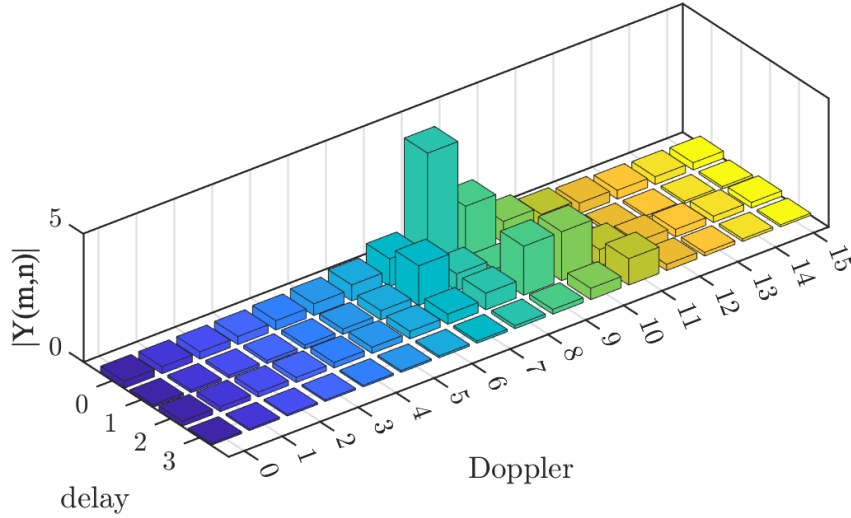


Figure 4.10: Pilot output grid with fractional Doppler indices $\kappa_i = [0, 1.2, 2.5, 3.7]$ and delay indices $l_i = [0, 1, 2, 3]$ in the absence of noise.

4.5 Sequence-based Pilot Channel Estimation

In this chapter, our main focus is on addressing the first aspect of the problem formulation. We have observed that achieving accurate channel estimation within the classical estimation scheme requires the transmission of an impulse pilot with high power. However, this leads to a high PAPR in the time domain signal. One potential solution to mitigate the PAPR effect is to distribute the pilot power across multiple pilot symbols within the delay-Doppler grid to achieve a more balanced power distribution. [Figure 4.11](#) visually represents the pilot structure on the delay-Doppler grid, where a sequence of length L_P is inserted along the delay axis. The pilot power P_{pilot} is evenly distributed across the L_P delay bins, with each symbol carrying the same power of $\frac{P_{\text{pilot}}}{L_P}$. After performing an N -point IDFT, the pilot sequence extends across the time axis, with each element having equal power of $\frac{P_{\text{pilot}}}{N_{L_P}}$.

To avoid the interference at the receiver, it is important to consider guard space in both the delay and Doppler axes. However, allocating guard space at the top and bottom

of the sequence can lead to a decrease in spectral efficiency. In the study by [146], a pilot structure is proposed to distribute the impulse pilot power P_{pilot} over the $2L - 1$ delay bins. They utilize a pilot sequence at the Doppler index n_p and delay indices $m_p, \dots, m_p + L - 1$. They append the last $L - 1$ symbols of the sequence to be inserted at delay indices $m_p - L, \dots, m_p - 1$ to absorb the interference from data symbols. They estimate the channel in the delay-Doppler domain based on the Least Squares (LS) and Minimum Mean Square Error (MMSE) criterion. Given the interference from pilot symbols into data symbols due to the multipath effect of the channel, they subtract the pilot from the received signal using the estimated channel matrix. In [147], the authors propose placing the pilot symbols throughout the entire zero-padded area in the ZP-OTFS system. They employ a joint channel estimation and data detection method, iteratively managing interference between the pilot and data symbols.

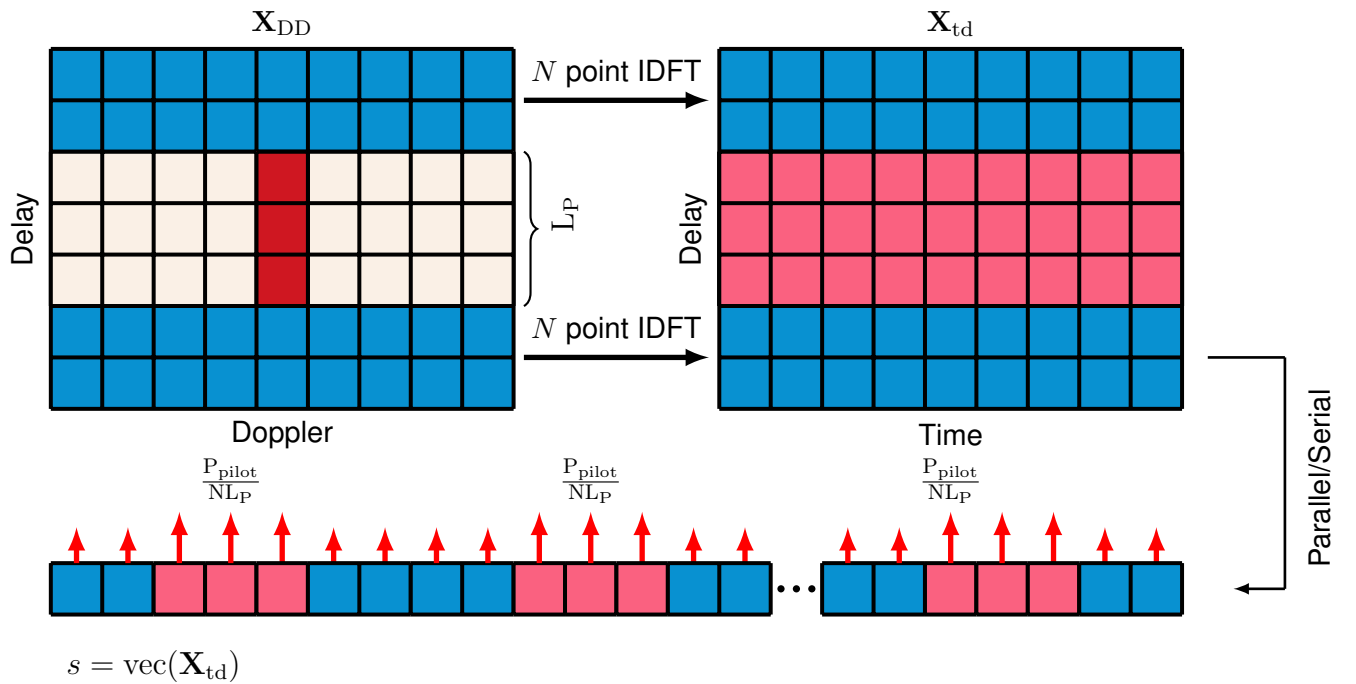


Figure 4.11: Sequence pilot balancing power distribution in the time domain signal.

In our proposed method [23], we employ a sequence pilot on delay bin m_p that occupies all Doppler bins, differing from previous works where the sequence is spread across the delay axis, as seen in Figure 4.12. Referring back to (2.33) in chapter 2, the

delay-Doppler channel matrix was formulated as:

$$\mathbf{H}_{DD} = \sum_{i=1}^P h_i \Pi^{l_i} \Delta^{k_i}. \quad (4.24)$$

Taking inspiration from this equation, we consider that the data experiences offsets along the delay axis and cyclic shifts in the Doppler dimension after coupling with the channel, with corresponding delay taps l_i and Doppler taps k_i . The pilot sequence at each delay index l_i appears to undergo cyclic shifts due to the corresponding Doppler index k_i .

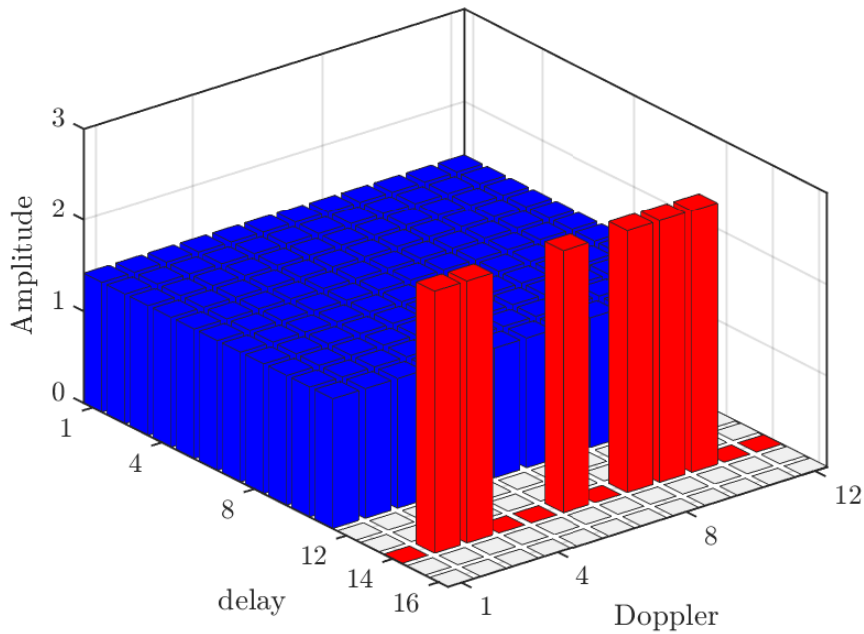


Figure 4.12: Pilot sequence, guard, and data symbol placements in the Delay-Doppler domain at the transmitter, with $N = 12$, $M = 16$, $m_p = 14$, and $\ell_{\max} = 2$,
■ data, ■ pilot, and ■ guard.

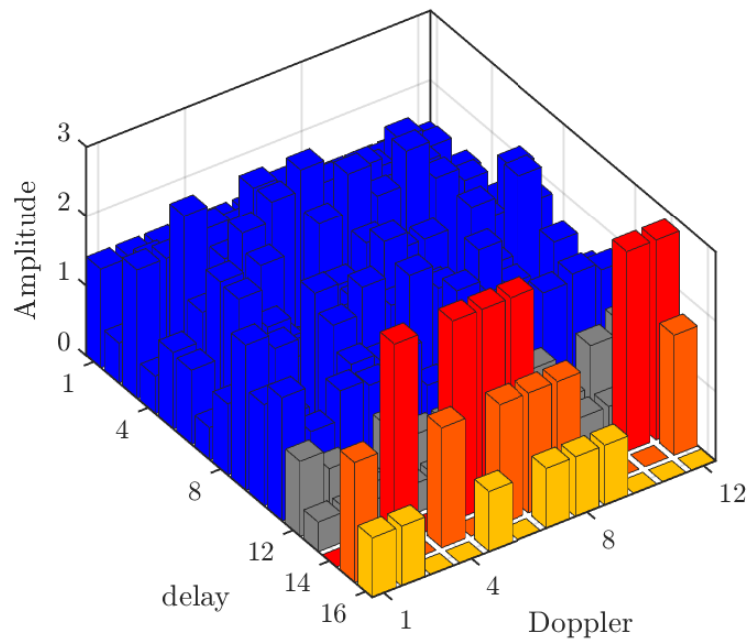


Figure 4.13: Channel effect on sequence pilot in delay-Doppler domain with $l = \{0, 1, 2\}$ and $k = \{3, 2, 1\}$. ■ data, ■ pilot at l_0 , ■ pilot at l_1 , ■ pilot at l_2 , and ■ channel effect of the data symbols spread on the guard area above the pilot.

When the signal passes through the channel, multiplying the channel matrix by the pilot sequence indicates that the l_i th path introduces a l_i -step cyclic shift of the sequence, denoted by Π^{l_i} and modulates it with a carrier at frequency k_i , represented by Δ^{k_i} . Figure 4.13 provides an example of how the pilot sequence experiences offsets on the delay axis with $l_i = \{0, 1, 2\}$, and cyclic shifts in the Doppler dimension with $k_i = \{3, 2, 1\}$ after coupling with the channel. To have a clear representation in this example, we utilized PN sequence with combination of 1's and 0's. To estimate the delay and Doppler taps of the channel, we propose a correlation-based estimation method. This method involves searching for the spread pilot sequence on the rows of the estimation grid in the delay-Doppler domain. This is accomplished through a correlation operation performed between the transmitted pilot sequence and the received signal. The peak of the resulting 2D correlation surface indicates the delay and Doppler shifts caused by the channel. The height of the peak reflects the degree of similarity, while the location of the peak indicates the amount of shift.

In the following section, we will discuss how to select an appropriate sequence that can effectively adapt to the correlation-based method, with desirable low PAPR properties.

4.5.1 An Optimum Sequence

To utilize the correlation-based method for estimating channel parameters, it is crucial to choose a sequence with high auto-correlation and low cross-correlation characteristics. In communication systems, training sequences, such as PN sequences and CAZAC sequences, are crucial for synchronization due to their sharp correlation peaks and minimal side lobes [148]–[150]. PN sequence, is a deterministic binary sequence that appears random but is generated by a deterministic algorithm. The most common type of PN sequence is the M -sequence, known as maximum-length sequence. M -sequences are the sequences of maximum possible period of $N = 2^m - 1$ where $m \in \mathbb{N}$. They are generated using a primitive polynomial over a finite field [151], [152]. In [153], the PN sequence pilot was used for the channel parameters estimation. CAZAC sequences are significant in communication systems due to their constant amplitude and zero auto-correlation for any nonzero circular shifts, making them suitable for synchronization, channel estimation, and reducing PAPR [154]. Moreover, after reviewing relevant literature, it becomes apparent that CAZAC sequences exhibit superior correlation properties compared to PN sequences [155], [156].

For an N -length CAZAC sequence represented by $c(n)$ where M is relatively prime to N , n th symbol $c(n)$ is given by:

$$c(n) = \exp\left(\frac{j\pi n M(n + \text{mod}(N, 2))}{N}\right). \quad (4.25)$$

The auto-correlation function of the CAZAC sequence $c(n)$ is defined as follows:

$$R(\delta) = \sum_{n=1}^N c(n)c^*(n + \delta) = \begin{cases} N, & \delta = 0 \\ 0, & \delta \neq 0 \end{cases}. \quad (4.26)$$

The normalized auto-correlation of both the CAZAC and PN sequences is given in [Figure 4.14](#). It is important to observe that the CAZAC sequence demonstrates reduced side lobes in its auto-correlation compared to the PN sequence. Furthermore, a notable characteristic of the CAZAC sequence is its resilience to change under DFT

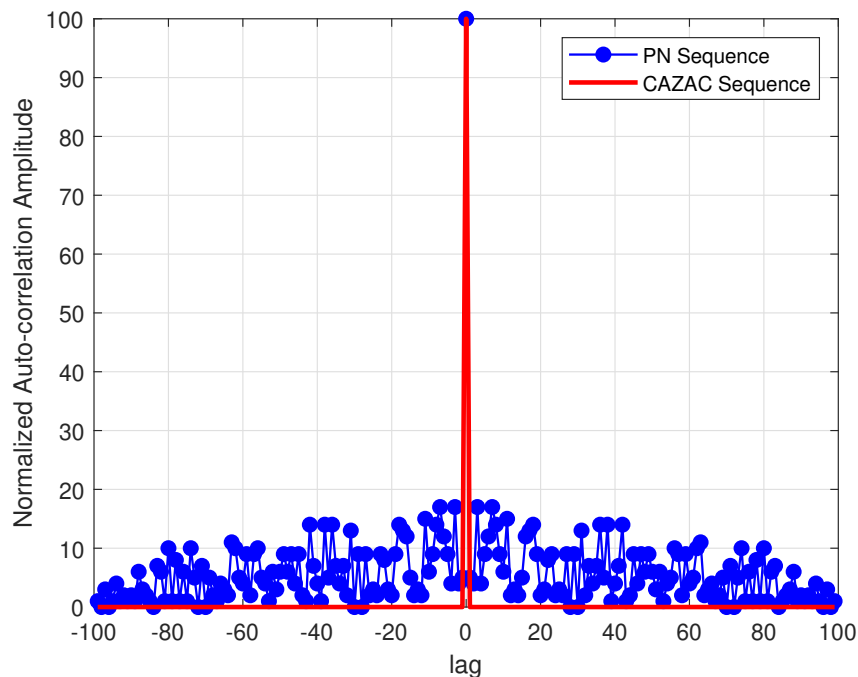


Figure 4.14: Auto-correlation function of the CAZAC and PN sequences

or IDFT, maintaining its properties. Thus, the resulting sequence after DFT/IDFT operations remains a CAZAC sequence, ensuring constant amplitude across both time and frequency domains. This property is particularly advantageous in our study as it helps to limit the PAPR of the time domain signal, contributing to improved system performance.

4.5.2 Pilot Sequence Placement

In [chapter 2](#), we discussed about the different OTFS variants. Since we loose the spectral efficiency due to the pilot sequence and guard symbol, in this section we analyze the effect of channel estimation and pilot location on the spectral efficiency of the OTFS variants [35], [157]. Let us consider $L_{ZP} = L_{CP} = L$. The [Figure 4.15](#) illustrates the structure of delay-Doppler grid with pilot sequence and guard symbols for CP-OTFS and ZP-OTFS. The variants RCP-OTFS/RZP-OTFS are shown in the [Figure 4.16](#). We calculate the spectral efficiency of the OTFS schemes in the [Table 4.1](#).

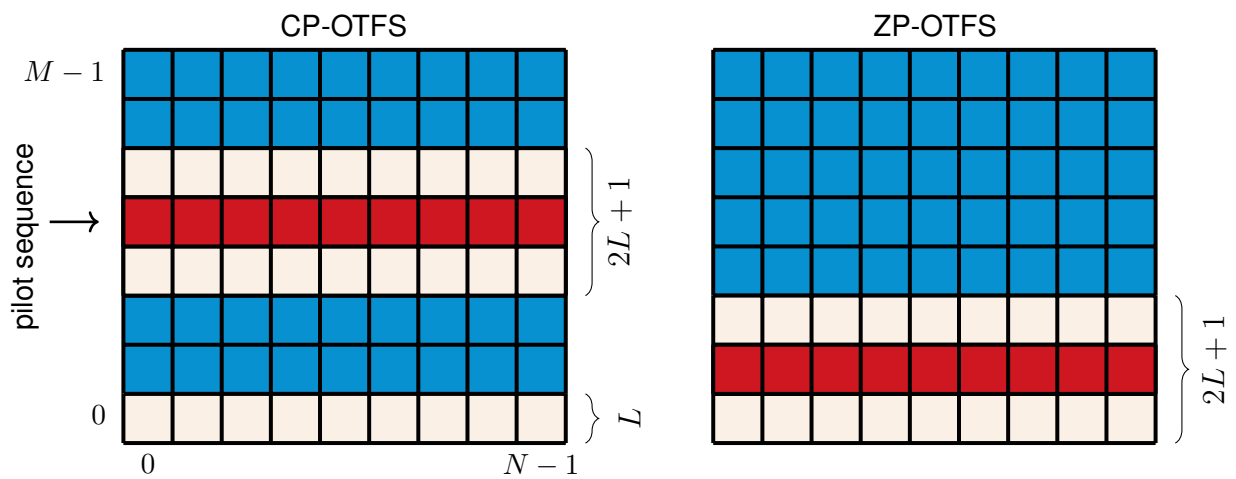


Figure 4.15: delay-Doppler grid structure with pilot sequence for CP-OTFS and ZP-OTFS; ■: data, ■: guard, and ■: pilot sequence.

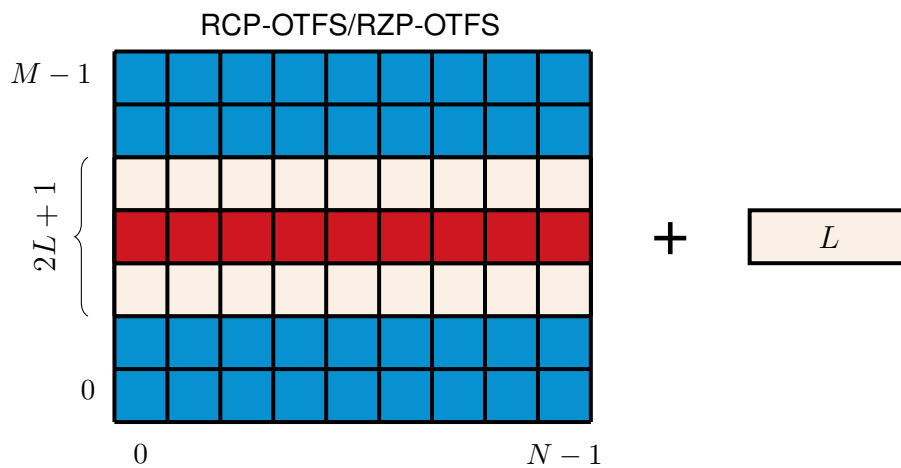


Figure 4.16: delay-Doppler grid structure with pilot sequence for RCP/RZP-OTFS; ■: data, ■: guard, and ■: pilot sequence.

Table 4.1: Spectral efficiencies of OTFS variants with/without sequence pilot insertion for channel estimation.

| | Spectral efficiency without pilot/guard | Spectral efficiency with pilot/guard |
|---------|---|--------------------------------------|
| CP | $\frac{M - L}{M}$ | $\frac{M - (3L + 1)}{MN}$ |
| ZP | $\frac{M - L}{M}$ | $\frac{M - (2L + 1)}{MN}$ |
| RZP/RCP | $\frac{MN}{MN + L}$ | $\frac{M - (2L + 1)}{MN + L}$ |

From the [Table 4.1](#) it is evident that ZP-OTFS offers the highest spectral efficiency among the other variants. This high performance is due to the utilization of zero-padding samples in ZP-OTFS, not only to prevent the interference among OTFS frames in the time domain but also serve as guard space between data and pilot samples. Therefore, in our study, we choose the ZP variant of OTFS. We position the pilot sequence within the zero-padded region, enabling the pilot to spread into the zero-padding samples due to the delay and Doppler spread of the channel.

4.5.3 Channel Parameters Estimation

Let us denote the pilot sequence $\mathbf{X}_p = [x_{p_0}, x_{p_1}, \dots, x_{p_{N-1}}]$ as a CAZAC sequence with N samples, located at delay bin m_p and occupying all Doppler bins. Together with the data symbols $x_d[m, n]$, they form the transmission frame of ZP-OTFS:

$$X_{DD}[m, n] = \begin{cases} x_p[n] & m = m_p, 0 \leq n \leq N - 1 \\ 0 & \begin{cases} m_p - l_{\max} \leq m \leq m_p + l_{\max} \\ 0 \leq n \leq N - 1 \end{cases} \\ x_d[m, n] & \text{otherwise} \end{cases} \quad (4.27)$$

[Figure 4.17](#) illustrates the original CAZAC sequence located at delay bin m_p .

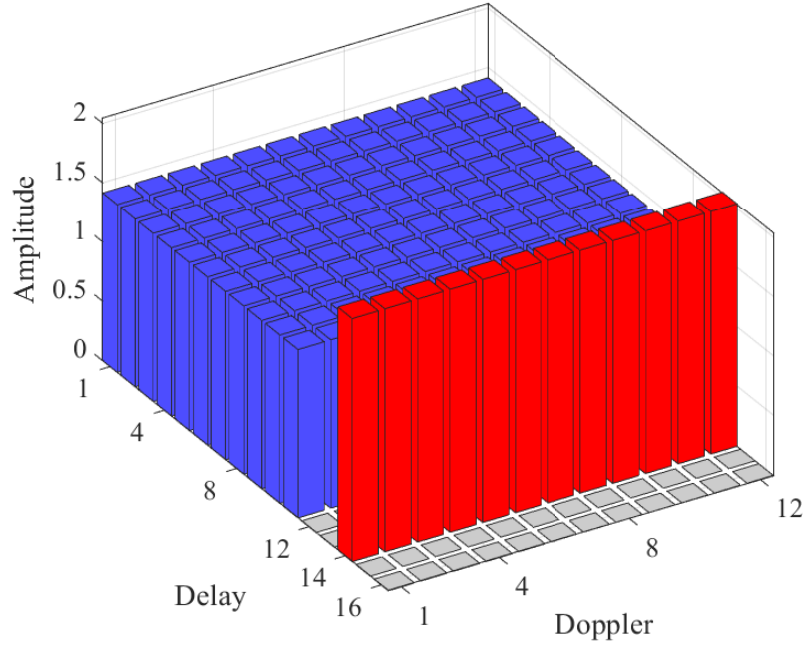


Figure 4.17: CAZAC sequence in the Delay-Doppler domain at the transmitter located at delay bin $m_p = 14$, and $\ell_{\max} = 2$, ■ data, ■ pilot, and ■ guard.

To estimate three quantities of interest, delay taps l_i , Doppler taps k_i , and coefficients h_i for the i th path, where $i = 1, \dots, P$, the following procedure needs to be implemented.

To estimate the delay and Doppler taps, we search across the delay dimension of the received signal \mathbf{Y} within the estimation region to identify the highest similarity with the transmitted pilot sequence. For each row m on the estimation grid $\{m_p : M, :\}$, a sliding window of length N is employed. This process can be implemented by forming the cross-correlation function between the known pilot sequence \mathbf{X}_p and each row of received signal \mathbf{Y} , resulting in a matrix $\mathbf{R}[m, n]$ where $m_p \leq m \leq M$, $0 \leq n \leq N$:

$$\mathbf{R}[m, n] = \sum_{u=0}^{N-2} \mathbf{Y}^*[m, n+u] \mathbf{X}_p[u+n+1]. \quad (4.28)$$

For each row m on the delay axis, the values are summed across the Doppler axis to obtain:

$$\mathbf{C}[m] = \sum_{n=0}^{N-1} \mathbf{R}[m, n], \quad (4.29)$$

The peaks of $\mathbf{C}[m]$ function indicate potential delay and Doppler shifts introduced by the channel, where the height of each peak reflects the degree of similarity. To filter out the false paths caused by the AWGN noise, a threshold ζ is applied to the elements of $\mathbf{C}[m]$. The estimated number of paths \hat{P} correspond to the count of elements exceeding ζ . These indices determine the rows in \mathbf{Y} where the pilot sequence \mathbf{X}_p is located, thereby indicating the presence of a path. Given the use of a CAZAC sequence, a prominent peak in the correlation function is expected. Let $\mathcal{L} = \{\hat{l}_i\}$ for $0 \leq i \leq \hat{P}$ represent the set of estimated delays, obtained as follows:

$$\mathcal{L} = \{\hat{l}_i \mid \mathbf{C}[m] > \zeta \text{ for some } m\}. \quad (4.30)$$

For each detected delay, the Doppler shift is determined by identifying the circular shift of the sequence at each matched row m using the index of the maximum value of $\mathbf{C}[m]$:

$$\hat{k}_i = \operatorname{argmax}_{\hat{l}_i \in \mathcal{L}} \left(\|\mathbf{C}[\hat{l}_i]\| \right). \quad (4.31)$$

The discrete delay-Doppler channel $\hat{h}[\hat{l}, \hat{k}]$ can then be estimated by element-by-element division and averaging of the received pilot symbols at the corresponding delay tap \hat{l}_i and Doppler tap \hat{k}_i by the pilot sequence \mathbf{X}_p :

$$\hat{h}[\hat{l}, \hat{k}] = \frac{1}{N} \sum_{k=0}^{N-1} \frac{\mathbf{Y}[m_p + \hat{l}, k + \hat{k} \bmod N]}{z^{\hat{k}m_p} \mathbf{X}_p[k]}, \quad \text{for } 0 < \hat{l} < \hat{l}_i, -\hat{k}_i < \hat{k} < \hat{k}_i. \quad (4.32)$$

The estimated channel coefficients \hat{h}_i can be obtained from $\hat{h}[\hat{l}, \hat{k}]$ as the following

$$\hat{h}_i = \begin{cases} \hat{h}[\hat{l}, \hat{k}], & \text{if } \hat{l} = \hat{l}_i \text{ and } \hat{k} = \hat{k}_i \\ 0, & \text{otherwise.} \end{cases} \quad (4.33)$$

The steps of the processing are summarized in [Algorithm 1](#). Finally, we compute the estimated discrete delay-time channel response $\hat{h}_{\text{td}}^s[l, q]$ for $q = 0, \dots, NM - 1$ and $l \in \mathcal{L}$, as previously formulated in (2.36):

$$\hat{h}_{\text{td}}^s[l, q] = \sum_{i=1}^{\hat{P}} \hat{h}_i z^{\hat{k}_i(q-l)} \delta(l - \hat{l}_i). \quad (4.34)$$

Algorithm 1: Estimation of Delay Taps, Doppler Taps, and Coefficients

Input: Received signal $\mathbf{Y}[m_p : M, :]$, transmitted pilot sequence \mathbf{X}_p , threshold ζ
Output: Estimated delay taps \hat{l}_i , Doppler taps \hat{k}_i , and coefficients \hat{h}_i

Estimation of Delay and Doppler Taps:

1. Compute cross-correlation function $\mathbf{R}[m, n]$ using (4.28)
2. Sum across Doppler axis: $\mathbf{C}[m] = \sum_{n=0}^{N-1} \mathbf{R}[m, n]$
3. Identify peaks in $\mathbf{C}[m]$ exceeding threshold ζ to obtain set \mathcal{L}
4. $\hat{k}_i = \operatorname{argmax}_{l_i \in \mathcal{L}} (\|\mathbf{C}[l_i]\|)$

Estimation of Channel Coefficients:

5. Circularly shift $\mathbf{Y}[m_p + \hat{l}_i, :]$ by $-\hat{k}_i$ positions to align with the pilot sequence:
 $\mathbf{Y}[m_p + \hat{l}_i, k + \hat{k}_i \bmod N]$
6. Perform element-by-element division of the circularly shifted
 $\mathbf{Y}[m_p + \hat{l}_i, k + \hat{k}_i \bmod N]$ with $z^{\hat{k}_i m_p} \mathbf{X}_p[k]$
7. Average the results over N elements to obtain the discrete
 delay-Doppler channel $\hat{h}[\hat{l}, \hat{k}]$ in (4.32)
8. Extract the estimated channel coefficient \hat{h}_i from $\hat{h}[\hat{l}, \hat{k}]$ using (4.33)

Output: \hat{l}_i , \hat{k}_i , and \hat{h}_i

4.5.4 PAPR of the Sequence Pilot

To ensure a fair comparison with the conventional method utilizing a single impulse pilot, we adjust the power of the sequence pilot to match that of the conventional method. Consequently, we distribute the pilot power P_{pilot} along the sequence to have equally powered elements of $\frac{P_{\text{pilot}}}{N}$. When the ISFFT operation is applied, the power of the pilot symbols is spread along the time axis. Additionally, the power of the CAZAC sequence symbols remains constant even after the ISFFT operation. As a result, the power distribution of the symbols along the time axis stays consistent with what would be observed if one impulse pilot were placed in the delay-Doppler domain. Hence, the PAPR remains unchanged as illustrated in Figure 4.18. Figure 4.19 visually illustrates how the power of the CAZAC sequence along the Doppler axis is distributed in time domain. It can be observed that the power distribution is the same as the impulse pilot illustrated in Figure 4.8.

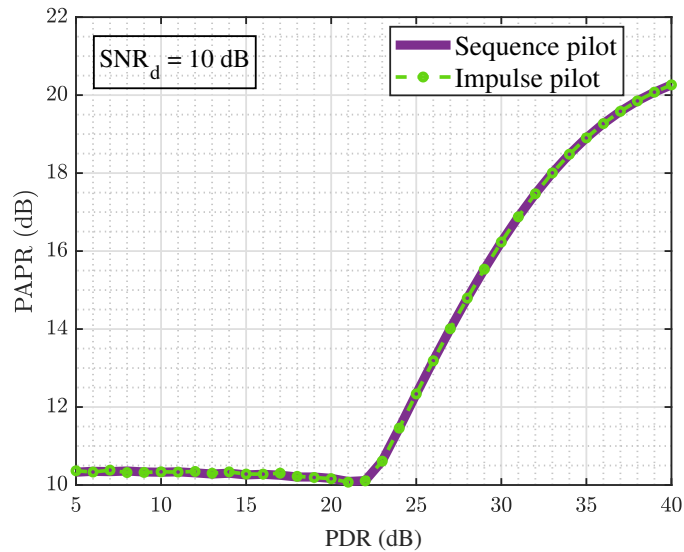


Figure 4.18: PAPR vs PDR for impulse pilot and sequence pilot.

However, as we will observe in the subsequent section detailing the results analysis, the proposed channel estimator outperforms the conventional method in mitigating channel estimation errors. This implies that the proposed method achieves the same level of channel estimation accuracy while using less pilot power resource, which in turn results in a lower PAPR of the corresponding time domain signal. Therefore, even though distributing the pilot symbols along the Doppler axis does not directly alter the PAPR, we can achieve an indirect reduction in PAPR when the channel estimation error decreases with the proposed method.

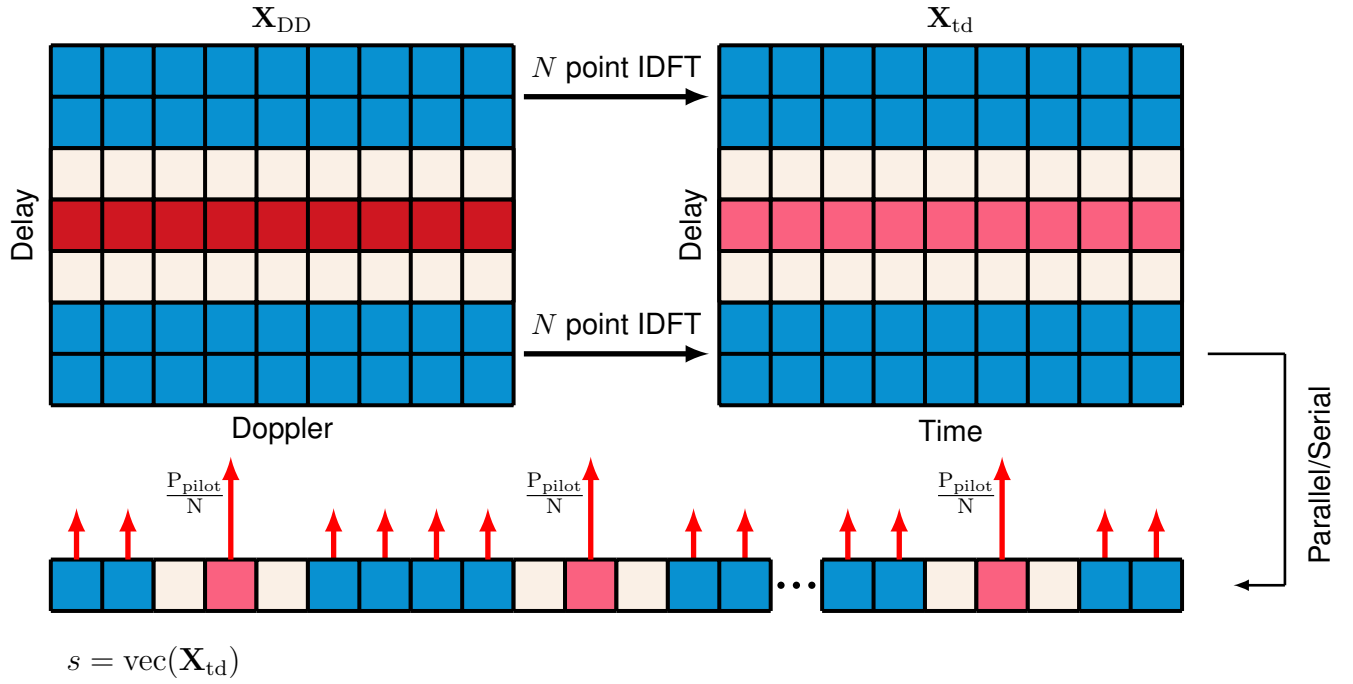


Figure 4.19: High-power impulse pilot causing elevated PAPR in the time-domain signal.

4.6 Detection

Let us recall the discrete received signal $y[q]$, as previously given in (2.31) for $q = 0, \dots, NM - 1$:

$$y[q] = \sum_{i=1}^P h_i z^{k_i(q-l_i)} x[q-l_i]. \quad (4.35)$$

The above equation can be expressed in terms of the discrete delay-time channel response $h_{td}^s[l, q]$ given in (2.36):

$$y[q] = \sum_{l \in \mathcal{L}} h_{td}^s[l, q] x[q-l], \quad (4.36)$$

where \mathcal{L} is the set of estimated delays. In (4.14), we observed that the discrete transmitted time-domain signal, denoted by \mathbf{s} , is a vector representation of the matrix \mathbf{X}_{td} containing delay-time domain samples. Specifically, it includes delay-time vectors $\tilde{\mathbf{x}}_m \in \mathbb{C}^{N \times 1}$. This can be expressed as:

$$\mathbf{s}(m + nM) = \tilde{\mathbf{x}}_m(n). \quad (4.37)$$

Similarly, the discrete received time-domain signal y can also be expressed using the delay-time vectors $\tilde{\mathbf{y}}_m \in \mathbb{C}^{N \times 1}$ as:

$$y(m + nM) = \tilde{\mathbf{y}}_m(n). \quad (4.38)$$

Subsequently, (4.36) can be reformulated in terms of the delay-time vectors $\tilde{\mathbf{x}}_m$ and $\tilde{\mathbf{y}}_m$ can be expressed as:

$$\tilde{\mathbf{y}}_m(n) = \sum_{l \in \mathcal{L}} \hat{h}_{\text{td}}^s[l, m + nM] \tilde{\mathbf{x}}_{m-l}(n) = \sum_{l \in \mathcal{L}} \hat{h}_i z^{\hat{k}_i(m-l)} e^{\frac{2j\pi \hat{k}_i n}{N}} \tilde{\mathbf{x}}_{m-l}(n). \quad (4.39)$$

To transition to the delay-Doppler domain, we apply an N -point FFT to (4.39), resulting in:

$$\mathbf{y}_m = \mathbf{F}_N \cdot \tilde{\mathbf{y}}_m = \sum_{i=1}^{\hat{P}} \hat{h}_i z^{\hat{k}_i(m-\hat{l}_i)} \otimes \mathbf{x}_{m-\hat{l}_i}, \quad (4.40)$$

where \mathbf{x}_m and $\mathbf{y}_m \in \mathbb{C}^{N \times 1}$ represent the vectors containing the delay-Doppler symbols in the m th row of \mathbf{X}_{DD} and \mathbf{Y}_{DD} , respectively. (4.40) illustrates how the transmitted symbols vector at delay index $m - \hat{l}_i$ is influenced by the channel at the delay tap of \hat{l}_i . Since the channel applies varying effects on different delay paths of the transmitted signal in the delay-Doppler grid, the SNR of the received signal components of the transmitted symbol vectors \mathbf{x}_m at each delay tap $0 < m < M - 1$ differs. This forms the fundamental concept utilized in [158], [159] for detecting the transmitted symbols \mathbf{x}_m at the receiver. They do this by combining the received multipath components of the transmitted symbols using the Maximum-Ratio Combining (MRC) method.

4.7 Simulation Results

In this section, we present simulation results for the proposed correlation-based channel estimation method utilizing the CAZAC sequence. The channel model utilized is the TransPod high-Doppler channel, capable of reaching speeds up to 1000 km h^{-1} , as detailed in chapter 3. We assess the performance of our method in terms of channel estimation Normalized Mean Squared Error (NMSE) and Bit Error Rate (BER), and compare it with conventional estimation method employing a single impulse pilot [135], [136]. All relevant system parameters for simulation are outlined in Table 4.2.

For the conventional channel estimation method, we transmit an impulse pilot with a power level of $P_{\text{pilot}} = |x_p|^2$. The SNR of the pilot, denoted as $\text{SNR}_{\text{pilot}}$, is computed as the ratio of the squared magnitude of the pilot to the variance of the AWGN, $\text{SNR}_{\text{pilot}} = \frac{P_{\text{pilot}}}{\sigma_w^2}$. The SNR of the data is defined as $\text{SNR}_d = \frac{P_{\text{data}}}{\sigma_w^2} = \frac{\mathbb{E}\{|x_d|^2\}}{\sigma_w^2}$. Notably, the zero guard samples surrounding the pilot are influenced by noise due to the SNR_d associated with data transmission. We introduce the Power Difference Ratio (PDR), defined by the equation:

$$\text{PDR} = 10 \log_{10} \left(\frac{P_{\text{pilot}}}{P_{\text{data}}} \right) = 10 \log_{10} \left(\frac{|x_p|^2}{\mathbb{E}\{|x_d|^2\}} \right). \quad (4.41)$$

For the proposed sequence-based channel estimation method, we employ the CAZAC sequence \mathbf{X}_p with the same power level as one impulse pilot. To be fair, the power of one impulse pilot is distributed evenly across the CAZAC pilot sequence symbols such that $\mathbb{E}\{|\mathbf{X}_p|^2\} = |x_p|^2 = P_{\text{pilot}}$.

Table 4.2: System Parameters for Simulation

| simulation parameters | Value |
|--------------------------------|-------------------------|
| Carrier Frequency | 4 GHz |
| Modulation scheme | 4-QAM |
| Size of an OTFS frame (N, M) | (32, 128) |
| Subcarrier spacing | 30 kHz |
| Speed | 1000 km h ⁻¹ |
| Transmitter-Receiver distance | 30 m |

4.7.1 NMSE

We analyze the NMSE of the discrete delay-time channel response in (4.34). NMSE is an indicator for reflecting the channel estimation accuracy and is defined as:

$$\text{NMSE} = \frac{\left\| \mathbf{h}_{\text{td}}^s - \widehat{\mathbf{h}}_{\text{td}}^s \right\|_F^2}{\left\| \mathbf{h}_{\text{td}}^s \right\|_F^2}, \quad (4.42)$$

where $\|\cdot\|_F$ represents the Frobenius norm [160]. Here, \mathbf{h}_{td}^s and $\widehat{\mathbf{h}}_{\text{td}}^s$ are the vectors of the discrete delay-time channel and its estimate, respectively.

We evaluate the performance of the proposed correlation-based channel estimator in

comparison with the conventional method [35], [135] at PDR = 5 dB and 15 dB. We also compare the performance of the proposed channel estimation algorithm with the classic Linear Minimum Mean Square Error (LMMSE) channel estimation method for OTFS modulation, which minimizes the mean square error between the estimation region of the received signal in the delay-Doppler domain, and the the known impulse pilot. Mathematically, the LMMSE estimate of $\hat{\mathbf{H}}_{\text{LMMSE}}$ is derived as:

$$\hat{\mathbf{H}}_{\text{LMMSE}} = \frac{\mathbf{y} * x_p^*}{|x_p|^2 + \sigma_w^2}. \quad (4.43)$$

Then, from the estimated channel response $\hat{\mathbf{H}}_{\text{LMMSE}}$, the channel parameters can be estimated [161].

Figure 4.20 illustrates the comparison of NMSE performance between different methods. We observe that the proposed method shows more resistance to the noise due to exploiting the whole zero padded space instead of just using one bin to place the pilot. The obtained "diversity gain" helps to reduce the false path detection probability and also to increase the probability of path detection.

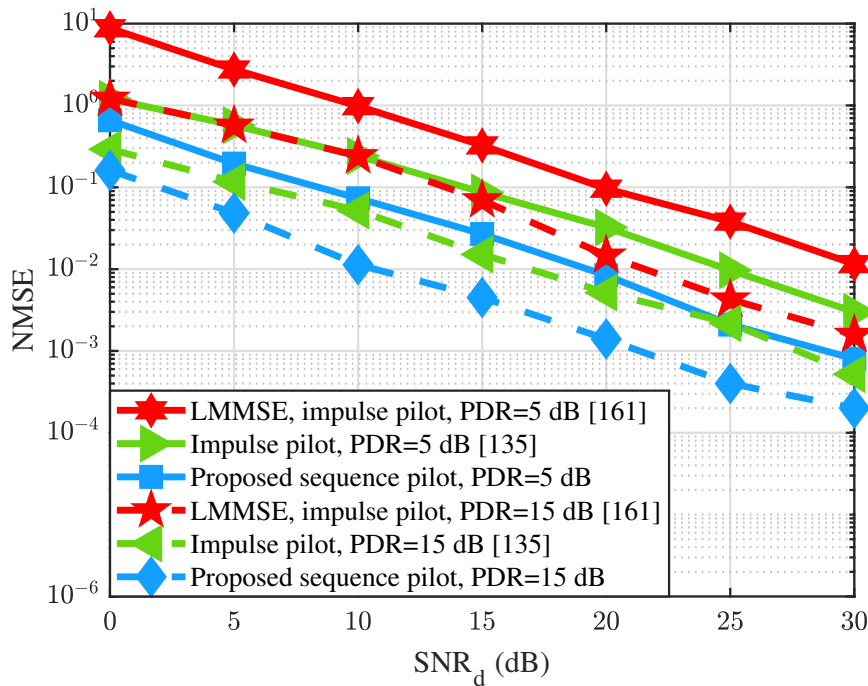


Figure 4.20: NMSE performance between proposed sequence pilot structure and conventional method with impulse pilot for different PDRs.

The NMSE vs PDR performances of the proposed algorithm and the conventional method in [135], for three different data SNR (5, 10, and 15 dB) is shown in Figure 4.21. Comparing the curves shows that, with a fixed power budget for the pilot, the proposed method achieves NMSE reduction. The Figure 4.22, depicts the same curves, with horizontal markers, that gives the reduction that we obtain in pilot power, for the same NMSE performance. Hence, apart from power saving, and as a good consequence, the PAPR of the time domain signal utilizing the proposed pilot sequence is reduced compared to the conventional pilot scheme.

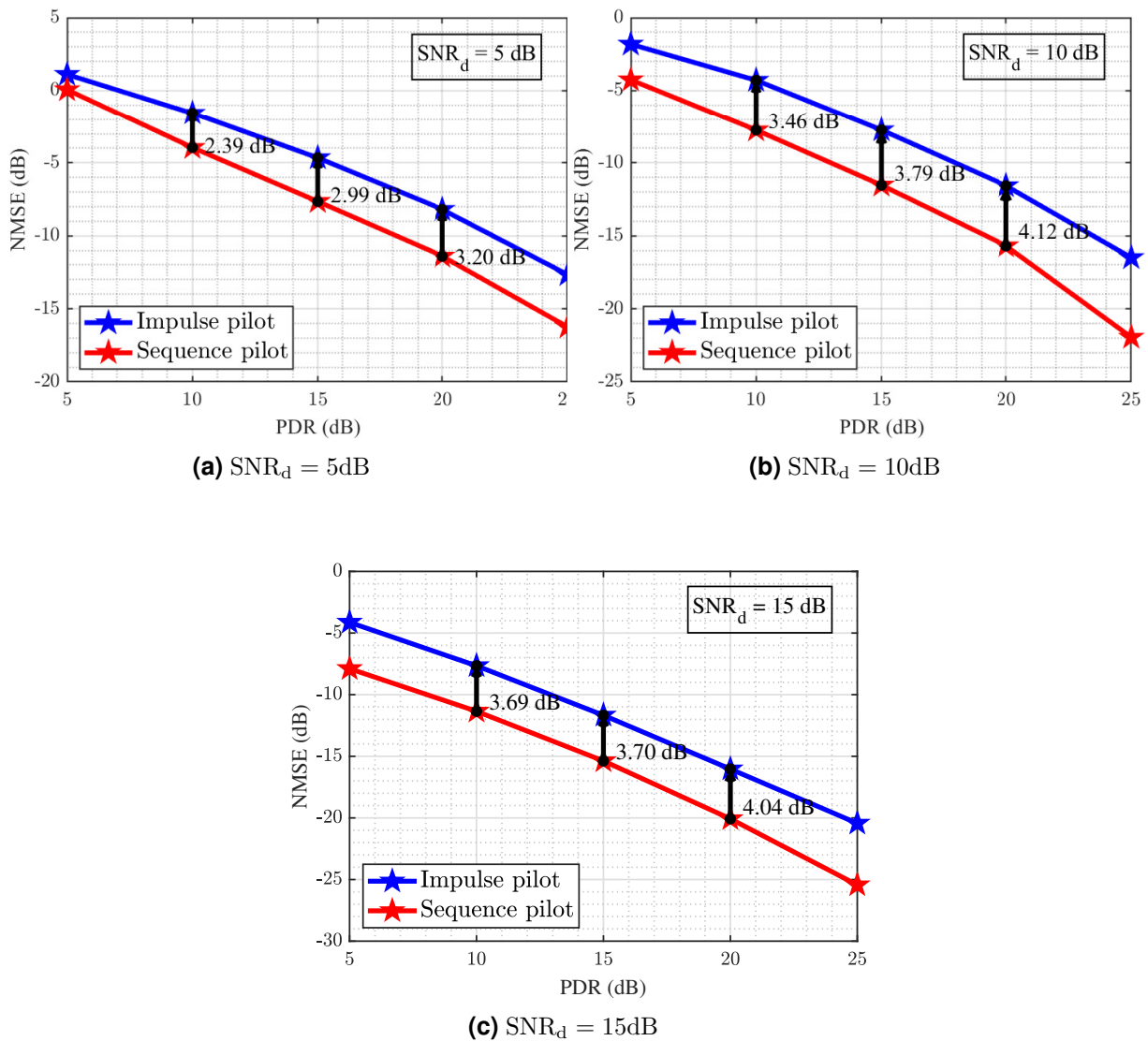


Figure 4.21: NMSE performance comparison of proposed sequence pilot structure and conventional impulse pilot as a function of pilot power, for different SNR_d .

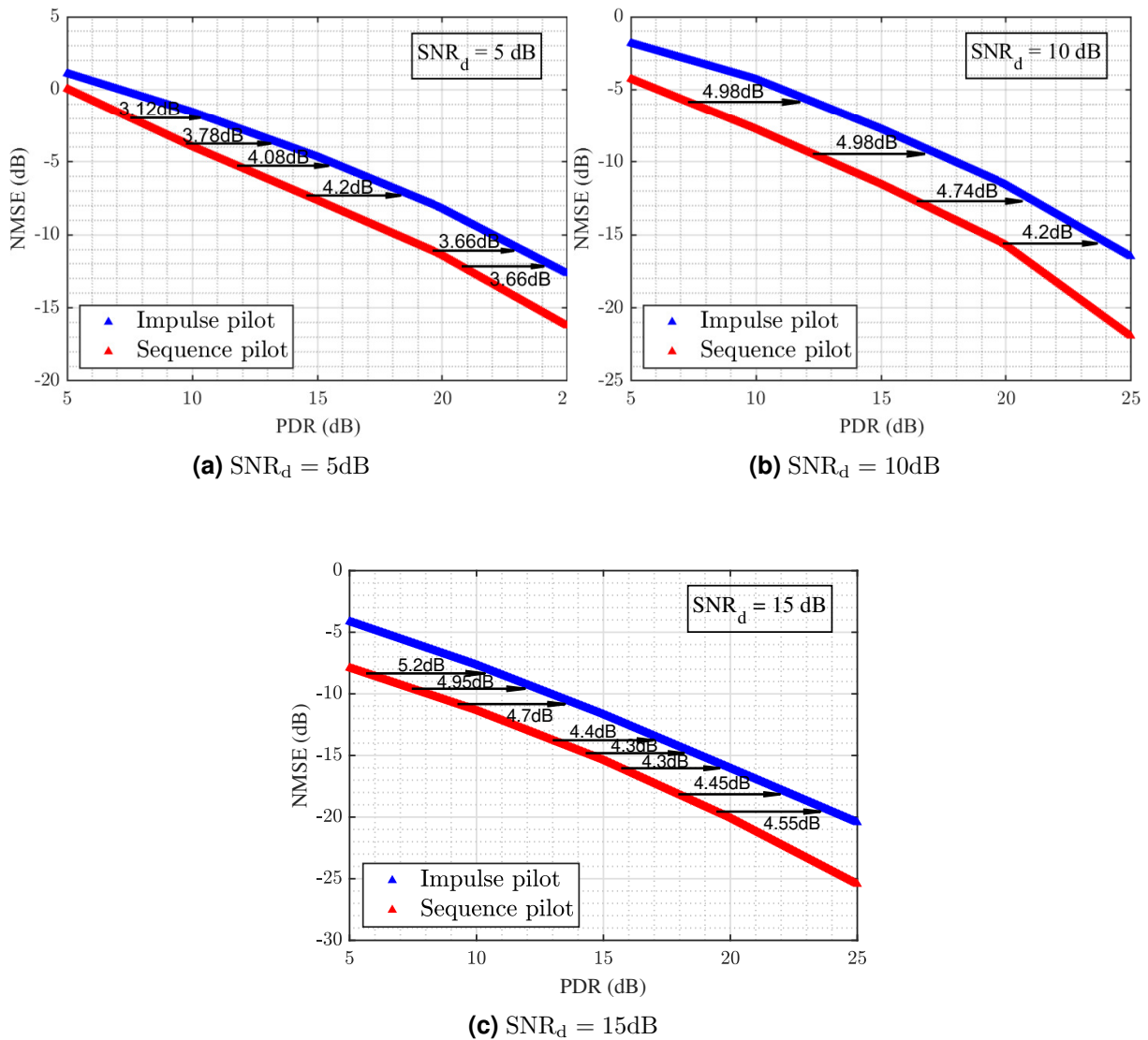


Figure 4.22: NMSE performance comparison of proposed sequence pilot structure and conventional impulse pilot as a function of pilot power, for different SNR_d .

4.7.2 BER

Figure 4.23 illustrates the BER comparison of the channel estimation methods with impulse pilot for $PDR = 5\text{ dB}$, 15 dB , and sequence pilot, where the case of known channel is also presented for reference. The results reflect the difference in channel estimation performance between the traditional and proposed method. In low pilot power, the traditional method exhibits the worst BER due to its inferior channel estimation

performance. The proposed method gives better BER performance because of its "diversity gain".

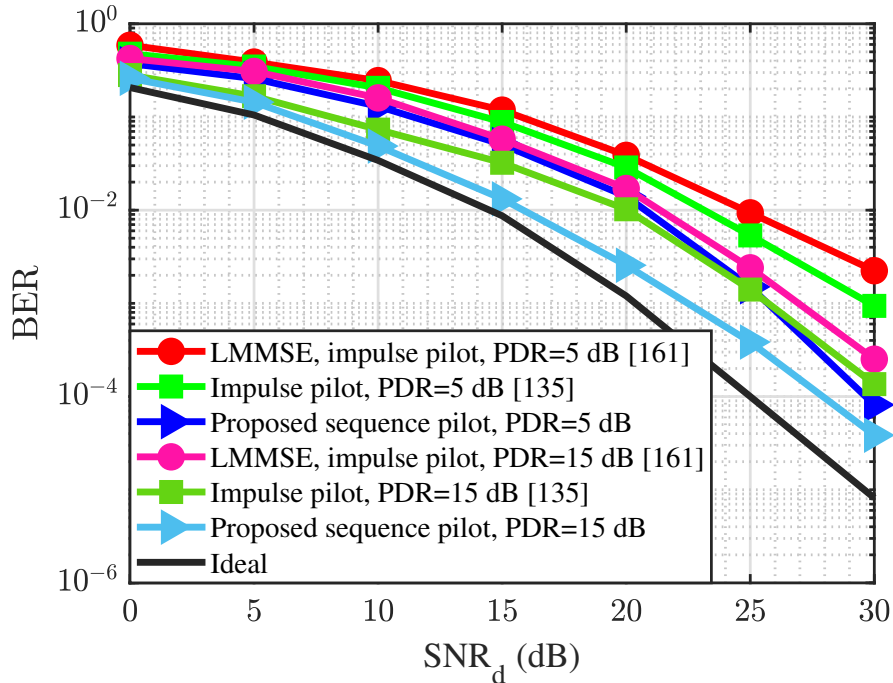


Figure 4.23: BER performance of the proposed sequence pilot and conventional impulse pilot channel estimation under different PDR.

4.8 Summary

This chapter introduces a novel pilot-based channel estimation technique for OTFS modulation systems. It involves inserting a pilot sequence into the zero bins of the ZP-OTFS system to improve the estimation accuracy, particularly in high noise scenarios. Multiple pilot symbols are utilized to provide redundancy, facilitating noise mitigation through averaging. Our proposed correlation-based estimation algorithm utilizes CAZAC sequence for robust parameter estimation. Additionally, the proposed method achieves the same level of channel estimation accuracy while using less pilot power resource, leading to a lower PAPR of the corresponding time domain signal. Therefore, although distributing the pilot symbols along the Doppler axis does not directly alter the PAPR, we can achieve an indirect reduction in PAPR thanks to pilot power reduction.

5

Deep Learning Based Channel Estimation in ZP-OTFS Modulation Systems

Sommaire

| | | |
|-------|--|-----|
| 5.1 | Related works | 136 |
| 5.2 | Motivation | 137 |
| 5.2.1 | Background on neural network | 138 |
| 5.2.2 | Dataset Management: Train, Validation, and Test Sets | 141 |
| 5.2.3 | System Model and Data arrangement | 141 |
| 5.2.4 | Proposed DNN structure | 143 |
| 5.3 | Discussions and Simulation analysis | 145 |
| 5.3.1 | Impact of pilot power | 146 |
| 5.3.2 | DNN Architecture | 150 |
| 5.3.3 | Impact of Tx-Rx distances | 152 |
| 5.3.4 | Impact of SNR on the trained DNN model | 154 |
| 5.3.5 | Computational Complexity | 155 |
| 5.4 | Summary | 155 |

THE main objective of this chapter is to propose a DNN-based channel estimation method for OTFS systems. Traditional estimation methods often struggle with fractional normalized Doppler indices, leading to inaccuracies due to the pilot symbol leakage effect. By applying the DNN approach, we aim to overcome this challenge and increase the accuracy of the channel estimation. We will evaluate this method through detailed simulations.

5.1 Related works

In recent years, DL, a subset of machine learning, has gained considerable attraction and demonstrated its efficacy across various domains, including the design of wireless communication systems [162], [163]. Within this context, DNNs offer promising solutions for various tasks such as channel estimation [164], [165], modulation recognition [166], and detection [167]. Given the advantages offered by OTFS, DL techniques have been employed in addressing various challenges within OTFS systems, including detection and channel estimation. In the investigation conducted by [168], pilot symbols were interleaved with data symbols, leading to interference between them at the receiver. To address this issue, the authors utilized Recurrent Neural Network (RNN) with Long Short-Term Memory (LSTM) layers. This choice was motivated by the feedback loop established in the system, after mitigating the interference effects from the data, the output of the OTFS detector is fed back to the input of the network. This feedback loop creates a dependency between the current input and previous inputs of the network,

making RNN the appropriate choice for the task. In [169], the authors propose to use 2D-ConvLSTM to predict future channel coefficients directly from the previous OTFS frames on a vehicle trajectory. In [170], a DNN-based architecture utilizing one impulse pilot is proposed to carry out fractional Doppler channel estimation in OTFS systems.

In this chapter, we begin by our motivation focusing on the fractional Doppler shifts, then we provide background information on deep learning. We then detail the architecture of the DNN used in this study and describe the input data structure of the DNN estimator, along with the generation of datasets required for training and testing phases. Finally, we conclude by identifying the optimal architecture for our specific case study, comparing simulation results with those obtained from conventional methods.

5.2 Motivation

Traditional channel estimation techniques, while effective in some scenarios, face significant challenges, including sensitivity to noise and the need for high pilot power. Moreover, these methods often struggle with fractional normalized Doppler indices, leading to inaccuracy due to the pilot symbol leakage effect (see Figure 4.10). This is where Deep Learning (DL) methods can play an efficient role. DL algorithms, with their ability to learn complex patterns and generalize from large datasets, can offer robustness against noise and fractional Doppler shifts in the channel, potentially improving channel estimation accuracy in OTFS system.

As previously discussed, the actual Doppler shift values ν can be computed as $\nu = \frac{\kappa}{NT}$, where κ is the Doppler index and NT is the OTFS frame size. For small OTFS frame duration and small N , κ becomes fractional and can not be accurately estimated at the receiver. Instead, multiple paths with integer Doppler indices k adjacent to the fractional value κ are estimated with an error of k^e , such that $\kappa = k + k^e$. This results in a phase rotation of $z^{k^e(m-l)}$ in the delay-Doppler received signal.

Revisiting Equation 4.39 from chapter 4 with fractional Doppler indices κ_i , the delay-time domain signal in vectorized form is expressed as:

$$\tilde{\mathbf{y}}_m(n) = \sum_{i=1}^{\hat{P}} \hat{h}_i z^{(\hat{k}_i - k_i^e)(m - \hat{l}_i)} e^{\frac{2j\pi(\hat{k}_i - k_i^e)n}{N}} \tilde{\mathbf{x}}_{m - \hat{l}_i}(n). \quad (5.1)$$

Similar to Equation 4.40, the above equation can be converted to delay-Doppler domain as:

$$\begin{aligned} \mathbf{y}_m &= \mathbf{F}_N \cdot \tilde{\mathbf{y}}_m = \frac{1}{N} \sum_{n=0}^{N-1} \sum_{i=1}^{\hat{P}} \hat{h}_i z^{(\hat{k}_i - k_i^e)(m - \hat{l}_i)} e^{\frac{2j\pi(\hat{k}_i - k_i^e)n}{N}} e^{-\frac{j2\pi kn}{N}} \tilde{\mathbf{x}}_{m - \hat{l}_i}(n) \\ &= \frac{1}{N} \sum_{i=1}^{\hat{P}} \hat{h}_i z^{(\hat{k}_i - k_i^e)(m - \hat{l}_i)} \left(\frac{e^{j2\pi((\hat{k}_i - k_i^e) - k)} - 1}{e^{\frac{j2\pi((\hat{k}_i - k_i^e) - k)}{N}} - 1} \right) \tilde{\mathbf{x}}_{m - \hat{l}_i}(n) \\ &= \frac{1}{N} \sum_{i=1}^{\hat{P}} \hat{h}_i z^{(\hat{k}_i - k_i^e)(m - \hat{l}_i)} \Psi \tilde{\mathbf{x}}_{m - \hat{l}_i}(n), \end{aligned} \quad (5.2)$$

here, the term Ψ represents the effect of fractional Doppler on the received signal.

5.2.1 Background on neural network

An Artificial Neural Network (ANN) or DL, a widely used machine learning algorithm, is structured similarly to the human neural system. The network learns to perform classification or regression tasks directly from input data such as images, text, or sound. It comprises basic computational units known as neurons, which are organized into layers within the network. Typically, an ANN consists of three primary layers: the input layer, the output layer, and at least one hidden layer in between. Each neuron receives inputs, denoted as $x = [x_1, x_2, \dots, x_n]$, either from the input layer or from neurons in other hidden layers [171]–[174]. These inputs are modified by corresponding weights, $w = [w_1, w_2, \dots, w_n]$. The neuron calculates the weighted sum of these inputs and adds a bias b to obtain the output z . Then a nonlinear function f , known as an activation function, is applied to z to determine the output of the neuron n :

$$n = f(z) = f\left(\sum_{j=1}^N x_j w_j + b\right) \quad (5.3)$$

This process is depicted in Figure 5.1, which illustrates the structure of a neuron in the neural network [175].

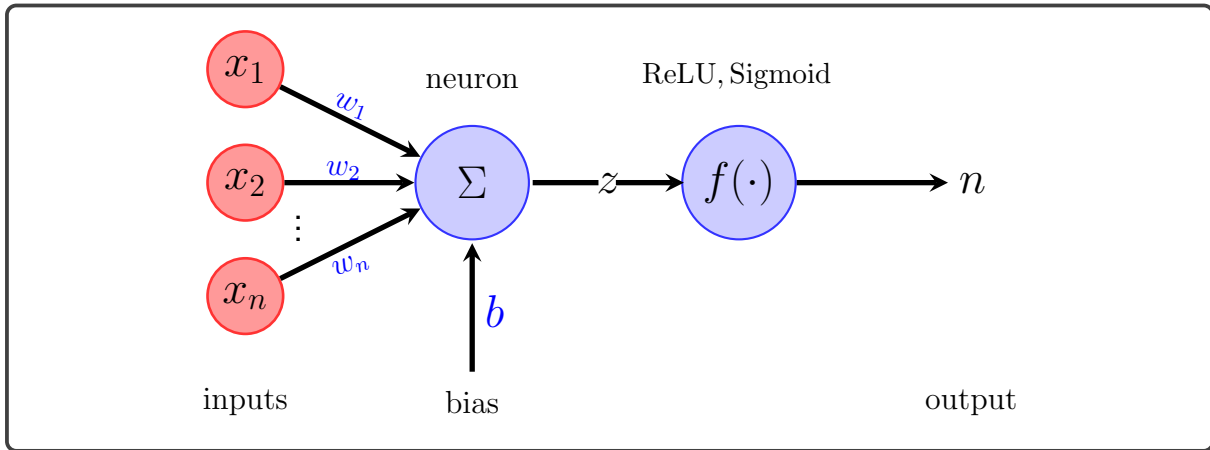


Figure 5.1: Neuron architecture with n input values.

An activation function is a mathematical operation that transforms the input of a neuron into an output to be passed to the next layers. They introduce non-linearity into the output of the neuron, allowing the network to learn more complex relationships between the inputs and outputs. There are various types of activation functions, each with its unique characteristics and applications. The activation function Rectified Linear Unit (ReLU) is the most popular due to its ability to avoid the vanishing gradient problem, and defined as:

$$f(x) = \max(0, x) \quad (5.4)$$

In the output layer, a different activation function might be used depending on whether the problem at hand is a regression or classification. For classification, the sigmoid activation function is generally considered:

$$f(x) = \frac{1}{1 + e^{-x}}, \quad (5.5)$$

and for regression problem, the linear activation function or identity function is used directly in the output layer:

$$f(x) = x. \quad (5.6)$$

As input data progresses through the network, each neuron computes its output, which is then passed on to the next layer. This process continues iteratively until reaching the output layer. Once the network produces its predicted output \hat{y} , it is compared against the expected output y , often referred to as the ground truth or target obtained from

training data, to compute the error. The deviation between expected and predicted outputs is quantified through a cost function, with Mean Squared Error (MSE) being one of the most commonly used loss functions:

$$L = \frac{1}{N} \sum_{i=1}^N (y_i - \hat{y}_i)^2. \quad (5.7)$$

During the training stage, the network is trained to adjust its internal parameters, such as weights and biases, via the back-propagation method. This process involves calculating the gradient of the error with respect to each weight, $\frac{\partial L}{\partial w}$ and bias, $\frac{\partial L}{\partial b}$. The gradient tells us the direction in which the weights and biases need to be adjusted to minimize the MSE. These modifications are made iteratively over numerous epochs, or complete passes through the training dataset. By updating the weights and biases, the network improves its ability to accurately map the input data to the correct outputs, thereby reducing the loss over time [176].

Neural networks can be broadly classified into two main categories: feed-forward and feedback (or recurrent) networks. Within these categories, there are several types of networks with different architectures tailored to specific applications.

1. **Feed-forward neural network (FNN)** : They are characterized by data moving one way from the input nodes, through any hidden layers, to the output nodes without any cycle or loop. This category includes both DNN and Convolutional Neural Network (CNN):

- **DNN** : These networks consist of an input layer, two or more hidden layers (hence "deep"), and an output layer. The layers are typically fully connected, meaning that every neuron in the layer is connected to all neurons in the previous layer. DNNs are used for tasks like object detection, facial recognition, and image classification [177], [178].
- **CNN** These are designed for processing two-dimensional grid data, such as images and videos. CNNs use convolutional layers, pooling layers, and fully connected layers [179], [180].

2. **Feedback neural network** They differ from feed-forward networks in that they

allow data to flow in loops. This means they can maintain state or memory over time that captures information about past inputs, making them suitable for tasks involving sequential data like time series prediction, natural language processing, and speech recognition [181], [182]. This category also includes gated recurrent units (GRUs) and long short-term memory (LSTM) approaches. LSTM network has the ability to predict the future data based on the previous observations [183].

In this work, we utilized DNN based channel estimation method.

5.2.2 Dataset Management: Train, Validation, and Test Sets

In neural networks, datasets are typically divided into three subsets: training, testing, and validation. The training set is used to train the model, allowing it to learn and adapt its weights based on the provided inputs and expected outputs. Commonly, around 70% to 80% of the data is allocated for training. The validation set, which often comprises about 10% to 20% of the train data, is used to validate the model performance during training. The model is trained on the training set, and, simultaneously, the model evaluation is performed on the validation set after every epoch to tune the model parameters. For example, in the classification tasks, the training data set is used to train the different candidate classifiers, the validation data set is used to compare the different candidate classifiers in terms of their performances and decide which one to take. Lastly, the test set is independent of the training data set and used to evaluate the performance of the model after training has concluded [184]–[187].

5.2.3 System Model and Data arrangement

As discussed previously, in this study, we utilize the ZP-OTFS structure, where the final L_{ZP} rows of the delay-Doppler grid are set to zeros, while the remaining $M - L_{ZP}$ rows contain the information symbols. The length of zero padding, L_{ZP} , is determined as $(2l_{\max} + 1)$, where l_{\max} represents the length of the channel impulse response. Within this zero-padded region, the pilot sequence is positioned at the delay index m_p across all Doppler bins. The insertion of zero padding helps mitigate inter-block interference in the time domain as well as interference between data and pilot symbols. Together with the data symbols $x_d[m, n]$, these elements constitute the transmission frame of

ZP-OTFS, depicted in Figure 5.2:

$$X_{DD}[m, n] = \begin{cases} x_p[n] & m = m_p, \quad n \in [0, N - 1] \\ 0 & \begin{cases} m \in [m_p - l_{\max}, m_p) \cup (m_p, M - 1] \\ n \in [0, N - 1] \end{cases} \\ x_d[m, n] & \text{otherwise.} \end{cases} \quad (5.8)$$

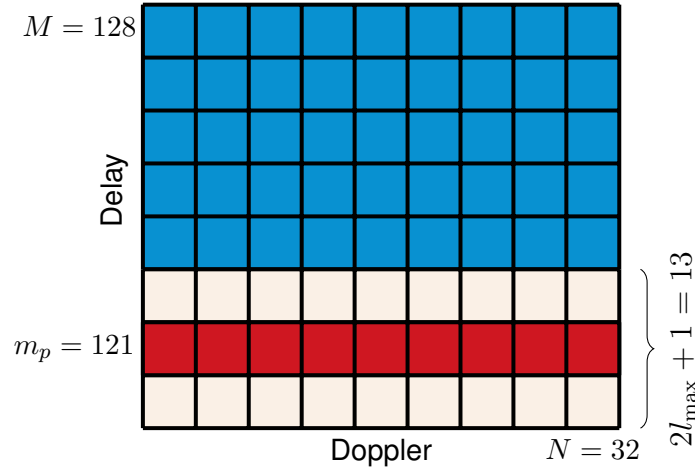


Figure 5.2: delay-Doppler grid structure with pilot sequence for CP-OTFS and ZP-OTFS; ■: data, ■: guard, and ■: pilot sequence.

To estimate the channel, we analyze symbols of the received signal in the delay-Doppler domain corresponding to both pilot symbols and zero guard bins. Circular shifted versions of the pilot sequence are copied at the delay taps of the channel, with each version multiplied by the complex-valued channel coefficient of the respective path. These symbols are structured into a complex-valued matrix denoted as $\mathbf{E} \in \mathbb{C}^{N \times (l_{\max} + 1)}$, spanning from m_p to $m_p + l_{\max}$ in the delay axis and from 0 to $N - 1$ in the Doppler axis:

$$\mathbf{E} = \mathbf{Y}[m_p : M - 1, :], \quad (5.9)$$

where \mathbf{Y} is the received signal in the delay-Doppler domain. This matrix serves as the input data for the deep neural network tasked with learning the channel characteristics. The goal is to reconstruct the channel parameters (h_i, l_i, k_i) for each detected path, which will serve as the expected output at the final layer of the network.

5.2.4 Proposed DNN structure

The DNN architecture includes three primary components: an input layer, D hidden layers, and an output layer, as illustrated in Figure 5.3. We extract $2N(l_{\max} + 1)$ symbols from the matrix \mathbf{E} from (5.9), corresponding to the transmitted pilot sequence, from the received OTFS frame. Then it transforms into vector $\mathbf{e} \in \mathbb{R}^{2N(l_{\max}+1) \times 1}$. Since the DNN processes only real values, this vector \mathbf{e} is divided into its real and imaginary parts, resulting in an input layer with $2N(l_{\max} + 1)$ neurons. The expected data for training the network is obtained by generating a $3l_{\max}$ length vector of true channel parameters $\mathbf{u} = (h_i, l_i, k_i)$, where i corresponds to each identified channel path. Since the channel coefficients are complex, their real and imaginary parts are processed separately, resulting in the output vector $\mathbf{u} \in \mathbb{R}^{4l_{\max} \times 1}$. At the core of the DNN are its hidden layers, each composed of J neurons. These neurons perform nonlinear function on the inputs they receive, which are the weighted sums from the previous layer's outputs. The activation function f_1 used for hidden layers is the ReLU function, while a linear activation function f_2 is used for the output layer. The output of the network during the forward propagation process, denoted as $\hat{\mathbf{u}}$, results from multiple sequential nonlinear transformations. In this context, the output of each hidden layer $\mathbf{n}^d \in \mathbb{R}^{J \times 1}$ serves as the input to the next layer, with \mathbf{n}^d being the output from layer d , and $\hat{\mathbf{u}} \in \mathbb{R}^{4l_{\max} \times 1}$ representing the final predicted output. The weights of each layer are stored in matrix $\mathbf{W}^d \in \mathbb{R}^{J \times J}$ for $d = 2, \dots, D$, $\mathbf{W}^1 \in \mathbb{R}^{2N(l_{\max}+1) \times J}$, and $\mathbf{W}^{D+1} \in \mathbb{R}^{J \times 4l_{\max}}$. Furthermore, each layer also has a bias vector $\mathbf{b}^d \in \mathbb{R}^{J \times 1}$. The transformations from the input to the first hidden layer and from the last hidden layer to the output are formulated as follows:

$$\mathbf{n}^1 = f_1 (\mathbf{W}^1 \mathbf{e} + \mathbf{b}^1), \quad (5.10)$$

$$\hat{\mathbf{u}} = f_2 (\mathbf{W}^{D+1} \mathbf{n}^D + \mathbf{b}^{D+1}). \quad (5.11)$$

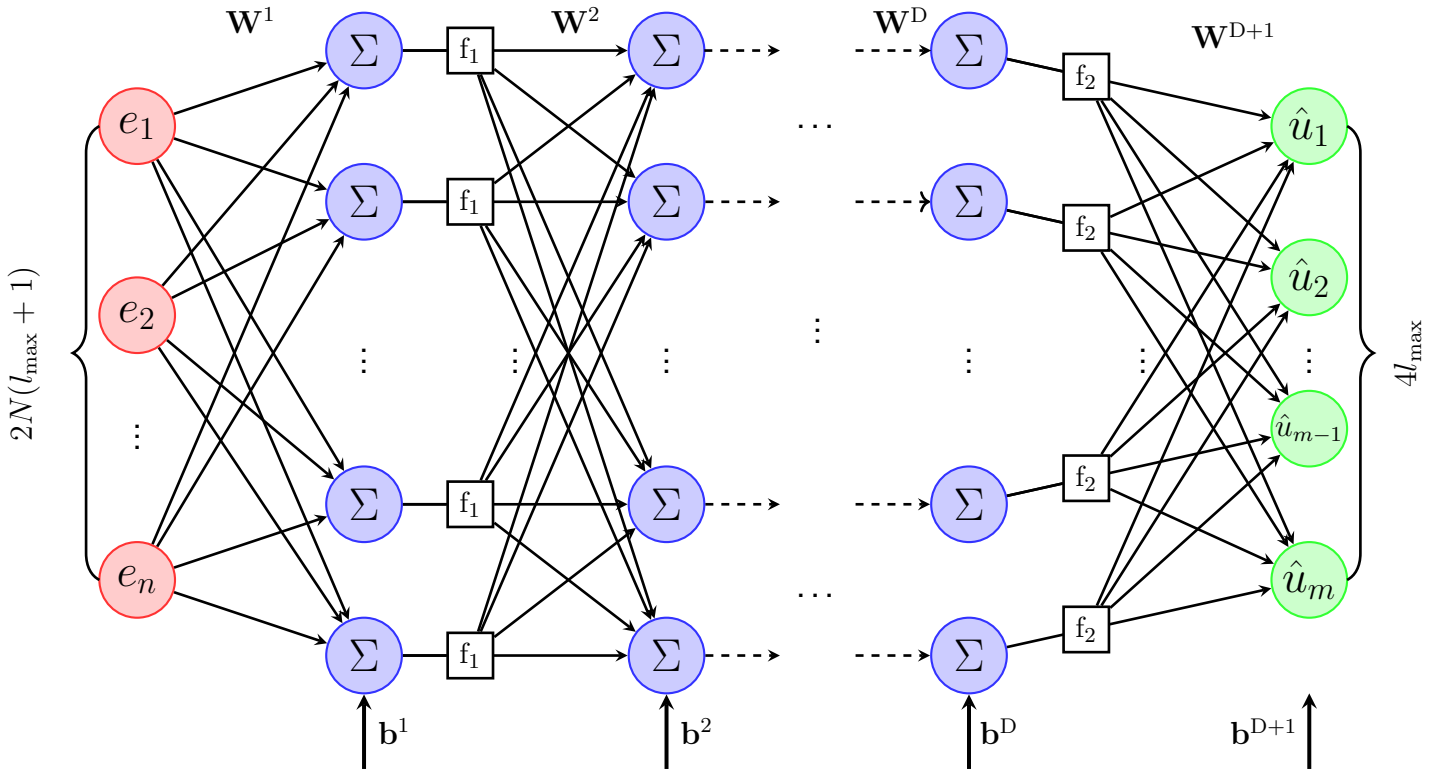


Figure 5.3: A fully connected neural network (FNN); ■: Inputs, ■: Neurons, and ■: Outputs

The network is trained offline using training data generated from a large number of delay-Doppler domain OTFS frames using various pilot schemes. The objective is to design an appropriate DNN architecture that can learn the relationship between the target data \mathbf{u} and the input \mathbf{E} as a function $F : \mathbf{E} \rightarrow \mathbf{u}$, to predict the output vector as a regression problem. During the training phase, the weights and biases are adjusted through the back-propagation by Adam optimizer, to minimize the error between the actual output \mathbf{U} and the predicted output $\hat{\mathbf{u}}$. The Mean Square Error (MSE) is employed as the loss function to quantitatively measure the difference between the predicted and actual channel parameters:

$$L(\mathbf{u}, \hat{\mathbf{u}}) = \|\mathbf{u} - \hat{\mathbf{u}}\|^2$$

The training process, involving both forward and backward propagation, is repeated until the network reaches a satisfactory level of accuracy.

To improve the accuracy of the network, the training set is generated under a variety of channel conditions, including different channel gains and SNRs.

5.3 Discussions and Simulation analysis

Our simulations apply the TransPod channel model introduced in chapter 2. To generate the dataset, we evaluate D distinct distances between the transmitter and receiver in the TransPod context. At each distance, we generate a dataset across a range of SNRs from 0 dB to 30 dB. For each distance and SNR for speed v of the FluxJet vehicle, we generate L_r realizations of the communication channel. These realizations have the same values of delay τ_i and Doppler ν_i , but differ in their channel coefficients h_i . To diversify our dataset, we further generate L_s sequences for each L_r realization by introducing random noise \mathbf{n} at a constant SNR to the actual signal, in (4.6).

Table 5.1: Parameters of DNN architecture.

| Parameter | Value |
|----------------------------|--------------------|
| Input layer neurons | $2N(l_{\max} + 1)$ |
| Hidden layer numbers | 2 |
| Output layer neurons | $4l_{\max}$ |
| Hidden layers neurons | 20 |
| Size of the training set | 28000 |
| Size of the validation set | 7000 |
| Size of the testing set | 15000 |
| Hidden layers activation | ReLU |
| Output layer activation | Linear |
| Optimizer | Adam |
| Epochs | 100 |
| Batch size | 128 |
| Learning rate | 0.001 |

We present a comprehensive analysis of our simulations using distinct subsections. In each subsection, we explore a specific performance aspect of our proposed DNN-based channel estimator. Our goal is to enhance training efficiency while avoiding excessive

resource consumption and the necessity for an individual network for each pair of SNR and distance. Thus, we adapt our dataset to train the network in alignment with the specifications outlined in the subsequent subsections. In one subset of experiments, we maintain a fixed distance between the transmitter and the receiver while training the DNN network across a range of SNR_d from 0 dB to 30 dB. Another subset of experiments involves keeping the SNR_d fixed, set at 15 dB and 30 dB, and vary the distances during training. We utilize a delay-Doppler grid with $M = 128$ delay bins and $N = 32$ Doppler bins, employing a subcarrier spacing of $\Delta f = 1000$ kHz. For the pilot sequence, we employ a CAZAC sequence of length N defined in (4.25). The sequence is designed to have the same total power as the impulse pilot, ensuring a fair comparison. The maximum delay index is set to $l_{\max} = 6$. In each scenario, we populate the corresponding values of delay, Doppler and channel coefficients, while setting all others to zero. Consequently, the input layer of the DNN consists of $2N(l_{\max} + 1) = 448$ neurons, and the output layer consists of $4l_{\max} = 24$ neurons. We generate a dataset consisting of $L_r = 50$ channel realizations for each distance, and each realization is generated $L_s = 1000$ times. To validate the effectiveness of our DNN, we split our dataset into 70% and 30% for training and testing, respectively. Within the training dataset, we further divide 80% for actual training and 20% for validation. We evaluate the prediction accuracy of our DNN by measuring the NMSE. As a result, we generate 50000 training samples and we set 28000 as the offline training dataset, 7000 as validation dataset, and 15000 for the test dataset. The DNN training and testing are conducted using the PyTorch framework. The robustness of the proposed DNN-based channel estimator is tested using PDR=5 dB and PDR=15 dB, reflecting both low and high pilot power compared to the data. Moreover, we investigate the impact of different DNN architectures to determine the optimum number of layers for improved channel estimation performance. Therefore, identifying the best DNN architecture that achieves good performance-complexity trade-off for the TransPod system. All the basic parameters of the architecture of the DNN is summarized in [Table 5.1](#).

5.3.1 Impact of pilot power

In this analysis, we fix the distance between transmitter and receiver to 30 m, and evaluate the performance of the proposed channel estimator with PDR=5 dB and

PDR=15 dB.

Figure 5.4 illustrates a comparison of NMSE performance between the conventional channel estimation method in [135] and the DNN-based method when utilizing one impulse pilot [170]. In Figure 5.5, we demonstrate NMSE comparison between correlation-based method as seen in chapter 4 [23], and the DNN-based method, while utilizing a CAZAC sequence pilot. The results demonstrate that, when the pilot power is not significantly higher than the data power, there is a risk of false detection of delay and Doppler taps, resulting in a significant error in channel estimation. Results further show that, the proposed DNN-based channel estimator outperforms its conventional counterparts. The DNN-based method, employing sequence pilot symbols, demonstrates superior performance compared to other curves. In fact, the diversity provided by multiple pilots improves the robustness, making the system more resilient to noise and interference. To achieve the same estimation performance, our architecture requires less pilot power, which results in a lower PAPR. Figure 5.6 and Figure 5.7 illustrate a comparison of the BER performance using the MRC detector. We observe that the conventional method employing a single impulse pilot or a sequence pilot, exhibits improved performance as the pilot power increases. These results also highlight the superior performance of the DNN approach compared to traditional approaches.

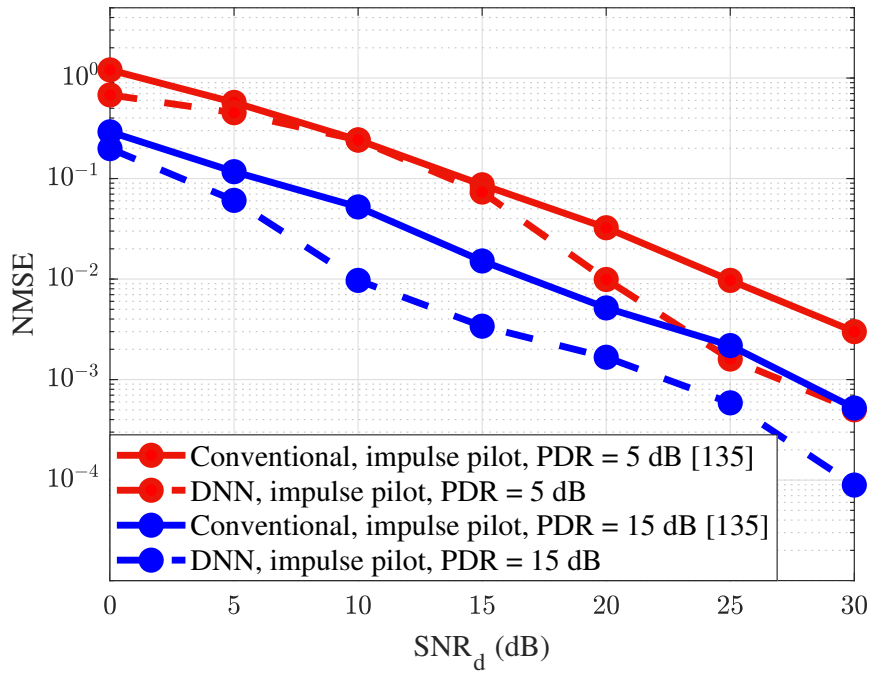


Figure 5.4: NMSE performance comparison between the proposed DNN approach and conventional scheme with an impulse pilot.

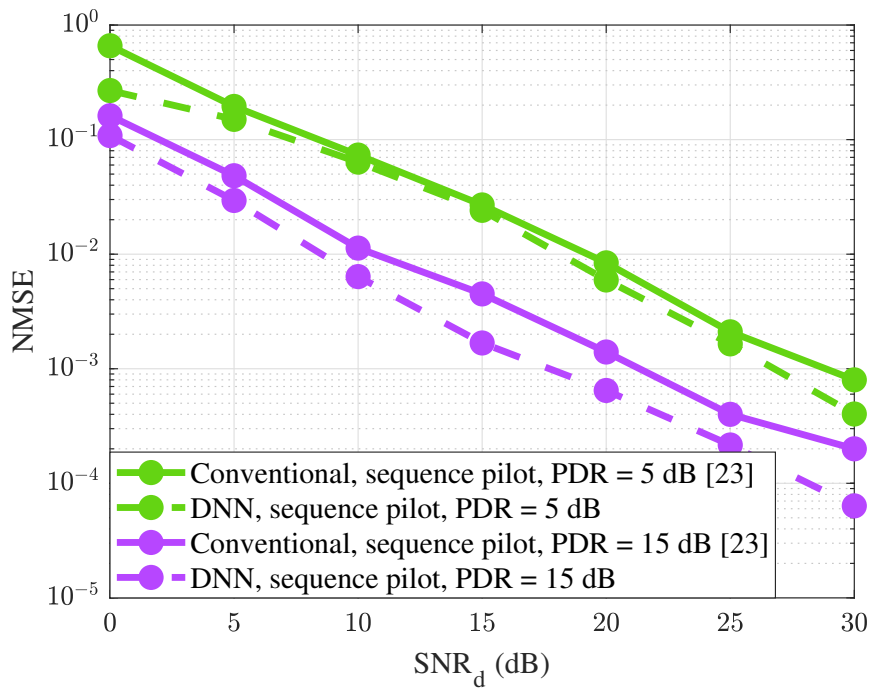


Figure 5.5: NMSE performance comparison between the proposed DNN approach and conventional scheme with a sequence pilot.

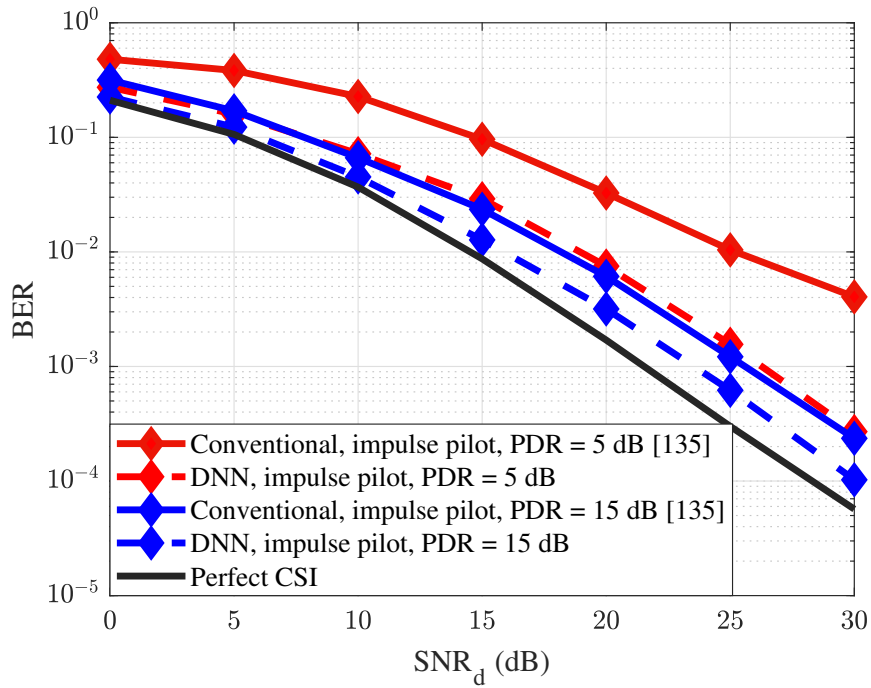


Figure 5.6: BER performance comparison between the proposed DNN approach and conventional scheme with an impulse pilot.

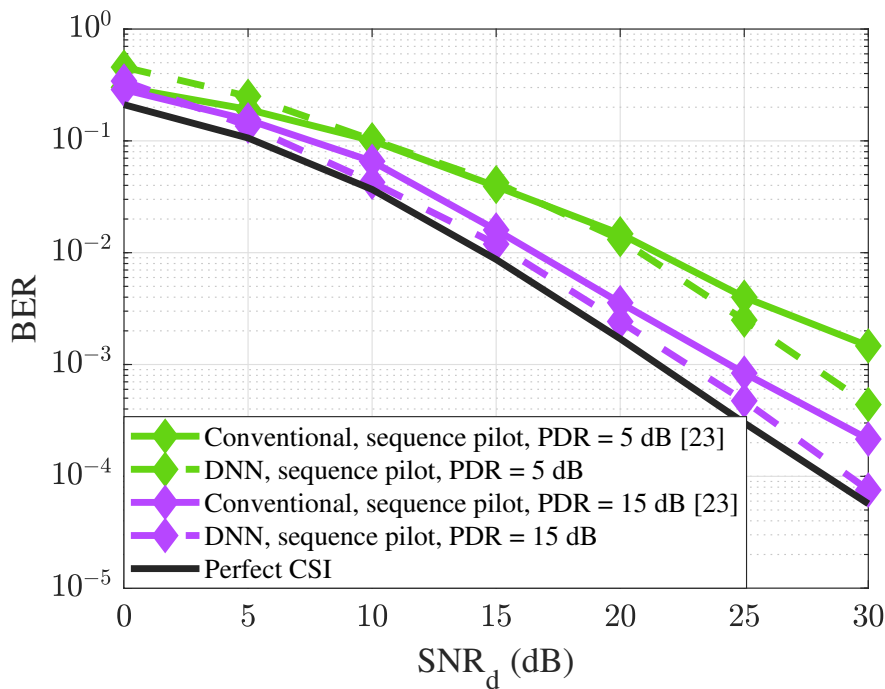


Figure 5.7: BER performance comparison between the proposed DNN approach and conventional scheme with a sequence pilot.

5.3.2 DNN Architecture

In this section, our primary aim is to assess the performance of the implemented DNN architecture and to explore the impact of varying the number of layers and neurons within the network. [Figure 5.8](#) presents the results of our NMSE evaluation for estimator utilizing CAZAC sequence. It was found that a two-layer network exhibited the most promising overall performance. Interestingly, our observations suggest that increasing the depth of the network does not necessarily lead to enhanced performance. This phenomenon can be explained by the fact that deeper networks demand more extensive datasets and computational resources for effective training. When the dataset is limited in size or lacks sufficient information to justify deeper representations, the addition of more layers may even result in performance degradation.

Subsequently, focusing on a two-layer architecture, we investigated the influence of varying the number of neurons, ranging from 5 to 40 neurons per layer, as illustrated in [Figure 5.9](#). The analysis indicates that increasing the number of neurons improves NMSE performance. However, finding the right balance is a key. If the model gets too complex, it needs more computing power. But if it is too simple, it might not give an accurate channel estimation. Through our analysis, we determined that employing 20 neurons per layer achieved a favorable balance between performance and computational complexity.

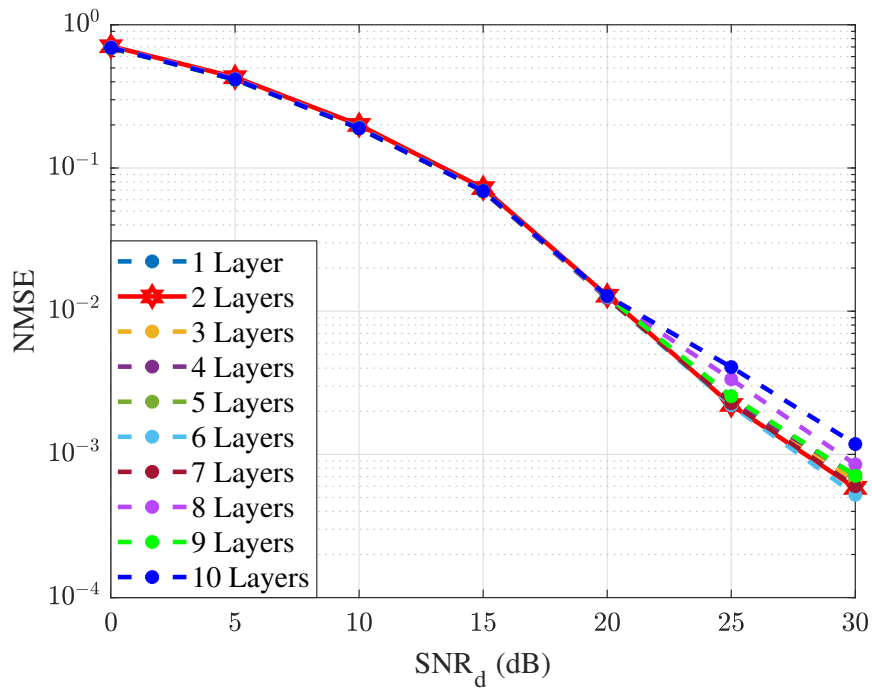


Figure 5.8: NMSE performance of the trained DNN model using different architectures.

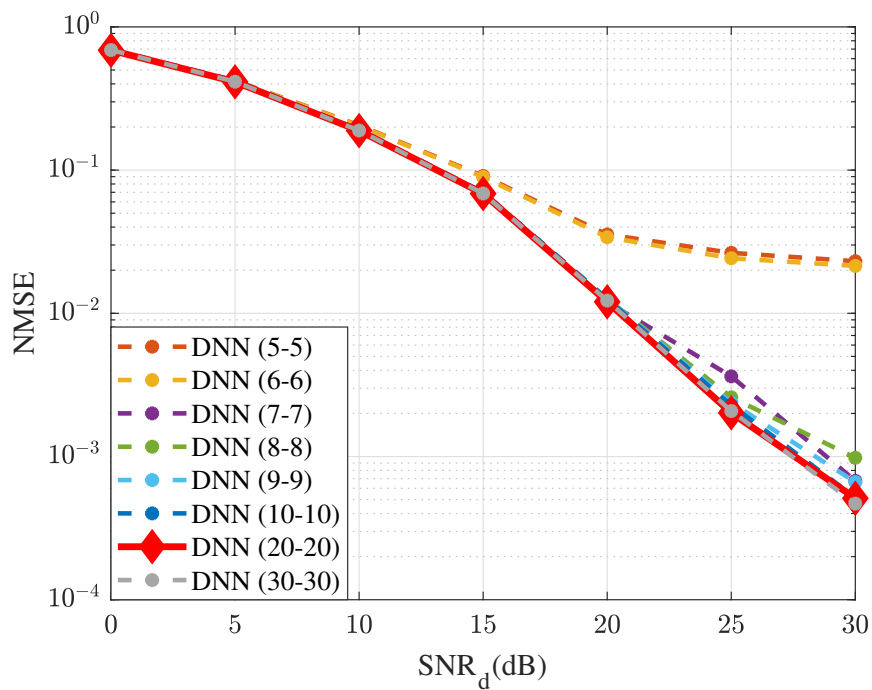


Figure 5.9: BER performance comparison between the different DNN architectures.

5.3.3 Impact of Tx-Rx distances

In this section, our objective is to analyze the impact of the distance between transmitter and receiver. In order to do so, we maintain SNR_d of 15 dB and 30 dB while training the network. We generate data from 10 different distances: [10, 40, 70, 100, 200, 300, 400, 500, 600, 700] meters. The results show that the minimal error is observed when the network is both trained and tested at the same distance. As a consequence, the DNN parameters should be adapted with the distance. Actually, in the TransPod transportation system, the location of the FluxJet is known, so in practice, we can modify the DNN parameters in real time.

[Figure 5.10](#) and [Figure 5.11](#) show the NMSE performance during testing across these defined distances. The outcomes show that the minimal error is observed when the network is both trained and tested at the same distance. However, better NMSE performance is recorded when the training is performed using SNR of 30 dB in [Figure 5.11](#). Actually, when higher SNR is employed in the training phase, the DNN is able to perform better since the impact of the AWGN noise is low. We note that the distinctive behavior observed in the curves corresponding to distances of 400m, 500m, and 600m can be attributed to shared characteristics in the delay and Doppler taps. Furthermore, we conclude that the DNN parameters should be adapted with the distance. Actually, in the TransPod transportation system, the location of the FluxJet is known, so in practice, we can modify the DNN parameters in real time.

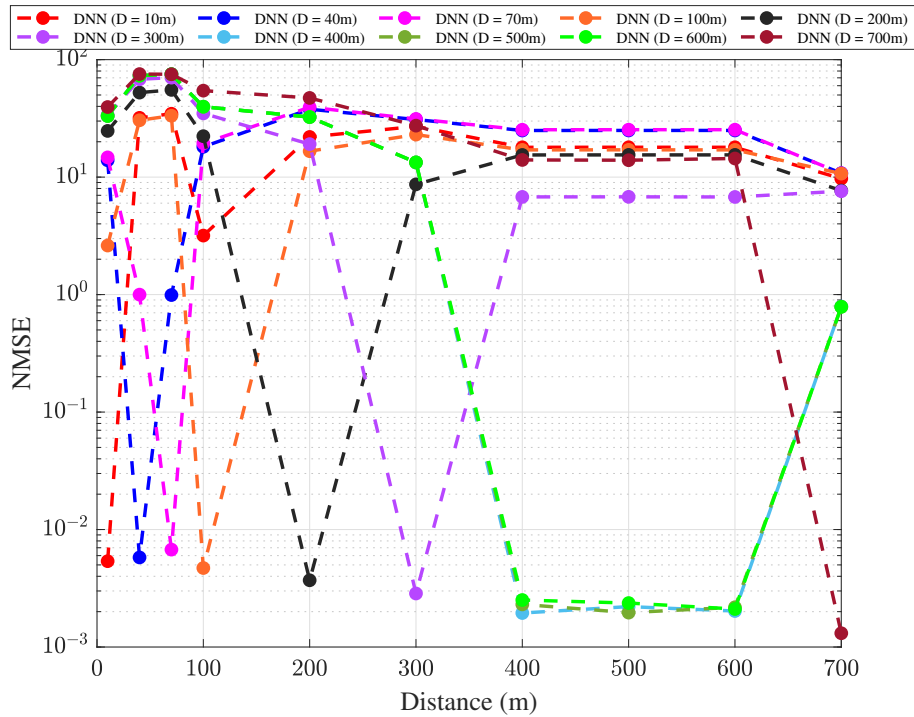


Figure 5.10: NMSE performance of the trained DNN model using several distances in data SNR = 15dB.

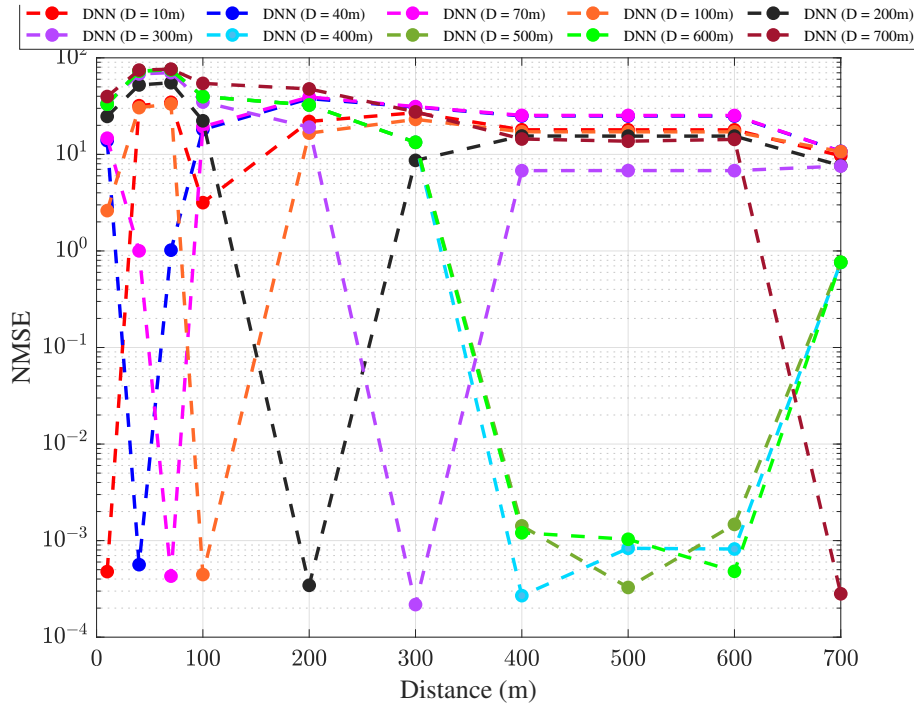


Figure 5.11: NMSE performance of the trained DNN model using several distances in data SNR = 30dB.

5.3.4 Impact of SNR on the trained DNN model

In the conducted study, we explored the NMSE and BER performance of a network trained specifically for a fixed SNR value within a defined range of 0 dB to 30 dB. This trained DNN for the given SNR is then tested for all the SNR levels. The results, displayed in Figure 5.12, illustrate that the network exhibits its most accurate and minimized error when tested at the specific SNR value it was originally trained on. However, training several DNN for different SNR values requires the SNR estimation at the receiver as well as increased memory storage.

As it can be seen from Figure 5.12, the DNN can be trained for the highest value of SNR, but used for all the SNR values. The degradation in the estimation error will not be too much. Furthermore, if we compare the BER curves of Figure 5.13, the impact on the performance is quite negligible if we use a high SNR trained DNN. This result can significantly reduce the system complexity because only one DNN is used for all the SNR values.

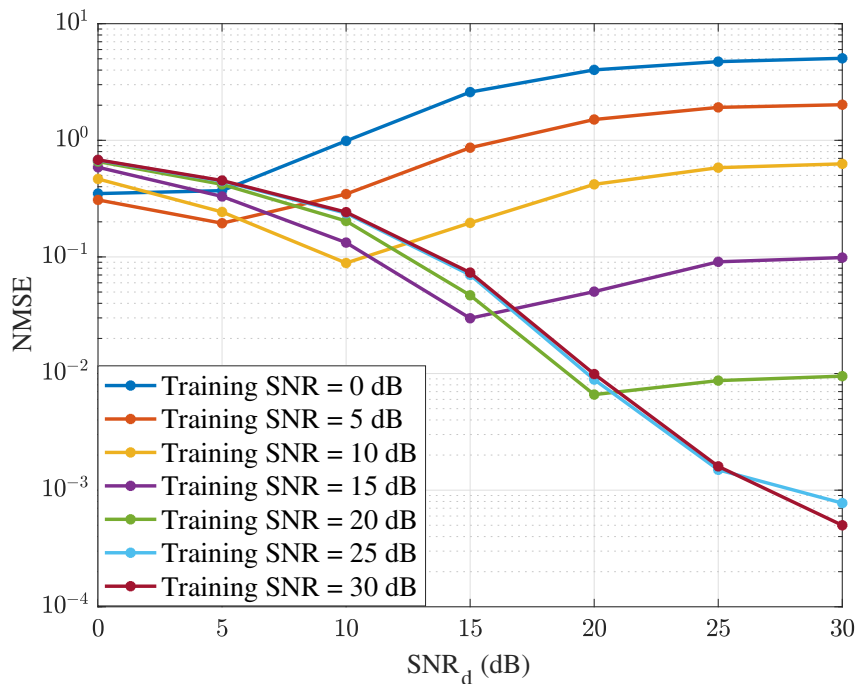


Figure 5.12: NMSE performance of the trained DNN model using different architectures.

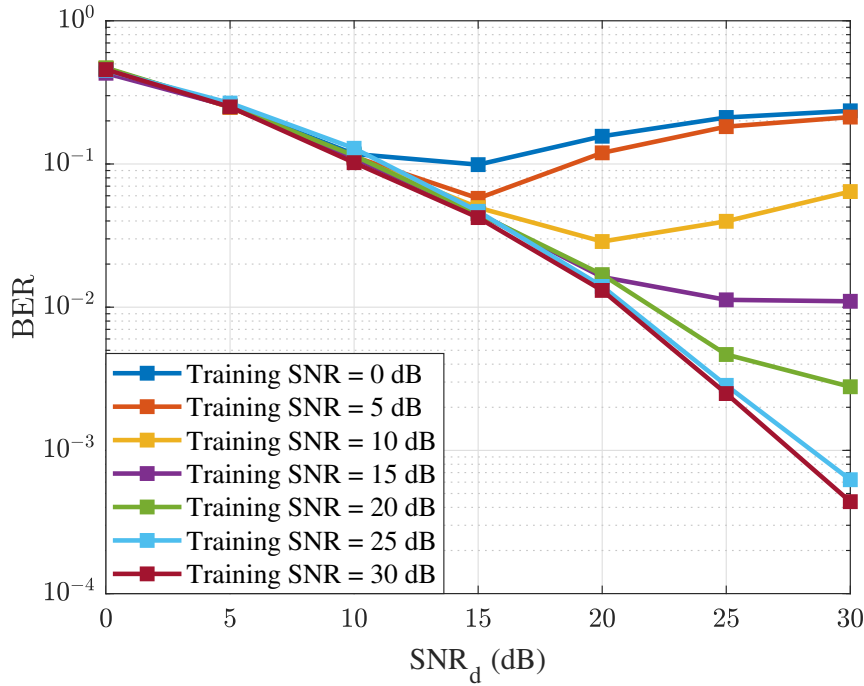


Figure 5.13: BER performance comparison between the different DNN architecture.

5.3.5 Computational Complexity

The required number of multiplication/division operations is a metric to evaluate the computational complexity. The threshold-based channel estimation methods with an impulse pilot [135] estimates the channel parameters from the $\mathbf{E} \in \mathbb{C}^{N \times (L_{\max} + 1)}$ matrix at the receiver, so the operation numbers is $N(l_{\max} + 1)$. For the channel estimation method with a sequence pilot proposed in the chapter 4, the complexity is $N^2(l_{\max} + 1) + PN + P$. For the proposed DNN-based estimator, the complexity comes from the DNN processing in (5.11), is about $2N(l_{\max} + 1)J + J^2 + (4l_{\max})J$. Here, J denotes the number of neurons in the the hidden layers. The DNN approach introduces increased computational complexity compared to conventional methods; however, it offers improved accuracy in channel estimation.

5.4 Summary

In this chapter, we introduced an innovative channel estimation method for OTFS systems utilizing machine learning, particularly the DNN approach. Our method addresses

the challenges posed by fractional normalized Doppler indices, where conventional techniques struggle with the pilot symbol leakage effect. Through simulations, we demonstrated the superior performance of our DNN-based channel estimation utilizing CAZAC sequence, even under conditions of low pilot power. Additionally, this not only ensures robust estimation but also achieves power efficiency during transmission.

6

Conclusion and Future Works

Sommaire

| | |
|----------------------------|-----|
| 6.1 Conclusion | 158 |
| 6.2 Future Works | 158 |

6.1 Conclusion

This thesis explores channel modeling and physical layer design to enhance high data rate communications in high mobility wireless channels, with a specific focus on the TransPod system. The work begins with a comprehensive review of wireless channels, focusing on doubly selective channels, their impairments, and modulation techniques such as OFDM and OTFS. We then characterize the TransPod guideway transmission channel, examining both large-scale and small-scale characteristics, and addressing noise from the plasma-based power transmission system. A dual-link communication system is proposed to mitigate frequent disconnectivity or handover. We propose a novel sequence pilot based channel estimation technique for OTFS systems in delay-Doppler domain, and introduce a machine learning-based method for fractional Doppler channel estimation using DNN.

6.2 Future Works

The future work can be considered in several directions. The research presented in [chapter 3](#) of this thesis has highlighted the challenges of impulsive noise and frequent handovers in the TransPod system. To further enhance the performance of the system, we propose two key areas for future work: designing appropriate coding techniques to mitigate impulsive noise and implementing a dual-link system.

One potential direction is the development of advanced coding techniques, specifically robust erasure codes optimized for the constraints of TransPod tube, to mitigate the impact of impulsive noise. Given that impulsive noise can corrupt transmitted signals to the point of packet erasure, the work could involve investigating and implementing advanced fountain codes like LT codes and Raptor codes for efficient data recovery, as well as exploring novel error correction codes, to provide efficient protection against packet erasures.

Additionally, future work could involve the implementation and testing of a dual-link communication system to create a seamless handover. This approach would be evaluated in various real-world scenarios, including different vehicle speeds and environmental conditions, with the aim of optimizing the system for smooth transitions between links and minimizing latency and packet loss during handovers.

Real-world validation is another important area for future research. The entire system could be tested using Universal Software Radio Peripheral (USRP) modules, focusing on real-world implementation and validation. This would include testing the system in metal tube structures at realistic speeds to gather performance data and validate simulation results, as well as characterizing the communication channel under various conditions to refine the system's models and improve its robustness.

Following this, the OTFS modulation technique could be further explored. Future work could evaluate the OTFS system's performance under real-world conditions, assessing its reliability and ability to handle high-mobility scenarios.

Another significant direction could be the exploration of multi-antenna systems, utilizing Multiple-Input and Multiple-Output (MIMO) technology. Following this, the integrating OTFS with MIMO technology could be considered as an area for further investigation. Testing various MIMO configurations would help determine the optimal setup for in-tube transmission for TransPod-like communication systems. Advanced beam-forming techniques could also be explored to direct signals more precisely, reducing interference and improving communication quality.

Future research could also investigate the integration of OTFS with other emerging technologies such as 5G and beyond, as well as its application in Internet of Things

(IoT) networks.

Machine learning and artificial intelligence can play a crucial role in future work. Developing adaptive algorithms that can optimize system performance in real-time and using AI techniques for predictive maintenance could improve the overall reliability of the communication system in such environments.

Finally, hardware optimization could become a crucial area of focus. This effort might involve creating custom hardware components designed to meet the specific needs of the TransPod system, including specialized RF components, antennas, and processing units. Additionally, exploring ways to reduce the energy consumption of the communication system could make it more sustainable and cost-effective.

7

Bibliography

Sommaire

| | |
|--|-----|
| References | 162 |
| List of Publications | 178 |

References

- [1] S. Zeadally, J. Guerrero, and J. Contreras, “A tutorial survey on vehicle-to-vehicle communications,” *Telecommunication Systems*, vol. 73, no. 3, pp. 469–489, 2020.
- [2] M. N. Ahangar, Q. Z. Ahmed, F. A. Khan, and M. Hafeez, “A survey of autonomous vehicles: enabling communication technologies and challenges,” *Sensors*, vol. 21, no. 3, p. 706, 2021.
- [3] J. He, K. Yang, and H.-H. Chen, “6g cellular networks and connected autonomous vehicles,” *IEEE network*, vol. 35, no. 4, pp. 255–261, 2020.
- [4] R. Janzen, “TransPod ultra-high-speed tube transportation: dynamics of vehicles and infrastructure,” *Procedia Engineering*, vol. 199, pp. 8–17, 2017.
- [5] S. Alraih, I. Shayea, M. Behjati, *et al.*, “Revolution or evolution? technical requirements and considerations towards 6g mobile communications,” *Sensors*, vol. 22, no. 3, p. 762, 2022.
- [6] R. Janzen, “The FluxJet: Unveiling of a novel vehicle concept,” 2022.
- [7] R. Janzen, “The FluxJet: A high-speed vehicle for transportation, based on electric flux, magnetic flux, and veillance flux,” 2022.
- [8] Y. Zhao and S.-G. Haggman, “Sensitivity to doppler shift and carrier frequency errors in ofdm systems-the consequences and solutions,” in *Proceedings of Vehicular Technology Conference-VTC*, IEEE, vol. 3, 1996, pp. 1564–1568.
- [9] M. Series, “Introduction to railway communication systems,” *Report ITU-R M. 2395-0*, 2016.
- [10] G. Hui, W. Hao, and Z. Yushu, “GSM-R network planning for high speed railway,” 2010.
- [11] R. He, B. Ai, G. Wang, *et al.*, “High-speed railway communications: from GSM-R to LTE-R,” *IEEE Vehicular Technology Magazine*, vol. 11, no. 3, pp. 49–58, 2016.

- [12] L. Zhu, F. R. Yu, B. Ning, and T. Tang, "Cross-layer handoff design in mimo-enabled wlans for communication-based train control (cbtc) systems," *IEEE Journal on Selected Areas in Communications*, vol. 30, no. 4, pp. 719–728, 2012.
- [13] E. TR, "5g: study on scenarios and requirements for next generation access technologies (3gpp tr 38.913 version 14.2. 0 release 14)," *ETSI TR 138 913*, 2017.
- [14] F. Hasegawa, A. Taira, G. Noh, *et al.*, "High-speed train communications standardization in 3gpp 5g nr," *IEEE Communications Standards Magazine*, vol. 2, no. 1, pp. 44–52, 2018.
- [15] J. Kim, M. Schmieder, M. Peter, *et al.*, "A comprehensive study on mmwave-based mobile hotspot network system for high-speed train communications," *IEEE Transactions on Vehicular Technology*, vol. 68, no. 3, pp. 2087–2101, 2018.
- [16] M. Zhou, "Analysis on the technical characteristics of wireless communication between vehicles and grounds of shanghai maglev line," *Urban Mass Transit*, vol. 13, pp. 26–29, 2010.
- [17] D. Yu, G. Yue, N. Wei, *et al.*, "Empirical study on directional millimeter-wave propagation in railway communications between train and trackside," *IEEE Journal on Selected Areas in Communications*, vol. 38, no. 12, pp. 2931–2945, 2020.
- [18] A. Bazin, B. Jahan, and M. H elard, "Doppler effect reduction in an ofdm system thanks to massive mimo," *IEEE Access*, vol. 6, pp. 38 498–38 511, 2018.
- [19] L. Zou, Z. Li, L. Liu, and J. Wang, "A design method for a leaky-wave system with uniform field coverage and broadside radiation for a vacuum-tube ultra-high-speed train," *IEEE Transactions on Antennas and Propagation*, vol. 70, no. 10, pp. 9936–9941, 2022.
- [20] J. Zhang, L. Liu, Z. Li, *et al.*, "Two novel structures of broadband wireless communication for high-speed flying train in vacuum tube," in *2019 28th wireless and optical communications conference (WOCC)*, IEEE, 2019, pp. 1–5.
- [21] C. Qiu, L. Liu, Y. Liu, Z. Li, J. Zhang, and T. Zhou, "Key technologies of broadband wireless communication for vacuum tube high-speed flying train," in *2019 IEEE 89th Vehicular Technology Conference (VTC2019-Spring)*, IEEE, 2019, pp. 1–5.
- [22] B. Kazemzadeh, R. Janzen, H. Meghdadi, V. Meghdadi, and A. Bradai, "Modeling of noise due to a plasma-based contactless power transmission system for ultra-high-speed transportation," in *Ubiquitous Networking*, O. Habachi, G. Chalhoub, H. Elbiaze, and E. Sabir, Eds., Cham: Springer Nature Switzerland, 2024, pp. 149–159.

- [23] B. Kazemzadeh, R. Janzen, V. Meghdadi, H. Meghdadi, and A. Bradai, “Enhancing channel estimation in high mobility ofts systems: a novel pilot-based method exploiting doppler axis diversity in a transpod transportation system,” in *GLOBECOM 2023-2023 IEEE Global Communications Conference*, IEEE, 2023, pp. 4958–4963.
- [24] B. Kazemzadeh, A. Gizzini, R. Janzen, H. Meghdadi, V. Meghdadi, and A. Bradai, “Deep learning based channel estimation in zp-ofts modulation systems utilizing cazac sequence pilot (submitted),” *IEEE Communications Letters*, 2024.
- [25] F. Hlawatsch and G. Matz, *Wireless communications over rapidly time-varying channels*. Academic press, 2011.
- [26] D. Tse and P. Viswanath, “The wireless channel,” in *Fundamentals of Wireless Communication*. Cambridge University Press, 2005, pp. 10–48.
- [27] Y. S. Cho, J. Kim, W. Y. Yang, and C. G. Kang, *MIMO-OFDM wireless communications with MATLAB*. John Wiley & Sons, 2010.
- [28] T. S. Rappaport, “Mobile radio propagation: large-scale path loss,” *Wireless communications: principles and practice*, pp. 107–110, 2002.
- [29] J. A. Shaw, “Radiometry and the friis transmission equation,” *American journal of physics*, vol. 81, no. 1, pp. 33–37, 2013.
- [30] C. A. Balanis, “Antenna theory: design and analysis,” *The 3rd Edition, John Wiley and Sons, NJ*, pp. 978–979, 1997.
- [31] M. Pätzold, *Mobile radio channels*. John Wiley & Sons, 2011.
- [32] A. R. Bahai, B. R. Saltzberg, and M. Ergen, *Multi-carrier digital communications: theory and applications of OFDM*. Springer Science & Business Media, 2004.
- [33] Y. Jiang and A. Papandreou-Suppappola, “Discrete time-frequency characterizations of dispersive linear time-varying systems,” *IEEE Transactions on Signal Processing*, vol. 55, no. 5, pp. 2066–2076, 2007.
- [34] W. C. Jakes and D. C. Cox, *Microwave mobile communications*. Wiley-IEEE press, 1994.
- [35] Y. Hong, T. Thaj, and E. Viterbo, *Delay-Doppler Communications: Principles and Applications*. Academic Press, 2022.
- [36] S. Parkvall and J. Skold, “4g lte/lte-advanced for mobile broadband,” *LTE-Advanced for Mobile Broadband Academic Press USA*, 2011.
- [37] R. Hadani, S. Rakib, M. Tsatsanis, *et al.*, “Orthogonal time frequency space modulation,” in *2017 IEEE Wireless Communications and Networking Conference (WCNC)*, IEEE, 2017, pp. 1–6.

- [38] L. Gaudio, G. Colavolpe, and G. Caire, "Otf vs. ofdm in the presence of sparsity: a fair comparison," *IEEE Transactions on Wireless Communications*, vol. 21, no. 6, pp. 4410–4423, 2021.
- [39] N. Dewangan, *A detailed Study of 4G in Wireless Communication: Looking insight in issues in OFDM*. Anchor Academic Publishing (aap_verlag), 2014.
- [40] B. Farhang-Boroujeny and H. Moradi, "Ofdm inspired waveforms for 5g," *IEEE Communications Surveys & Tutorials*, vol. 18, no. 4, pp. 2474–2492, 2016.
- [41] M. Rahman, S. Das, and F. Fitzek, "Ofdm based wlan systems," *Center for TeleInfrastruktur (CTiF), Technical report R-04-1002*, 2005.
- [42] P. Dhok and A. Dhanvijay, "A review on digital video broadcasting terrestrial (dvb-t) based ofdm system," *International Journal of Engineering and Techniques*, vol. 1, no. 2, pp. 27–31, 2015.
- [43] S. Ghosh and A. Bass, "Implementation of digital video broadcasting-terrestrial (dvb-t) using orthogonal frequency division multiplexing (ofdm) on physical media dependent sub layer," *Int. J. Comput. Appl.*, vol. 44, no. 22, pp. 20–25, 2012.
- [44] Y. Sun and L. Tong, "Channel equalization using one-tap dfe for wireless ofdm systems with ici and isi," in *1999 2nd IEEE Workshop on Signal Processing Advances in Wireless Communications (Cat. No. 99EX304)*, IEEE, 1999, pp. 146–149.
- [45] T. Wang, J. G. Proakis, E. Masry, and J. R. Zeidler, "Performance degradation of ofdm systems due to doppler spreading," *IEEE Transactions on wireless communications*, vol. 5, no. 6, pp. 1422–1432, 2006.
- [46] J. Flores de Valgas, J. F. Monserrat, and H. Arslan, "Flexible numerology in 5g nr: interference quantification and proper selection depending on the scenario," *Mobile Information Systems*, vol. 2021, pp. 1–9, 2021.
- [47] F. Conceição, M. Gomes, V. Silva, R. Dinis, A. Silva, and D. Castanheira, "A survey of candidate waveforms for beyond 5g systems," *Electronics*, vol. 10, no. 1, p. 21, 2020.
- [48] R. Hadani, S. Rakib, M. Tsatsanis, *et al.*, "Orthogonal time frequency space modulation," in *2017 IEEE Wireless Communications and Networking Conference (WCNC)*, IEEE, 2017, pp. 1–6.
- [49] F. Lampel, A. Alvarado, and F. M. Willems, "Orthogonal time frequency space modulation: a discrete zak transform approach," *arXiv preprint arXiv:2106.12828*, 2021.
- [50] H. Bölcskei, *Gabor expansion and frame theory*. na, 1994.

- [51] H. Bolcskei and F. Hlawatsch, "Discrete zak transforms, polyphase transforms, and applications," *IEEE Transactions on signal processing*, vol. 45, no. 4, pp. 851–866, 1997.
- [52] A. Farhang, A. RezaZadehReyhani, L. E. Doyle, and B. Farhang-Boroujeny, "Low complexity modem structure for ofdm-based orthogonal time frequency space modulation," *IEEE Wireless Communications Letters*, vol. 7, no. 3, pp. 344–347, 2017.
- [53] A. Shafie, J. Yuan, Y. Fang, P. Fitzpatrick, and T. Sakurai, "Coexistence of ofts modulation with ofdm-based communication systems," in *GLOBECOM 2023-2023 IEEE Global Communications Conference*, IEEE, 2023, pp. 4056–4061.
- [54] H. B. Mishra, P. Singh, A. K. Prasad, and R. Budhiraja, "Ofts channel estimation and data detection designs with superimposed pilots," *IEEE transactions on wireless communications*, vol. 21, no. 4, pp. 2258–2274, 2021.
- [55] P. Raviteja, K. T. Phan, Y. Hong, and E. Viterbo, "Interference cancellation and iterative detection for orthogonal time frequency space modulation," *IEEE transactions on wireless communications*, vol. 17, no. 10, pp. 6501–6515, 2018.
- [56] R. Janzen, *Plasma-based high-speed power transmission system*, US Patent 11,524,583, Dec. 2022.
- [57] B. Ai, X. Cheng, T. Kürner, *et al.*, "Challenges toward wireless communications for high-speed railway," *IEEE transactions on intelligent transportation systems*, vol. 15, no. 5, pp. 2143–2158, 2014.
- [58] R. He, B. Ai, G. Wang, *et al.*, "High-speed railway communications: from GSM-R to LTE-R," *IEEE Vehicular Technology Magazine*, vol. 11, no. 3, pp. 49–58, 2016.
- [59] D. G. Dudley and H.-Y. Pao, "System identification for wireless propagation channels in tunnels," *IEEE Transactions on Antennas and Propagation*, vol. 53, no. 8, pp. 2400–2405, 2005.
- [60] P. Pajusco, "Propagation channel models for mobile communication," *Comptes Rendus Physique*, vol. 7, no. 7, pp. 703–714, 2006.
- [61] L. Liu, C. Tao, J. Qiu, *et al.*, "Position-based modeling for wireless channel on high-speed railway under a viaduct at 2.35 ghz," *IEEE Journal on Selected Areas in Communications*, vol. 30, no. 4, pp. 834–845, 2012.
- [62] X. Cai, J. Rodríguez-Piñeiro, X. Yin, *et al.*, "An empirical air-to-ground channel model based on passive measurements in lte," *IEEE Transactions on Vehicular Technology*, vol. 68, no. 2, pp. 1140–1154, 2018.

- [63] S. L. Cebula III, A. Ahmad, J. M. Graham, *et al.*, “Empirical channel model for 2.4 ghz ieee 802.11 wlan,” in *Proceedings of the International Conference on Wireless Networks (ICWN)*, Citeseer, 2011, p. 1.
- [64] C.-X. Wang, A. Ghazal, B. Ai, Y. Liu, and P. Fan, “Channel measurements and models for high-speed train communication systems: a survey,” *IEEE communications surveys & tutorials*, vol. 18, no. 2, pp. 974–987, 2015.
- [65] K. Guan, Z. Zhong, B. Ai, and T. Kurner, “Deterministic propagation modeling for the realistic high-speed railway environment,” in *2013 IEEE 77th Vehicular Technology Conference (VTC Spring)*, IEEE, 2013, pp. 1–5.
- [66] E. Greenberg and E. Klodzh, “Comparison of deterministic, empirical and physical propagation models in urban environments,” in *2015 IEEE International Conference on Microwaves, Communications, Antennas and Electronic Systems (COMCAS)*, IEEE, 2015, pp. 1–5.
- [67] A. Tavsanoğlu, C. Briso, D. Carmena-Cabanillas, and R. B. Arancibia, “Concepts of hyperloop wireless communication at 1200 km/h: 5g, wi-fi, propagation, doppler and handover,” *Energies*, vol. 14, no. 4, p. 983, 2021.
- [68] N. Selina *et al.*, “Solution of maxwell’s equations for cylindrical symmetry waveguides,” *Journal of Applied Mathematics and Physics*, vol. 8, no. 05, p. 753, 2020.
- [69] B. Han, J. Zhang, L. Liu, and C. Tao, “Position-based wireless channel characterization for the high-speed vactrains in vacuum tube scenarios using propagation graph modeling theory,” *Radio Science*, vol. 55, no. 4, pp. 1–12, 2020.
- [70] L. Tian, V. Degli-Esposti, E. M. Vitucci, and X. Yin, “Semi-deterministic radio channel modeling based on graph theory and ray-tracing,” *IEEE Transactions on Antennas and Propagation*, vol. 64, no. 6, pp. 2475–2486, 2016.
- [71] T. Pedersen, G. Steinbock, and B. H. Fleury, “Modeling of reverberant radio channels using propagation graphs,” *IEEE Transactions on Antennas and Propagation*, vol. 60, no. 12, pp. 5978–5988, 2012.
- [72] B. Han, J. Zhang, L. Liu, and C. Tao, “Position-based wireless channel characterization for the high-speed vactrains in vacuum tube scenarios using propagation graph modeling theory,” *Radio Science*, vol. 55, no. 4, pp. 1–12, 2020.
- [73] C. Zhou, “Ray tracing and modal methods for modeling radio propagation in tunnels with rough walls,” *IEEE transactions on antennas and propagation*, vol. 65, no. 5, pp. 2624–2634, 2017.
- [74] F. Fuschini and G. Falciasecca, “A mixed rays—modes approach to the propagation in real road and railway tunnels,” *IEEE Transactions on Antennas and Propagation*, vol. 60, no. 2, pp. 1095–1105, 2011.

- [75] Y. Zhang, Y. Liu, J. Sun, C.-X. Wang, and X. Ge, "Impact of different parameters on channel characteristics in a high-speed train ray tracing tunnel channel model," in *2017 IEEE 85th Vehicular Technology Conference (VTC Spring)*, 2017, pp. 1–5.
- [76] Y. P. Zhang, "Novel model for propagation loss prediction in tunnels," *IEEE Transactions on Vehicular Technology*, vol. 52, no. 5, pp. 1308–1314, 2003.
- [77] A. Hrovat, G. Kandus, and T. Javornik, "A survey of radio propagation modeling for tunnels," *IEEE Communications Surveys & Tutorials*, vol. 16, no. 2, pp. 658–669, 2013.
- [78] I. Lazányi and L. Szirmay-Kalos, "Fresnel term approximations for metals," 2005.
- [79] C. Schlick, "An inexpensive brdf model for physically-based rendering," in *Computer graphics forum*, Wiley Online Library, vol. 13, 1994, pp. 233–246.
- [80] N. Hoffman, "Fresnel Equations Considered Harmful," in *Workshop on Material Appearance Modeling*, R. Klein and H. Rushmeier, Eds., The Eurographics Association, 2019.
- [81] J. Mistrik, S. Kasap, H. E. Ruda, C. Koughia, and J. Singh, "Optical properties of electronic materials: fundamentals and characterization," *Springer handbook of electronic and photonic materials*, pp. 1–1, 2017.
- [82] S. O. Kasap, *Electronic materials and Devices*. McGraw-Hill New York, 2006.
- [83] T. J. Roupael, *Wireless Receiver Architectures and Design: Antennas, RF, synthesizers, mixed signal, and digital signal processing*. Academic Press, 2014.
- [84] R. Janzen, *Vehicle for travelling along a linear route guideway*, US Patent 11,235,666, Feb. 2022.
- [85] I. Boldea, *Linear electric machines, drives, and MAGLEVs handbook*. CRC press, 2013.
- [86] R. Janzen and S. Mann, "Veillance flux, vixels, veillons: an information-bearing extramissive formulation of sensing, to measure surveillance and sousveillance," in *2014 IEEE 27th Canadian Conference on Electrical and Computer Engineering (CCECE)*, IEEE, 2014, pp. 1–10.
- [87] R. Janzen and S. Mann, "The physical-fourier-amplitude domain, and application to sensing sensors," in *2016 IEEE International Symposium on Multimedia (ISM)*, IEEE, 2016, pp. 317–320.
- [88] S. Yang, *Veillametrics: An extramissive approach to analyze and visualize audio and visual sensory flux*. University of Toronto (Canada), 2018.
- [89] J.-L. Meyzonnette, J. Mangin, and M. Cathelinaud, "Refractive index of optical materials," *Springer Handbook of Glass*, pp. 997–1045, 2019.

- [90] B. I. Bleaney, B. I. Bleaney, and B. Bleaney, *Electricity and Magnetism, Volume 2*. Oxford University Press (UK), 2013, vol. 2.
- [91] J. Mistrik, S. Kasap, H. E. Ruda, C. Koughia, and J. Singh, “Optical properties of electronic materials: fundamentals and characterization,” *Springer handbook of electronic and photonic materials*, pp. 1–1, 2017.
- [92] F. Silveira and S. Kurcbart, “Hagen-rubens relation beyond far-infrared region,” *Europhysics Letters*, vol. 90, no. 4, p. 44 004, 2010.
- [93] A. Seifiter, “About the meaning of the hagen—rubens relation to radiation thermometry,” in *Proceedings of the XVII IMEKO World Congress Metrology in the 3rd Millennium, Dubrovnik, Croatia, Citeseer*, 2003, pp. 22–27.
- [94] H.-N. Dai, K.-W. Ng, M. Li, and M.-Y. Wu, “An overview of using directional antennas in wireless networks,” *International journal of communication systems*, vol. 26, no. 4, pp. 413–448, 2013.
- [95] H. L. Bertoni, *Radio propagation for modern wireless systems*. Pearson Education, 1999.
- [96] W. L. Stutzman and G. A. Thiele, *Antenna theory and design*. John Wiley & Sons, 2012.
- [97] Z. Xu, C. Yang, Z. Tan, and Z. Sheng, “Raptor code-enabled reliable data transmission for in-vehicle power line communication systems with impulsive noise,” *IEEE Communications Letters*, vol. 21, no. 10, pp. 2154–2157, 2017.
- [98] T. Bai, H. Zhang, R. Zhang, *et al.*, “Discrete multi-tone digital subscriber loop performance in the face of impulsive noise,” *IEEE Access*, vol. 5, pp. 10 478–10 495, 2017.
- [99] U. Epple and M. Schnell, “Advanced blanking nonlinearity for mitigating impulsive interference in ofdm systems,” *IEEE Transactions on Vehicular Technology*, vol. 66, no. 1, pp. 146–158, 2016.
- [100] N. B. Sarr, A. K. Yazbek, H. Boeglen, J.-P. Cances, R. Vauzelle, and F. Gagnon, “An impulsive noise resistant physical layer for smart grid communications,” in *2017 IEEE International Conference on Communications (ICC)*, IEEE, 2017, pp. 1–7.
- [101] P. Chen, Y. Rong, S. Nordholm, Z. He, and A. J. Duncan, “Joint channel estimation and impulsive noise mitigation in underwater acoustic ofdm communication systems,” *IEEE Transactions on Wireless Communications*, vol. 16, no. 9, pp. 6165–6178, 2017.

- [102] A. Mahmood and M. Chitre, "Ambient noise in warm shallow waters: a communications perspective," *IEEE communications magazine*, vol. 55, no. 6, pp. 198–204, 2017.
- [103] D. Middleton, I. of Electrical, and E. Engineers, *An introduction to statistical communication theory*. McGraw-Hill New York, 1960, vol. 960.
- [104] M. Ghosh, "Analysis of the effect of impulse noise on multicarrier and single carrier qam systems," *IEEE Transactions on Communications*, vol. 44, no. 2, pp. 145–147, 1996.
- [105] G. Ndo, F. Labeau, and M. Kassouf, "A markov-middleton model for bursty impulsive noise: modeling and receiver design," *IEEE Transactions on Power Delivery*, vol. 28, no. 4, pp. 2317–2325, 2013.
- [106] D. Fertoni and G. Colavolpe, "On reliable communications over channels impaired by bursty impulse noise," *IEEE Transactions on Communications*, vol. 57, no. 7, pp. 2024–2030, 2009.
- [107] J. Dannemann and H. Holzmam, "Testing for two states in a hidden markov model," *Canadian Journal of Statistics*, vol. 36, no. 4, pp. 505–520, 2008.
- [108] D. Middleton, "Statistical-physical models of electromagnetic interference," *IEEE transactions on Electromagnetic Compatibility*, no. 3, pp. 106–127, 1977.
- [109] S. V. Vaseghi and S. V. Vaseghi, "Impulsive noise," *Advanced Signal Processing and Digital Noise Reduction*, pp. 294–313, 1996.
- [110] Z. Xu, C. Yang, Z. Tan, and Z. Sheng, "Raptor code-enabled reliable data transmission for in-vehicle power line communication systems with impulsive noise," *IEEE Communications Letters*, vol. 21, no. 10, pp. 2154–2157, 2017.
- [111] A. Mizera, J. Pang, and Q. Yuan, "Reviving the two-state markov chain approach," *IEEE/ACM transactions on computational biology and bioinformatics*, vol. 15, no. 5, pp. 1525–1537, 2017.
- [112] K. Yu, T. Sato, *et al.*, "Modeling and analysis of error process in 5g wireless communication using two-state markov chain," *IEEE Access*, vol. 7, pp. 26 391–26 401, 2019.
- [113] M. Kijima, *Markov processes for stochastic modeling*. Springer, 2013.
- [114] M. Luby, "Lt codes," in *The 43rd Annual IEEE Symposium on Foundations of Computer Science, 2002. Proceedings.*, IEEE Computer Society, 2002, pp. 271–271.
- [115] A. Shokrollahi, "Raptor codes," *IEEE transactions on information theory*, vol. 52, no. 6, pp. 2551–2567, 2006.

- [116] N. Andreadou and A. M. Tonello, "On the mitigation of impulsive noise in power-line communications with LT codes," *IEEE Transactions on Power Delivery*, vol. 28, no. 3, pp. 1483–1490, 2013.
- [117] T. Li, W. H. Mow, and M. H. Siu, "A joint approach to erasure marking and viterbi decoding for impulsive noise channels," in *2003 4th IEEE Workshop on Signal Processing Advances in Wireless Communications-SPAWC 2003 (IEEE Cat. No. 03EX689)*, IEEE, 2003, pp. 180–184.
- [118] H. H. Nguyen and T. Q. Bui, "Bit-interleaved coded ofdm with iterative decoding in impulsive noise," *IEEE transactions on power delivery*, vol. 23, no. 2, pp. 640–649, 2008.
- [119] H. H. Nguyen and T. Q. Bui, "Bit-interleaved coded modulation with iterative decoding in impulsive noise," *IEEE transactions on power delivery*, vol. 22, no. 1, pp. 151–160, 2006.
- [120] R. Pighi, M. Franceschini, G. Ferrari, and R. Raheli, "Fundamental performance limits of communications systems impaired by impulse noise," *IEEE Transactions on Communications*, vol. 57, no. 1, pp. 171–182, 2009.
- [121] A. Al-Dweik, A. Hazmi, B. Sharif, and C. Tsimenidis, "Efficient interleaving technique for ofdm system over impulsive noise channels," in *21st Annual IEEE international symposium on personal, indoor and mobile radio communications*, IEEE, 2010, pp. 167–171.
- [122] S. Nayyef, C. Tsimenidis, A. Al-Dweik, B. Sharif, and A. Hazmi, "Time-and frequency-domain impulsive noise spreader for ofdm systems," in *2012 IEEE 11th International Conference on Trust, Security and Privacy in Computing and Communications*, IEEE, 2012, pp. 1856–1861.
- [123] B. Sklar, "Reed-solomon codes," *Downloaded from URL <http://www.informit.com/content/images/art.sub.-sklar7.sub.-reed-solomo-n/elementLinks/art.sub.-sklar7.sub.-reed-solomon.pdf>*, pp. 1–33, 2001.
- [124] D. Toumpakaris, W. Yu, J. M. Cioffi, D. Gardan, and M. Ouzzif, "A simple byte-erasure method for improved impulse immunity in dsl," in *IEEE International Conference on Communications, 2003. ICC'03.*, IEEE, vol. 4, 2003, pp. 2426–2430.
- [125] A. Hadi, K. M. Rabie, and E. Alsusa, "Polar codes based OFDM-PLC systems in the presence of middleton class-a noise," in *2016 10th International Symposium on Communication Systems, Networks and Digital Signal Processing (CSNDSP)*, IEEE, 2016, pp. 1–6.

- [126] D. D. Lin, R. A. Pacheco, T. J. Lim, and D. Hatzinakos, "Joint estimation of channel response, frequency offset, and phase noise in ofdm," *IEEE Transactions on Signal Processing*, vol. 54, no. 9, pp. 3542–3554, 2006.
- [127] M.-H. Hsieh and C.-H. Wei, "Channel estimation for ofdm systems based on comb-type pilot arrangement in frequency selective fading channels," *IEEE Transactions on Consumer Electronics*, vol. 44, no. 1, pp. 217–225, 1998.
- [128] Y. Liu, Z. Tan, H. Hu, L. J. Cimini, and G. Y. Li, "Channel estimation for ofdm," *IEEE Communications Surveys & Tutorials*, vol. 16, no. 4, pp. 1891–1908, 2014.
- [129] S. Coleri, M. Ergen, A. Puri, and A. Bahai, "Channel estimation techniques based on pilot arrangement in ofdm systems," *IEEE Transactions on broadcasting*, vol. 48, no. 3, pp. 223–229, 2002.
- [130] T. Wang, J. G. Proakis, E. Masry, and J. R. Zeidler, "Performance degradation of ofdm systems due to doppler spreading," *IEEE Transactions on wireless communications*, vol. 5, no. 6, pp. 1422–1432, 2006.
- [131] J. Wu and P. Fan, "A survey on high mobility wireless communications: challenges, opportunities and solutions," *IEEE Access*, vol. 4, pp. 450–476, 2016.
- [132] H. M. Mahmoud, A. S. Mousa, and R. Saleem, "Channel estimation based in comb-type pilots arrangement for ofdm system over time varying channel," *Journal of networks*, vol. 5, no. 7, p. 766, 2010.
- [133] Z. Tang, R. C. Cannizzaro, G. Leus, and P. Banelli, "Pilot-assisted time-varying channel estimation for ofdm systems," *IEEE Transactions on Signal Processing*, vol. 55, no. 5, pp. 2226–2238, 2007.
- [134] O. K. Rasheed, G. Surabhi, and A. Chockalingam, "Sparse delay-doppler channel estimation in rapidly time-varying channels for multiuser ofds on the uplink," in *2020 IEEE 91st Vehicular Technology Conference (VTC2020-Spring)*, IEEE, 2020, pp. 1–5.
- [135] P. Raviteja, K. T. Phan, Y. Hong, and E. Viterbo, "Embedded delay-doppler channel estimation for orthogonal time frequency space modulation," in *2018 IEEE 88th Vehicular Technology Conference (VTC-Fall)*, IEEE, 2018, pp. 1–5.
- [136] P. Raviteja, K. T. Phan, and Y. Hong, "Embedded pilot-aided channel estimation for ofds in delay–doppler channels," *IEEE transactions on vehicular technology*, vol. 68, no. 5, pp. 4906–4917, 2019.
- [137] W. Yuan, S. Li, Z. Wei, J. Yuan, and D. W. K. Ng, "Data-aided channel estimation for ofds systems with a superimposed pilot and data transmission scheme," *IEEE wireless communications letters*, vol. 10, no. 9, pp. 1954–1958, 2021.

- [138] H. B. Mishra, P. Singh, A. K. Prasad, and R. Budhiraja, "Otf channel estimation and data detection designs with superimposed pilots," *IEEE transactions on wireless communications*, vol. 21, no. 4, pp. 2258–2274, 2021.
- [139] H. Zhao, Z. Kang, and H. Wang, "A novel channel estimation scheme for ofts," in *2020 IEEE 20th International Conference on Communication Technology (ICCT)*, IEEE, 2020, pp. 12–16.
- [140] W. Shen, L. Dai, J. An, P. Fan, and R. W. Heath, "Channel estimation for orthogonal time frequency space (otfs) massive mimo," *IEEE Transactions on Signal Processing*, vol. 67, no. 16, pp. 4204–4217, 2019.
- [141] A. Goldsmith, *Wireless communications*. Cambridge university press, 2005.
- [142] J. Zhang, L. Cai, and H. Liu, "Integrated sensing and communication via orthogonal time frequency space signaling with hybrid message passing detection and fractional parameter estimation," *Sensors*, vol. 23, no. 24, p. 9874, 2023.
- [143] S. Gao and J. Zheng, "Peak-to-average power ratio reduction in pilot-embedded ofts modulation through iterative clipping and filtering," *IEEE Communications Letters*, vol. 24, no. 9, pp. 2055–2059, 2020.
- [144] H. Alzer, "On the cauchy-schwarz inequality," *Journal of mathematical analysis and applications*, vol. 234, no. 1, pp. 6–14, 1999.
- [145] Z. Wei, W. Yuan, S. Li, J. Yuan, and D. W. K. Ng, "Transmitter and receiver window designs for orthogonal time-frequency space modulation," *IEEE transactions on communications*, vol. 69, no. 4, pp. 2207–2223, 2021.
- [146] P. Sanoopkumar and A. Farhang, "A practical pilot for channel estimation of ofts," in *ICC 2023-IEEE International Conference on Communications*, IEEE, 2023, pp. 1319–1325.
- [147] O. A. Aghda, M. J. Omid, and H. Saeedi-Sourck, "Low-overhead joint channel estimation and data detection in zp-ofts system," *arXiv preprint arXiv:2304.01681*, 2023.
- [148] T. M. Schmidl and D. C. Cox, "Robust frequency and timing synchronization for ofdm," *IEEE transactions on communications*, vol. 45, no. 12, pp. 1613–1621, 1997.
- [149] H. Minn, V. K. Bhargava, and K. B. Letaief, "A robust timing and frequency synchronization for ofdm systems," *IEEE Transactions on Wireless communications*, vol. 2, no. 4, pp. 822–839, 2003.
- [150] G. Ren, Y. Chang, H. Zhang, and H. Zhang, "Synchronization method based on a new constant envelop preamble for ofdm systems," *IEEE Transactions on Broadcasting*, vol. 51, no. 1, pp. 139–143, 2005.

- [151] R. Mutagi, "Pseudo noise sequences for engineers," *Electronics & communication engineering journal*, vol. 8, no. 2, pp. 79–87, 1996.
- [152] R. Frank, S. Zadoff, and R. Heimiller, "Phase shift pulse codes with good periodic correlation properties (corresp.)," *IRE Transactions on Information Theory*, vol. 8, no. 6, pp. 381–382, 1962.
- [153] K. R. Murali and A. Chockalingam, "On ofts modulation for high-doppler fading channels," in *2018 information theory and applications workshop (ITA)*, IEEE, 2018, pp. 1–10.
- [154] Y. Wen, W. Huang, and Z. Zhang, "Cazac sequence and its application in lte random access," in *2006 IEEE Information Theory Workshop-ITW'06 Chengdu*, IEEE, 2006, pp. 544–547.
- [155] A. Das, B. Mohanty, and B. Sahu, "A novel cazac sequence based timing synchronization scheme for ofdm system," in *2018 International Conference on Wireless Communications, Signal Processing and Networking (WiSPNET)*, IEEE, 2018, pp. 1–4.
- [156] J. Liu, K. Mei, X. Zhang, *et al.*, "Fine timing and frequency synchronization for mimo-ofdm: an extreme learning approach," *IEEE Transactions on Cognitive Communications and Networking*, vol. 8, no. 2, pp. 720–732, 2022.
- [157] S. E. Zegrar and H. Arslan, "Effect of prefix/suffix configurations on ofts systems with rectangular waveforms," *arXiv preprint arXiv:2205.14872*, 2022.
- [158] T. Thaj and E. Viterbo, "Low complexity iterative rake decision feedback equalizer for zero-padded ofts systems," *IEEE transactions on vehicular technology*, vol. 69, no. 12, pp. 15 606–15 622, 2020.
- [159] T. Thaj and E. Viterbo, "Low complexity iterative rake detector for orthogonal time frequency space modulation," in *2020 IEEE Wireless Communications and Networking Conference (WCNC)*, IEEE, 2020, pp. 1–6.
- [160] "1 - introductory material," in *Computer Solution of Large Linear Systems*, ser. Studies in Mathematics and Its Applications, G. Meurant, Ed., vol. 28, Elsevier, 1999, pp. 1–68. [Online]. Available: <https://www.sciencedirect.com/science/article/pii/S0168202499800022>.
- [161] T. M. Inc., *Communications toolbox, ofts modulation version: r2024a*, Natick, Massachusetts, United States, 2022. [Online]. Available: <https://www.mathworks.com>.
- [162] W. Yu, F. Sohrabi, and T. Jiang, "Role of deep learning in wireless communications," *IEEE BITS the Information Theory Magazine*, vol. 2, no. 2, pp. 56–72, 2022.

- [163] L. Dai, R. Jiao, F. Adachi, H. V. Poor, and L. Hanzo, "Deep learning for wireless communications: an emerging interdisciplinary paradigm," *IEEE Wireless Communications*, vol. 27, no. 4, pp. 133–139, 2020.
- [164] H. Ye, G. Y. Li, and B.-H. Juang, "Power of deep learning for channel estimation and signal detection in ofdm systems," *IEEE Wireless Communications Letters*, vol. 7, no. 1, pp. 114–117, 2017.
- [165] M. Soltani, V. Pourahmadi, and H. Sheikhzadeh, "Pilot pattern design for deep learning-based channel estimation in ofdm systems," *IEEE Wireless Communications Letters*, vol. 9, no. 12, pp. 2173–2176, 2020.
- [166] S. Hong, Y. Wang, Y. Pan, *et al.*, "Convolutional neural network aided signal modulation recognition in ofdm systems," in *2020 IEEE 91st Vehicular Technology Conference (VTC2020-Spring)*, IEEE, 2020, pp. 1–5.
- [167] X. Yi and C. Zhong, "Deep learning for joint channel estimation and signal detection in ofdm systems," *IEEE Communications Letters*, vol. 24, no. 12, pp. 2780–2784, 2020.
- [168] S. R. Mattu and A. Chockalingam, "Learning based delay-doppler channel estimation with interleaved pilots in ofds," in *2022 IEEE 96th Vehicular Technology Conference (VTC2022-Fall)*, IEEE, 2022, pp. 1–6.
- [169] A. Pfadler, P. Jung, V. Shala, M. Kasparick, M. Adrat, and S. Stanczak, "Short-term prediction of doubly-dispersive channels for pulse-shaped ofds using 2d-convlstm," in *2022 IEEE International Conference on Communications Workshops (ICC Workshops)*, IEEE, 2022, pp. 939–944.
- [170] L. Guo, P. Gu, J. Zou, G. Liu, and F. Shu, "Dnn-based fractional doppler channel estimation for ofds modulation," *IEEE Transactions on Vehicular Technology*, vol. 72, no. 11, pp. 15 062–15 067, 2023.
- [171] H.-I. Suk, "An introduction to neural networks and deep learning," in *Deep Learning for Medical Image Analysis*, Elsevier, 2017, pp. 3–24.
- [172] R. Y. Choi, A. S. Coyner, J. Kalpathy-Cramer, M. F. Chiang, and J. P. Campbell, "Introduction to machine learning, neural networks, and deep learning," *Translational vision science & technology*, vol. 9, no. 2, pp. 14–14, 2020.
- [173] W. Liu, Z. Wang, X. Liu, N. Zeng, Y. Liu, and F. E. Alsaadi, "A survey of deep neural network architectures and their applications," *Neurocomputing*, vol. 234, pp. 11–26, 2017.
- [174] T. Bouwmans, S. Javed, M. Sultana, and S. K. Jung, "Deep neural network concepts for background subtraction: a systematic review and comparative evaluation," *Neural Networks*, vol. 117, pp. 8–66, 2019.

- [175] D. Elbrächter, D. Perekrestenko, P. Grohs, and H. Bölcskei, “Deep neural network approximation theory,” *arXiv preprint arXiv:1901.02220*, 2019.
- [176] W. Schmidt, S. Raudys, M. Kraaijveld, M. Skurikhina, and R. Duin, “Initializations, back-propagation and generalization of feed-forward classifiers,” in *IEEE International Conference on Neural Networks*, 1993, 598–604 vol.1.
- [177] H. Yi, S. Shiyu, D. Xiusheng, and C. Zhigang, “A study on deep neural networks framework,” in *2016 IEEE advanced information management, communicates, electronic and automation control conference (IMCEC)*, IEEE, 2016, pp. 1519–1522.
- [178] H.-I. Suk, “An introduction to neural networks and deep learning,” in *Deep Learning for Medical Image Analysis*, Elsevier, 2017, pp. 3–24.
- [179] Z. Li, F. Liu, W. Yang, S. Peng, and J. Zhou, “A survey of convolutional neural networks: analysis, applications, and prospects,” *IEEE transactions on neural networks and learning systems*, vol. 33, no. 12, pp. 6999–7019, 2021.
- [180] K. O’shea and R. Nash, “An introduction to convolutional neural networks,” *arXiv preprint arXiv:1511.08458*, 2015.
- [181] L. Medsker and L. C. Jain, *Recurrent neural networks: design and applications*. CRC press, 1999.
- [182] Y. Huang, J. Gornet, S. Dai, *et al.*, “Neural networks with recurrent generative feedback,” *Advances in Neural Information Processing Systems*, vol. 33, pp. 535–545, 2020.
- [183] A. Sherstinsky, “Fundamentals of recurrent neural network (rnn) and long short-term memory (lstm) network,” *Physica D: Nonlinear Phenomena*, vol. 404, p. 132 306, 2020.
- [184] L. Prechelt, “Early stopping — but when?” In *Neural Networks: Tricks of the Trade: Second Edition*, G. Montavon, G. B. Orr, and K.-R. Müller, Eds. Berlin, Heidelberg: Springer Berlin Heidelberg, 2012, pp. 53–67. [Online]. Available: https://doi.org/10.1007/978-3-642-35289-8_5.
- [185] N. Polyzotis, M. Zinkevich, S. Roy, E. Breck, and S. Whang, “Data validation for machine learning,” *Proceedings of machine learning and systems*, vol. 1, pp. 334–347, 2019.
- [186] Y. Xu and R. Goodacre, “On splitting training and validation set: a comparative study of cross-validation, bootstrap and systematic sampling for estimating the generalization performance of supervised learning,” *Journal of analysis and testing*, vol. 2, no. 3, pp. 249–262, 2018.

- [187] P. Gavali and J. S. Banu, "Chapter 6 - deep convolutional neural network for image classification on cuda platform," in *Deep Learning and Parallel Computing Environment for Bioengineering Systems*, A. K. Sangaiah, Ed., Academic Press, 2019, pp. 99–122. [Online]. Available: <https://www.sciencedirect.com/science/article/pii/B9780128167182000130>.

List of Publications

Conférences internationales à comité de lecture

- B. Kazemzadeh, A. k. Gizzini, V. Meghdadi, H. Meghdadi, and R. Janzen, “Deep learning based channel estimation in zp-ofds modulation systems utilizing cazac sequence pilot (submitted),” IEEE Wireless Communications and Networking Conference (WCNC), 2024.
- B. Kazemzadeh, R. Janzen, V. Meghdadi, H. Meghdadi, and A. Bradai, “Enhancing channel estimation in high mobility ofds systems: a novel pilot-based method exploiting doppler axis diversity in a transpod transportation system,” IEEE Global Communications Conference, 2023. [Online]. Available: <https://ieeexplore.ieee.org/abstract/document/10436957>.
- B. Kazemzadeh, R. Janzen, H. Meghdadi, V. Meghdadi, and A. Bradai, “Modeling of noise due to a plasma-based contactless power transmission system for ultra-high-speed transportation,” pp. 149–159, 2023. [Online]. Available: https://doi.org/10.1007/978-3-031-62488-9_12.

Conception d'un système de transmission haut débit dans un canal doublement sélectif: système de TransPod

Résumé : Cette thèse explore la modélisation des canaux et la conception de la couche physique pour améliorer les communications à haut débit dans les canaux sans fil à haute mobilité, en se concentrant spécifiquement sur le système TransPod. Le travail commence par une revue complète des canaux sans fil, en se focalisant sur les canaux doublement sélectifs, leurs dégradations, et les techniques de modulation telles que OFDM et OTFS. Nous caractérisons ensuite le canal de transmission du guide TransPod, en examinant à la fois les caractéristiques à grande échelle et à petite échelle, et en traitant le bruit provenant du système de transmission de puissance basé sur le plasma. Un système de communication à double liaison est proposé pour atténuer les déconnexions fréquents. Nous proposons une nouvelle technique d'estimation de canal basée sur des pilotes pour les systèmes OTFS dans le domaine retard-Doppler, et introduisons une méthode d'estimation du canal Doppler fractionnaire basée sur l'apprentissage automatique utilisant les deep neural network.

Mots clés : Transport de tubes à ultra-haute vitesse, TransPod, bruit impulsif dû au plasma, modulation OTFS

Designing a high data rate wireless communication system in a doubly selective channel: TransPod system

Abstract: This thesis explores channel modeling and physical layer design to enhance high data rate communications in high mobility wireless channels, with a specific focus on the TransPod system. The work begins with a comprehensive review of wireless channels, focusing on doubly selective channels, their impairments, and modulation techniques such as OFDM and OTFS. We then characterize the TransPod guideway transmission channel, examining both large-scale and small-scale characteristics, and addressing noise from the plasma-based power transmission system. A dual-link communication system is proposed to mitigate frequent disconnectivity. We propose a novel sequence-pilot-based channel estimation technique for OTFS systems in delay-Doppler domain and introduce a machine learning-based method for fractional Doppler channel estimation using deep neural network.

Keywords: Ultra-high-speed tube-transportation, TransPod, impulsive noise due to plasma, OTFS modulation